NORTHWESTERN UNIVERSITY

Microfluidics on Self-Assembled Monolayers for Analyzing Biological and Chemical Reactions

A DISSERTATION

SUBMITTED TO THE GRADUATE SCHOOL
IN PARTIAL FULFILLMENT OF THE REQUIREMENTS

for the degree

DOCTOR OF PHILOSOPHY

Field of Chemistry

By

Jennifer Grant

EVANSTON, ILLINOIS

December 2018

Abstract

Recent advances in combinatorial chemistry, synthetic biology, and ‘omics’ research require high-throughput methods for performing and analyzing thousands to millions of reactions in one day. However, it is a challenge to engineer high-throughput systems that can autonomously conduct and analyze such a large number of reactions in a generalizable and quantitative format. Limitations in liquid handling robotics, instrument costs, and a lack of generalizable analytical tools prevent rapid and widespread implementation of high-throughput screening technologies. Microfluidic devices can precisely and predictably manipulate nanoliter to femtoliter fluid volumes in channels ranging from several to a few hundred microns− overcoming limitations associated with standard high-throughput screening technology. By taking adavtage of microfluidics, biological and chemical activities can be interrogated in detail while consuming minimal reagent and requiring less pipetting and bench time. In this work, I present several microfluidic devices for performing high-throughput experiments that would otherwise be impractical to conduct using standard benchtop strategies or modern liquid handling robotics. Each device interfaces microfluidics with self-assembled monolayers to quantitatively assess chemical and biological activities. A new technique called iSAMDI-MS (imaging self-assembled monolayers for matrix-assisted laser desorption/ionization mass spectrometry) is presented, in which a microfluidic device autonomously conducts thousands of unique reactions that are interpreted by a MALDI mass spectrometer capable of imaging. In addition, I present a strategy that uses microfluidics and self-assembled monolayers to spatiotemporally control the output of a two-step biochemical transformation.

The first demonstration of iSAMDI-MS uses a 3-dimensional (3D) microfluidic device to perform 2,592 distinct enzyme reactions using just 150 µL of reagent for calculating the Michaelis constant (K_m). The floor of the microfluidic device consists of a self-assembled monolayer that immobilizes the product in a time-dependent manner corresponding to the reaction progress. In this way, the position along the channel floor corresponds to the reaction time and each channel has a full kinetic profile describing each reaction, thereby providing all of the necessary information to calculate the K_m. Scanning the self-assembled monolayer with a MALDI mass spectrometer capable of imaging generates a 108 x 88 pixel array that is used to obtain the K_m. I present another biological application of iSAMDI-MS for calculating the Hill kinetics of an enzyme-ligand interaction. Here, a 3D microfluidic device first generates a linear concentration gradient of ligand, and then mixes the ligand with the enzyme. The enzyme becomes activated by the ligand and modifies a substrate immobilized to the self-assembled monolayer. The self-assembled monolayer is scanned with iSAMDI-MS and the amount of product conversion on the resulting pixel array reflects the extent of enzyme activation. Both methods introduce iSAMDI-MS as a high-throughput and label-free approach for characterizing enzyme kinetics while requiring minimal reagent, pipetting, and bench time.

The next example of iSAMDI-MS widens its applicability beyond the field of biology and into chemistry. Here, iSAMDI-MS is used to calculate a pH-dependent reaction rate from 15,720 unique time points with only 160 µL of reagent. A microfluidic device has two inputs—one for each reactant— that diffusively mix at the base of a Y-junction and travel along the length of a single, unidirectional channel. The floor of the microfluidic device covalently immobilizes the reactant and the product from the reaction proceeding in the flow above, such

that the device floor records the reaction progress and the distance downstream of the Y-junction correlates to the reaction time. Knowledge of the immobilization kinetics and the characteristics of the dispersion front allows us to determine the reaction rate.

The last strategy that I present uses a microfluidic device for precisely controlling the output of a two-step biochemical reaction. This strategy pairs a microfluidic channel with a SAM-functionalized chip that presents two immobilized enzymes and a product analysis region. The enzymes are immobilized in distinct regions onto the chip using orthogonal active site-directed chemistries. A downstream region of the chip covalently captures thiol-containing products and substrate. Spatially organizing the two enzymes on the chip along the flow direction gives rise to different product yields depending on the order of enzyme treatment, consistent with a mechanism of crosstalk. This work describes a new microfluidic device for the reaction and analysis of multistep biotransformations and demonstrates how spatiotemporally reordering the reaction steps affects product yields.

Acknowledgements

I express my deepest gratitude and appreciation towards my graduate advisor, Prof. Milan Mrksich. Milan has mentored, challenged, and inspired me with an insatiable level of intellectual curiosity and commitment to teaching. He prepared me to work at the intersection of many disciplines and pursue challenging problems in fundamental and applied research. Throughout my time at Northwestern, Milan provided me with the freedom and flexibility to take chemistry and biology into new directions. I am very grateful for his guidance and encouragement throughout my graduate career.

I would also like to thank Prof. Amy Rosenzweig and Prof. Julia Kalow for serving on my dissertation committee, and Prof. Thomas Meade and Prof. Neil Kelleher for serving on my qualifying exam committee.

I am very grateful to the National Science Foundation which supported my work for four years through the NSF Graduate Research Fellowship and to the Defense Threat Reduction Agency for supporting my work in my fifth and sixth years of graduate work.

I would like to thank all of my collaborators from the Mrksich lab: Justin Modica, Patrick O'Kane, Blaise Kimmel, Paul Perkovich, Juliet Roll, and Lindsey Szymczak. Justin served as an outstanding mentor throughout my graduate career and I admire his research skills, curiosity, and drive. Justin was responsible for synthesizing the HaloTag capture ligand in Chapter 6. Patrick O'Kane and Blaise Kimmel worked with me on the iSAMDI ligation kinetics project described in Chapter 4. Patrick discovered a new type of ligation reaction that was applied towards iSAMDI-MS for calculating the kinetics of the reaction. I approached Patrick when I was initially designing this iSAMDI-MS method and he agreed to work with me without any

hesitation. Blaise carried out the computational work required for this project and I am very grateful for his enthusiasm and commitment towards this work. I had the unique opportunity to work with two outstanding undergraduates at Northwestern− Paul Perkovich and Juliet Roll− over the course of three years. I am very proud that they both graduated from Northwestern with the ability to conduct independent research. They have my full support throughout their careers and I am confident that they will make a huge impact in their area of work. Lindsey Szymczak prepared the peptide library presented in Chapter 5, and I am grateful for her expertise in peptide arrays and SAMDI-MS.

I thank several collaborators from the Northwestern University core facilities who have helped me with the work presented in this thesis. Sohrab Habibi Gourarzi, who previously worked at the Integrated Molecular Structure Education and Research Center (IMSERC) at Northwestern, brought MALDI Imaging Mass Spectrometry to the Northwestern campus. He allowed me to be the first researcher at Northwestern to test it for several months before expanding its use by other researchers at the university. During this time, iSAMDI-MS came to fruition and we realized how powerful the MALDI-IMS technique would be in many different areas of research. Other collaborators at Northwestern core facilities who helped me with the work presented in this thesis are Michael Wasiukiewicz at the Research Shop− Instrumentation Design Engineering and Production, Michael Beltran at the 3D Printing and Rapid Prototyping Lab, Andrew Ott at IMSERC, and Saman Shafie at IMSERC.

This work is a product of the support from many colleagues, friends, and family members. First, I thank my undergraduate research advisor, Prof. Younan Xia, for accepting me into his laboratory at Washington University in St. Louis and introducing me to academic

research. I learned how to conduct research in his lab and my experiences in his group inspired me to attend graduate school. I am also grateful for other members of the Mrksich group who did not directly collaborate with me on the work presented in this thesis but were very important for helping me throughout my graduate career: Alison Bayly, Alexander Simon, Pradeep Bugga, Jose-Marc Techner, Alexei Ten, Elamar Hakim-Moully, Sarah Anderson, and Kevin Metcalf. Each one was always so supportive and never hesitated to provide their help. I am very grateful for the many lifelong friends that I made from the Mrksich group. I am very thankful for the support that my mother and father have provided me through their patience, love, and understanding. They always supported my interest in science over the years by encouraging me to participate in science fairs, take challenging high school science courses, and study engineering in college. This level of support is so important for a child to maintain their interest in science despite the challenging coursework and frequent setbacks that are prevalent in the field. Lastly, I am very grateful for the inspiration and companionship of my fiancée Tyler, who has provided unwavering support throughout my studies. I am very blessed to have all of these people in my life.

List of Abbreviations

ADM	axial dispersion model
AUC	area under the curve
ChIP	chromatin immunoprecipitation
EDTA	ethylenediaminetetraacetic acid
FRET	fluorescence resonance energy transfer
GSH	reduced glutathione
GSSG	oxidized glutathione
hGR	human glutathione reductase
HTS	high-throughput screening
IMAC	immobilized metal affinity chromatography
IMS	imaging mass spectrometry
IMSERC	integrated molecular structure education and research center
IPTG	isopropyl β-D-1-thiogalactopyranoside
iSAMDI-MS	imaging self-assembled monolayers for matrix-assisted laser desorption/ionization mass spectrometry
ITO	indium tin oxide
MALDI-IMS	matrix-assisted laser desorption/ionization imaging mass spectrometry
MALDI-TOF MS	matrix-assisted laser desorption/ionization time-of-flight mass spectrometry
MITOMI	mechanically induced trapping of molecular interactions
mVLSI	microfluidic very large scale integration

NADPH	dihydronicotinamide-adenine dinucleotide phosphate
OLA	octanol-assisted liposome assembly
PAD	peptidylarginine deiminase
PAD2	peptidylarginine deiminase type 2
PCAF	acetyltransferase p300/CBP associated factor
PCR	polymerase chain reaction
PDMS	polydimethylsiloxane
PTFE	polytetrafluoroethylene
ROI	region of interest
SAM	self-assembled monolayer
SAMDI-MS	self-assembled monolayers for matrix-assisted laser desorption/ionization mass spectrometry
SDS-PAGE	sodium dodecyl sulphate-polyacrylamide gel electrophoresis
SPR	surface plasmon resonance
TCEP	tris(2-carboxyethyl)phosphine hydrochloride
TFA	trifluoroacetic acid
THAP	2,4,6-tri-hydroxyacetophenone
TISM	tank-in-series model

Table of Contents

List of Figures

Chapter 1

Microfluidics for Conducting High-Throughput Experiments and Controlling Reactions

1.1 High-Throughput Assays in Microfluidic Devices

High-throughput screening (HTS) experiments simultaneously conduct hundreds to thousands of reactions while requiring less reagent and time per experiment than standard benchtop procedures. Advances in combinatorial synthesis, solid-phase synthesis, and microarray preparation have greatly increased the need for conducting HTS experiments. Compound libraries exceeding 1 million small molecules require new technology to manipulate and screen each compound against biological or non-biological targets. In addition, synthetic biology research often requires screening large genetic libraries and mapping complex cellular processes from numerous dense and disparate datasets. It is evident that continued advancements in biology, chemistry, and engineering require developing new and generalizable HTS strategies.

HTS experiments are typically performed in microtiter plates with liquid-handling robotics. Microtiter plate densities range from 96 to 6,144 wells and contain volumes ranging from a few nanoliters to several hundred microliters. Liquid handling robotics are programmed to automatically mix and dispense arrays of reaction mixtures, enabling over 1 million reactions to be performed in a day. However, these procedures require large capital investments and expert personnel which limits their applicability to a small number of research settings. In addition, liquid handling robotics are not able to reliably and quickly dispense nanoliter-scale droplets appropriate for 6,144 plate densities, leading to uncontrolled evaporation and experimental

variability.[1] Advances in nanoliter-scale reagent handling will be necessary for implementing HTS experiments with 6,144 and higher array plate densities.

Microfluidic systems overcome the limitations of traditional HTS procedures due to their ability to precisely control small reagent volumes and conduct multiplexed experiments inside a small footprint. Continuous-flow operation allows for integrating multiple experimental steps into one device, enabling cheaper and faster experimentation than standard HTS procedures. Several strategies have been developed to carry out sample preparation mixing, incubation, and separation in microfluidic devices. The three most common approaches use continuous flow, droplet-based, or arrayed valve designs (Figure 1.1).

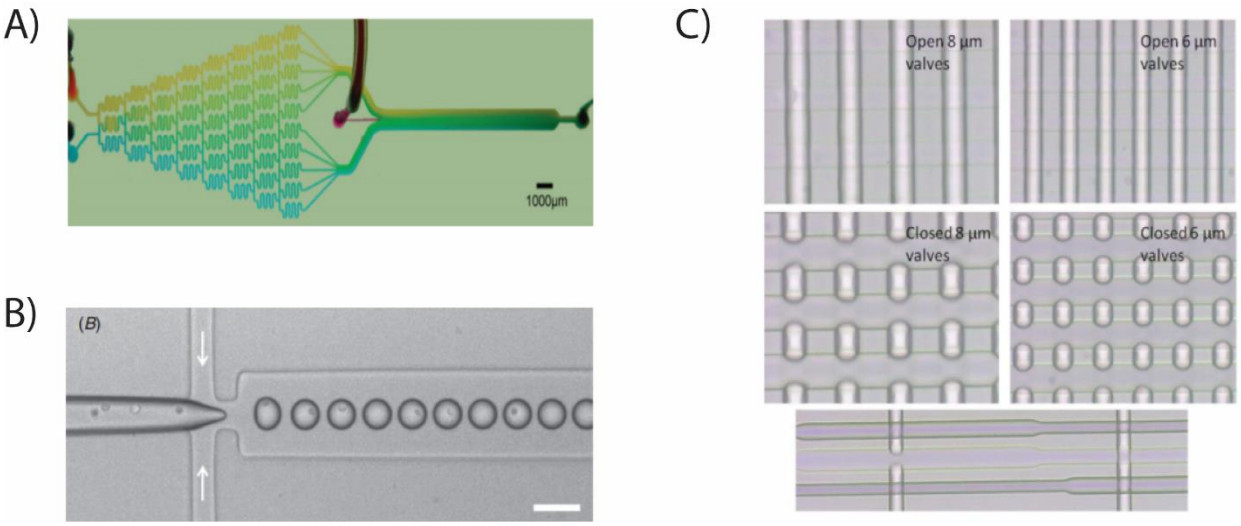

Figure 1.1 Multiplexing in microfluidic devices. A) Continuous flow linear gradient generator[2] B) Droplet-based microfluidic device[3] (reprinted with permission from IOP Publishing), C) Microfluidic very large-scale integration (mVLSI) device with arrayed valves[4] (reprinted with permission from the Royal Society of Chemistry)

Continuous flow systems generate complex and stable concentration gradients through controlled diffusive mixing in the laminar flow regime. Whitesides and coworkers first used this

approach to generate complex spatial and temporal concentration gradients by continuously splitting and merging microfluidic channels.[5] Linear, parabolic,[5] and log-scale molecular gradients can be used to recapitulate physiologically-relevant environments for cell studies.[6,7] Folch and coworkers developed a culture platform based on controlled diffusive mixing to generate stable and continuous gradients that impose low shear forces on cells or tissues. This strategy was applied towards a device containing 1,024 cell culture chambers, where each chamber had an individually-addressable concentration gradient, for conducting high-throughput cell screens.[8]

Droplet and segmented-flow microfluidic systems generate nanoliter-volume microdroplets by combining two immiscible phases under flow. Each droplet serves as an individual reaction chamber and arrays of droplets have been generated at kilohertz frequencies.[9] The droplets can be individually manipulated to control the reaction volume and content. Droplet-based assays have been developed for a variety of high-throughput applications, including protein crystallization,[10] enzyme kinetics,[11] PCR,[12] and strain optimization.[13] A unique advantage of droplet-based microfluidics is the absence of dispersion, which is known to complicate the position-to-time conversion in microfluidic devices. Confining reactions into discrete droplets minimizes the effect of dispersion and the reaction time course can be followed by monitoring the conversion within each droplet.

High-throughput screens have also been conducted in microfluidic devices that contain thousands of individually addressable valves and reaction chambers. The external valves and actuators are connected to an array of chambers for precise fluidic manipulation and reagent isolation. Microfluidic very large scale integration (mVSLI) devices designed by Quake and

coworkers contain valves as small as 6 x 6 μm^2 with densities approaching 1 million valves per cm^2.[14] The most widely-used valve design is the Quake valve− a pneumatically-controlled microvalve in which a control layer fills with air and pushes onto an adjacent fluidic channel, causing it to close.[15] Further advancements in micromechanical valve design and operation have introduced high-density array devices for applications such as PCR,[16] 3D cell culture,[17] and DNA binding studies.[18] For example, the MITOMI (mechanically induced trapping of molecular interactions) device integrates picoliter-scale reaction chambers on a double stranded DNA array for monitoring transcription factor-DNA binding events.[18] One MITOMI device can have up to 4,160 unit cells and 12,555 valves, where each reaction is conducted in a unit cell and three valves control one unit cell.[19]

Together, these approaches demonstrate the potential for microfluidics to overcome the limitations of robotic handling and use of microtiter plates in traditional HTS assays. In this work, I present three microfluidic devices that use continuous flow to conduct all of the necessary steps for obtaining Michaelis Menten kinetics, Hill kinetics, and chemical reaction rates from a single experiment. These microfluidic devices conduct thousands of individually addressable reactions using just two or three inputs. A self-assembled monolayer present on the floor of each device establishes a covalent record of the reaction progress from the flow above. Analysis of the self-assembled monolayer by MALDI imaging mass spectrometry− a process we define as iSAMDI-MS− reveals thousands of pixels representing each individual reaction as it occurred within the device.

1.2 Spatiotemporal Control in Biology and Microfluidic Devices

There are thousands of reactions simultaneously occurring in a living cell at any given time. To accomplish this, cells have evolved membrane-bound and non-membrane-bound compartmentalization strategies to organize metabolic processes. Compartmentalization establishes unique environments with distinct biochemical mixtures of enzymes, receptors, and metabolites for carrying out specialized tasks, and serves to sequester toxic intermediates, co-localize reactants, prevent reaction competition, and overcome diffusion. Examples of non-membrane-bound compartmentalization strategies include cytoplasmic phase separation and cytoplasmic streaming. Cytoplasmic phase separation rapidly increases local analyte concentrations, allowing reactions to initate without an outside regulatory event.[20,21] Cytoplasmic streaming occurs when organelles and vesicles move along the cytoskeleton and generate convective flows, which is believed to increase the frequency of enzyme-substrate interactions.[22,23] These examples demonstrate the importance of compartmentalization and spatiotemporal control in cellular metabolic maintenance and regulation. Strategies that mimic cellular spatiotemporal control in the laboratory are important and reveal the essential elements required for cell survival.

Spatiotemporally-controlled systems are challenging to engineer in the laboratory because they require applying the appropriate chemistry, micro and nano-scale interfaces, and analytical tools towards maintaining and measuring chemical and biological fluxes. Microfluidics have been used to mimic biological processes because fluid flows can be precisely manipulated and reagents are confined within small volumes. For example, Kanie and coworkers report a microfluidic chip with glycosyltrasferases bound to agarose beads and

arranged in series for the synthesis of a tetrasaccharide.[24] Niemeyer and coworkers developed a strategy to 3D print enzymes with agarose-based inks for control over the position and quantity of enzyme in a 2-step biotransformation.[25] Other devices have been designed to generate physiologically-relevant environments through precise fluidic manipulation at the microscale. A series of devices presented by Folch and coworkers generate stable gradients of small molecules for studying the effects of morphogen and chemokine gradients on axonal migration.[8]

In this work, I present an enzyme reactor that generates different yields of four possible reaction products, dependent on the direction of fluid flow through the reactor. This system takes advantage of '*in cis* crosstalk', in which a modification affects the addition or removal of another modification on the same substrate.

Chapter 2

MALDI Mass Spectrometry for Systems-Level Analyses

2.1 MALDI Imaging Mass Spectrometry

Matrix-assisted laser desorption/ionization mass spectrometry imaging (MALDI-IMS) is an analytical technique that determines the spatial arrangement of analytes from a 2-dimensional sample. MALDI-IMS can screen for a wide variety of analytes, including small molecules,[26] metabolites,[27] peptides,[28,29] and proteins,[30,31] and has been used to answer a wide variety of biological questions involving disease pathology,[31] subcellular compartmentalization,[32] and developmental biology.[33] A powerful feature of MALDI-IMS is the capability to identify analytes of interest without any prior knowledge of their location in the sample.

The majority of MALDI-IMS workflows have been developed for analyzing plant and animal tissue cross sections (Figure 2.1). MALDI-IMS on tissue cross sections begins with fixing ~10 μm thin tissue slices onto an indium-tin oxide (ITO)-coated glass slide and treating the fixed sample with matrix.[34] Matrix crystal size and homogeneity must be optimized towards each sample type to acquire consistent, high-quality spectra at micron-scale laser beam diameters and raster step sizes. The three matrix application methods commonly used in MALDI-IMS are airbrushing, automatic spraying, and sublimation.[35] Then, a photographic image of the sample is loaded into MALDI-IMS software and the sample is inserted into a MALDI mass spectrometer capable of imaging. A region of interest (ROI) is defined by overlaying an array of pixels onto the sample. The minimum pixel resolution is dependent on the laser diameter and matrix crystal spacing; these parameters must be optimized by the user before acquiring the MALDI-IMS dataset. The MALDI-IMS dataset is generated by acquiring one spectrum per pixel, where each

spectrum (i.e. pixel) is assigned a specific x,y-coordinate. The acquisition is automated, allowing for parallel analysis of hundreds to thousands of analytes in a single sample. The resulting image is an array of pixels that are colorized to identify the relative abundance of ions of interest. It should be noted that the color intensity in this ion map represents the intensity of the ion of interest in relation to the entire dataset. Thus, it is a measure of the relative ion abundance, rather than a true quantitative measurement. Quantitation requires information about the peak intensities or peak areas and an internal calibrant. Typically, the calibrant is an isotopic variant of the target ion or another species that has been externally calibrated against the target. Muddiman and coworkers developed an open-source software (MSiReader) that extracts peak intensities from the MALDI-IMS dataset, which can then be used for normalizing peak intensities for quantitation.[36,37]

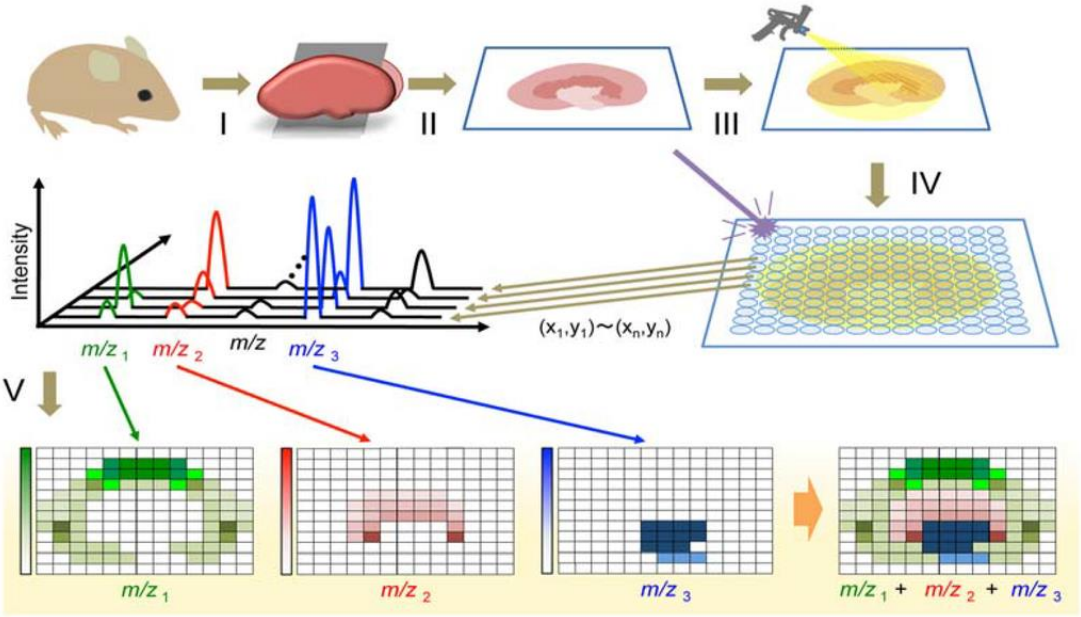

Figure 2.1 MALDI-IMS procedure.[38]

Bruker Daltonics manufactures the most advanced commercially available MALDI-TOF mass spectrometer capable of MALDI-IMS, called the rapifleX MALDI Tissuetyper (the 'rapifleX'). The rapifleX is capable of acquiring MALDI-IMS datasets at laser firing rates up to 10 kHz and with 10 μm pixel resolution. It is expected that future iterations will reach even higher frequencies and lower pixel resolutions. Academic research efforts have also worked to increase the capabilities of MALDI-IMS instrumentation. Notably, Caprioli and coworkers obtained a pixel resolution of 2.5 μm using transmission geometry MALDI-TOF MS.[39]

Here, I present work using MALDI-IMS for the analysis of synthetic substrates, rather than tissue cross sections, for high-throughput kinetic studies. The synthetic substrates are paired with networks of microfluidic channels, where the substrate comprises the floor of the microfluidic channel and selectively captures analytes from the flow above. Combining MALDI-IMS with a network of microfluidic channels enables analysis of thousands of unique experiments on a single chip. This work acquired spectra at 200 μm resolution with an Autoflex III MALDI-TOF MS (Bruker Daltonics). To date, no reported method has combined parallel microfluidic processes with MALDI-IMS.

2.2 SAMDI Mass Spectrometry

The Mrksich group pioneered a technique called SAMDI-MS (self-assembled monolayers for matrix-assisted laser desorption/ionization mass spectrometry) for high-throughput analysis of chemical and biological reactions on arrayed substrates. This strategy couples self-assembled monolayers on gold with MALDI-MS to rapidly detect mass changes accompanying a chemical or biological reaction.

The self-assembled monolayers (SAMs) consist of alkanedisulfides that form a well-defined, crystalline structure on gold-coated surfaces through a thiol-gold bond. The alkanedisulfides are functionalized to capture molecules of interest onto the self-assembled monolayer and are present against a background of tri(ethylene glycol groups) to prevent nonspecific protein adsorption. The Mrksich group has developed selective capture strategies using maleimide,[40] benzoquinone[41], and alkyne[42] functional groups that covalently react with thiols, cyclopentadiene conjugates, and azides, respectively. In addition, nonspecific strategies have been developed, which include traceless immobilization of unlabeled compounds with UV irradiation.[42] Selective methods for covalently capturing proteins that contain the enzymes cutinase,[43] SnapTag,[44] and HaloTag[44] have also been incorporated onto the self-assembled monolayer. These proteins site-specifically react with phosphonate, benzylguanine/benzylchloropyrimidine, and primary alkyl chloride-functionalized ligands, respectively, and generate a covalent bond to amino acid residues in the enzyme active site. The presence or absence of functional groups tunes the selectivity and reactivity of the SAM.

The SAMs are prepared on surfaces presenting an array of gold islands or one continuous gold layer. Until now, the vast majority of the work from the Mrksich group has used 384 and 1536-spotted array plates, where each spot on the plate represents a different set of reaction conditions. The array plates have been instrumental for analyzing enzyme specificities on peptide libraries,[45,46] chemical reaction discovery,[47] cellular lysate profiling,[48] and protein-ligand interactions.[49] In these studies, liquid handling robotics apply droplets containing the reactant to each array spot. However, transitioning from 1536 to 6144-spotted arrays is challenging due the limited dispensing capabilities of commercially-available liquid handling robotics. The work that

I present uses microfluidics to conduct all reagent handling steps and a surface coated entirely with a layer of gold. The array density is determined by the imaging resolution limit of the MALDI-TOF mass spectrometer.

The SAM-functionalized gold substrates are compatible with commercially-available MALDI-TOF MS instrumentation. Direct ablation of the matrix-coated surface with a MALDI-TOF laser desorbs the monolayer at the sulfur-gold bond. The intact masses of the disulfides and thiolates bound to the captured analytes are observed in the mass spectra (Figure 2.2). This allows for the label-free detection of biological and chemical reactions, which is advantageous because labels are known disturb native reactivity and generate false positives.[45,50] The combination of SAMs with MALDI-MS− called SAMDI-MS− can detect a wide variety of biological and chemical reactions and provides a quantitative readout of activities.[51–53]

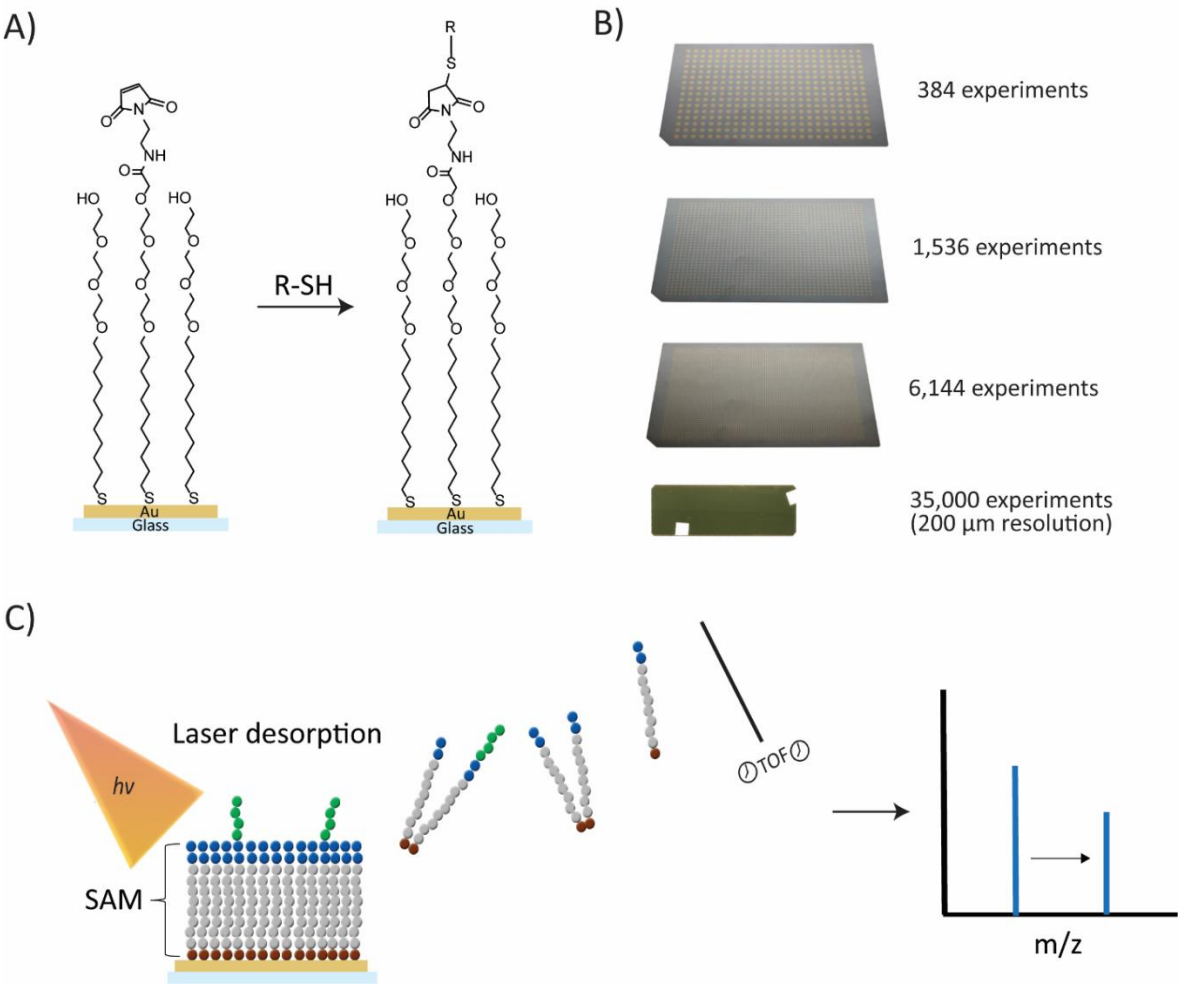

Figure 2.2 SAMDI-MS schematic. A) The SAM displaying maleimide functional groups reacts with thiol-derivatized molecules via Michael addition. B) SAMDI-MS substrate densities. C) A MALDI-MS laser ablates the SAM and desorbs intact disulfides and thiolates. The resulting mass spectrum shows a peak shift indicative of a reaction that took place on the monolayer prior to MALDI-TOF analysis.

In the first part of this work, I introduce imaging SAMDI-MS (iSAMDI-MS), which combines SAMDI-MS, microfluidics, and MALDI-IMS for conducting thousands of high-throughput experiments on a single chip. iSAMDI-MS generates datasets orders of magnitude greater than what is attainable with 1,536 and 6,144 array plates. Additionally, iSAMDI-MS requires over ten-fold less reagent and bench time than traditional assays. I describe developing

iSAMDI-MS for determining Michaelis-Menten kinetics, Hill kinetics, and chemical reaction kinetics. These parameters are essential for chemical and biological research but are laborious and time-consuming with standard benchtop protocols. In the second part of this work, I describe a spatiotemporal enzyme reactor that uses SAMDI-MS for the identification and quantification of 4 possible reaction products from a fluidic stream. I take advantage of the SAM's flexibility to pattern two protein immobilization regions and a product capture region on the same chip.

Chapter 3

High-Throughput Characterization of Enzyme Kinetics with 3D Microfluidics and Imaging SAMDI Mass Spectrometry

This chapter is adapted from the following published work:
Grant, J.; Goudarzi, S. H.; Mrksich, M. *"High-Throughput Enzyme Kinetics with 3D Microfluidics and Imaging SAMDI Mass Spectrometry"* Analytical Chemistry 2018, doi: 10.1021/acs.analchem.8b04391.

3.1 Introduction

Microfluidic systems have been important for increasing the throughput of biological assays and reducing reagent consumption. For example, a microfluidic device for chromatin immunoprecipitation (ChIP) required only 100 cells and 700 nL of reagent for epigenomic studies of hematopoietic stem and progenitor cells.[54] In addition, octanol-assisted liposome assembly (OLA) enabled the on-chip production of biocompatible liposomes at rates exceeding 10 Hz using 10 μL of reagent.[55] However, the two-dimensional structure of most microfluidic devices is not well-suited for mixing multiple reagents in large numbers of combinations, and the need for fluorescent labels to analyze reaction products limits the generality of microfluidic formats for characterizing enzymes. Additionally, microfluidic devices are often designed with networks of valves and arrayed reaction chambers that add complexity to the device design and operation. We demonstrate the combination of a simple three-dimensional fluidic structure and imaging mass spectrometry to perform 2,592 unique biochemical experiments on a chip, and highlight its applicability towards providing kinetic constants for an enzyme.

High-throughput microfluidic reaction systems can overcome the limitations inherent to manually preparing and analyzing thousands of separate experiments on the laboratory bench. For example, combinatorial microfluidic mixers based on a three-dimensional network of

channels have eliminated the need to manually mix and dispense solutions for large-scale biological screens.[56,57] In a landmark paper, Quake and coworkers described a device having 1,000 valve-controlled reaction chambers to rapidly access thousands of reaction conditions,[58] highlighting the advantages of using microfluidics for high-throughput screening applications. To circumvent the need for large numbers of integrated valves on a chip, Ismagilov and coworkers developed a droplet-based method to screen multiple reaction conditions for protein crystallization[59] and bacterial susceptibility to antibiotics.[60] That method has been integrated with a variety of detection methods, including MALDI mass spectrometry, to calculate the relative concentration of a reaction product.[61] These approaches demonstrate the potential of combining microfluidic devices with new detection strategies to enable high-throughput experiments for a broad range of enzyme activities, while requiring substantially less reagent and shorter assay times than conventional approaches.

In this chapter, we use iSAMDI-MS to obtain quantitative, high-throughput maps of reaction progress. We quantitate 2,592 unique experiments performed in flow− using only 150 μL of reagent− where the products were captured onto a self-assembled monolayer that could then be imaged with mass spectrometry to demonstrate its application towards calculating the Michaelis constant (K_m) of an enzyme-substrate reaction. We used a multilayer microfluidic device that generated a gradient of substrate concentration and simultaneously introduced an enzyme solution to each channel to initiate the reactions. As the reaction proceeded, the product underwent immobilization to a monolayer on the floor of the channel to record a kinetic profile of the reaction. We imaged the floor of the microfluidic device with SAMDI mass spectrometry to generate a 110 x 91 pixel array of adjacent 200 μm x 200 μm regions, and present a

quantitative map of reaction progress. In this way, the device carried out thousands of reactions without requiring any valves or isolated reaction chambers. iSAMDI-MS is a powerful method that uses a simple fluidic device and a minimal amount of reagent to obtain a high-density dataset of reaction progress.

3.2 Results

Experimental Design. Our device for measuring the Michaelis constant for an enzyme is shown in Figure 3.1. The device has three input solutions— enzyme, substrate and buffer— and two layers of channels on top of a substrate functionalized with a self-assembled monolayer. The bottom layer uses controlled diffusive mixing of the substrate and buffer to give a linear concentration gradient of substrate along eight parallel channels.[62,63] The top layer partitions a solution of enzyme and calibrant into a set of eight identical parallel channels that are then mixed with the substrate in the bottom layer to initiate the reactions. As the reactions flow down the channels in the bottom layer, the product of the reaction undergoes immobilization to a self-assembled monolayer on the floor of the channel. Hence, the position along the channel corresponds to the reaction time such that each channel has a full kinetic profile for each reaction and each channel contains a unique substrate concentration, thereby providing all of the information necessary to determine the K_m.

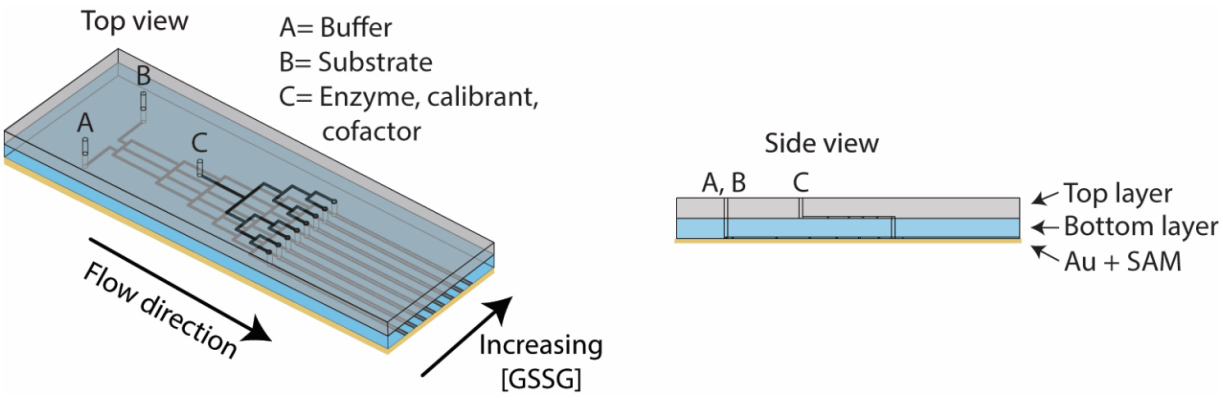

Figure 3.1 Michaelis Menten microfluidic platform design. Inlets A (buffer) and B (substrate) deliver reagent into the bottom layer with unique concentrations of substrate in each of the eight final channels. Inlet C delivers enzyme into the top layer, which then introduced into the bottom layer. Both layers are placed on top of a gold slide functionalized with a self-assembled monolayer terminated with maleimide functional groups.

We included a constant concentration of an isotopically labeled version of the product to quantitate the amount of product formed. The ratio of peak intensities for the product and calibrant gives the product yield in the solution where it underwent immobilization. The device was operated by flowing the three solutions into the device for approximately 1 h. The fluidic cassette was disassembled and iSAMDI-MS was used to quantitate the amount of product and calibrant with a resolution of 200 μm (square pixels) directly from the monolayer.

The monolayer comprising the floor of the microfluidic device was formed by self-assembly of maleimide-terminated disulfides and tri(ethylene glycol)-terminated disulfides on a gold-coated glass slide. The maleimide groups serve to immobilize cysteine-terminated peptides by a Michael addition of the thiol group and the tri(ethylene glycol) groups prevent nonspecific adsorption of the enzyme.

In the present example, we use human glutathione reductase (hGR) which catalyzes the NADPH-dependent conversion of oxidized glutathione (GSSG) to reduced glutathione (GSH)

(Figure 3.2A). The free thiol group in GSH allows the product of the reaction to be immobilized to the self-assembled monolayer, while the GSSG substrate lacks a free thiol group and is unable to undergo immobilization with the monolayer. We included an isotopically labeled GSH ([$^{13}C_2$, ^{15}N]-GSH) at constant concentration in the reaction mixtures. This molecule underwent co-immobilization with the product and allows for quantitation of the product by calculating the ratio of peak intensities in the mass spectrum. We used an isotopomer of the actual product to ensure that both GSH and [$^{13}C_2$, ^{15}N]-GSH have identical immobilization rates and ionization efficiencies in the mass spectrometry experiments. We validated the detection of hGR activity with SAMDI-MS by allowing a mixture of hGR, GSSG, [$^{13}C_2$, ^{15}N]-GSH, and NADPH to react and pipetted the reaction mixture onto the self-assembled monolayer to allow immobilization of the product and calibrant. SAMDI-MS spectra were obtained from 125 laser shots with a fixed sample stage to simulate imaging acquisition conditions. A SAMDI-MS spectrum of the monolayer before the hGR-catalyzed reaction showed peaks at *m/z* 809, 841, and 873 corresponding to the maleimide- alkanedisulfide conjugate (Figure 3.2C). Treatment of the monolayer with the reaction mixture revealed peaks representing the GSH-akyldisulfide conjugate and the [$^{13}C_2$, ^{15}N]-GSH -alkanedisulfide conjugate (Figure 3.2D).

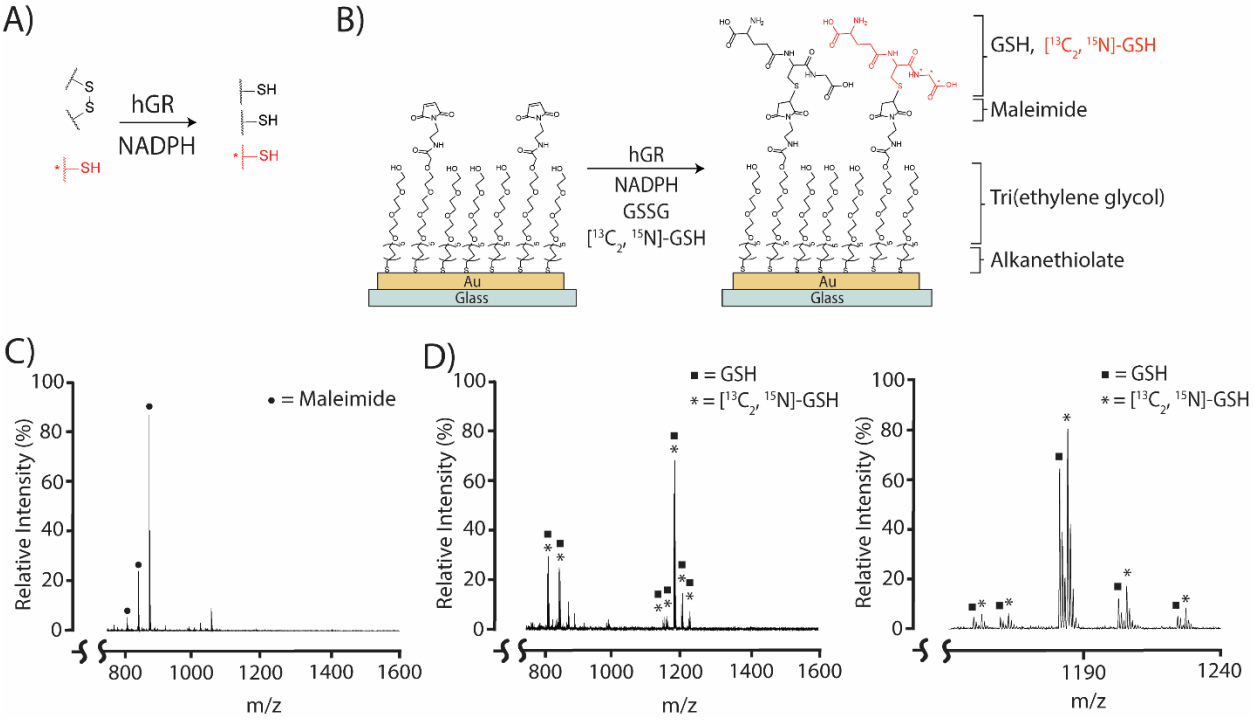

Figure 3.2 Detecting hGR activity with SAMDI-MS. A) Glutathione reductase (hGR) reaction. An isotope of reduced glutathione (red) is present for GSH quantitation. B) GSH and [$^{13}C_2$, ^{15}N]-GSH bind to a self-assembled monolayer terminated with maleimide functional groups that constitute the floor of the fluidic channel. C) iSAMDI-MS spectrum with peaks at *m/z* 809.16, 841.19, and 873.12 (circles) representing the maleimide-alkanedisulfide conjugate. *m/z* range 750-1600. D) iSAMDI-MS spectra from a channel after the hGR reaction. The GSH-alkanedisulfide conjugate and GSH-alkanethiol conjugate peaks are noted by squares at *m/z*= 812.08, 846.09, 1148.21, 1180.24, 1202.18, and 1224.23. Peaks representing the [$^{13}C_2$, ^{15}N]-GSH-alkanedisulfide conjugate and [$^{13}C_2$, ^{15}N]-GSH-alkanethiol conjugate are represented by asterisks (*m/z*=815.09, 849.09, 1151.33, 1183.25, 1205.20, 1227.14). Spectra were accumulated with 125 laser pulses. Peaks representing the maleimide-alkanedisulfide conjugate are no longer present. Left: *m/z* range 750-1600; right: *m/z* range 1140-1240.

The top and bottom PDMS layers were each prepared by casting against a 3D printed master (Figure 3.3). The use of a 3D printer to prepare the masters was significant because it increased the rate at which designs could be iteratively tested. The master for the bottom layer contained a 2-input/8-output pyramidal network of 250 µm tall, 250 µm wide channels that split and combined with neighboring streams at each node. Cylindrical posts (3 mm tall, 800 µm

diameter) were placed at each output of the pyramidal network to generate through-holes for connecting the two PDMS layers. The eight channels downstream of the cylindrical posts were 550 μm wide and 550 μm tall, allowing for the acquisition of three technical replicate kinetic traces. The top layer contained a 1-input/8-output network of channels 250 μm wide and 250 μm tall. The 3D printed masters allowed for facile PDMS polymerization and removal, and the masters were used for subsequent polymerization cycles.

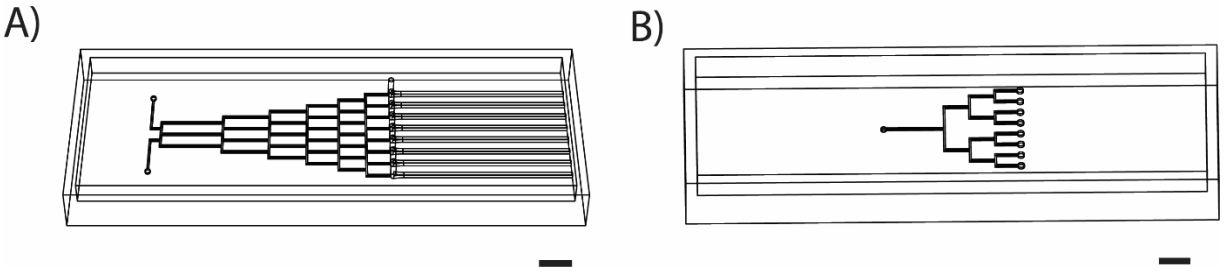

Figure 3.3 SolidWorks renderings of PDMS masters. A) top layer, B) bottom layer. Scale bar= 5 mm.

Device Operation. The device operation began with aligning both PDMS layers onto a gold coated substrate functionalized with the self-assembled monolayer (Figure 3.4). The PDMS and monolayer assembly were held together using light pressure from an external clamp. To generate the substrate gradient, potassium phosphate buffer and GSSG were flowed into both inlets A and B of the bottom layer, respectively, and potassium phosphate buffer was flowed into the top layer for 25 min to equilibrate the device. The inlet of the top layer was then replaced with a solution of hGR, [$^{13}C_2$, ^{15}N]-GSH, and NADPH to initiate the reactions, which were allowed to flow for 1 h. During this time, the product and calibrant underwent immobilization to the monolayer and once all of the maleimide groups had reacted, the reaction kinetics were

permanently recorded on the monolayer. The microfluidic device was then rinsed with potassium phosphate buffer and removed from the monolayer, which was then imaged with SAMDI mass spectrometry.

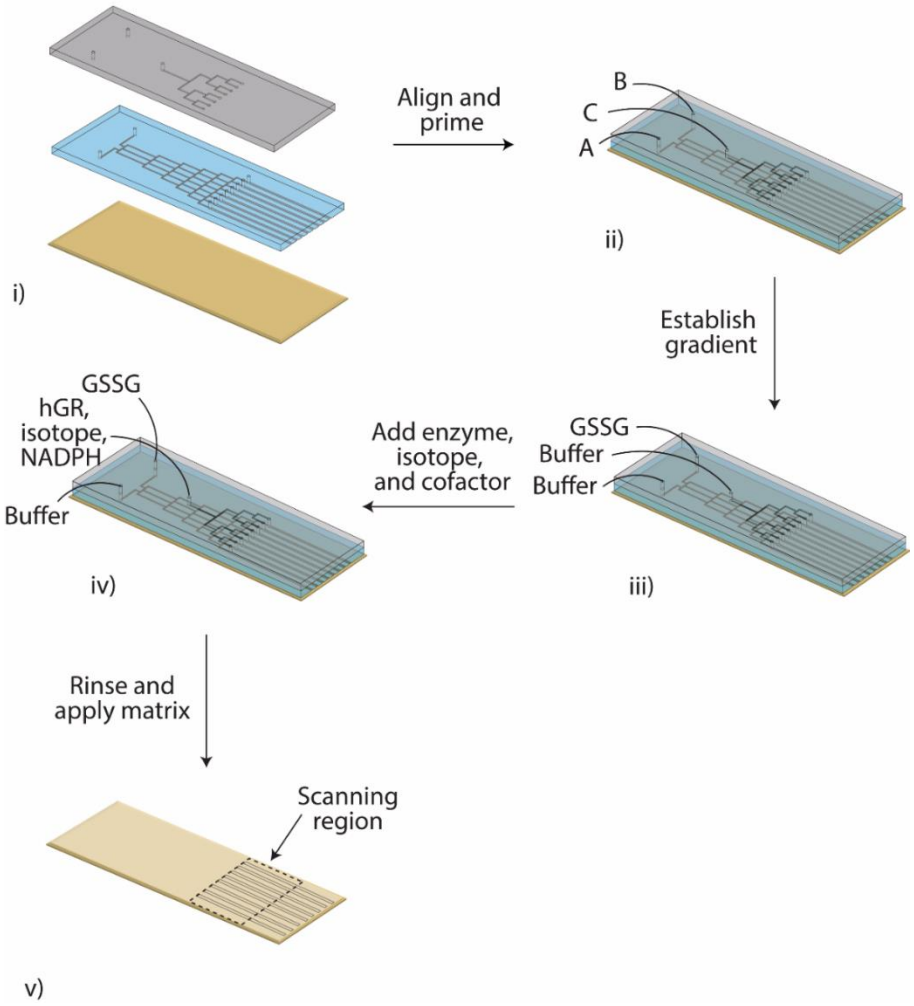

Figure 3.4 Schematic of microfluidic reactor assembly and operation. i) The bottom and top layers are aligned using the 8 through-holes in the bottom layer and placed on a gold slide functionalized with self-assembled monolayer. ii) Tubing is inserted in to all three inlets (A, B, C) and the device is primed. iii) A gradient of GSSG is established by injecting buffer into inlets A and C, and GSSG into inlet B. iv) hGR, [$^{13}C_2$, ^{15}N]-GSH, and NADPH are introduced through inlet C. v) The top and bottom layers are removed from the chip, the chip is rinsed, and matrix is applied. A region of the chip is scanned with iSAMDI-MS.

Matrix crystal homogeneity and spacing significantly affects the spectral quality and resolution in IMS workflows. With this in mind, we developed a simple matrix application technique for iSAMDI-MS that did not require matrix sprayers or precision injectors commonly implemented in IMS workflows.[64] Additionally, we confirmed that we could accumulate 125 shots within each 200 μm^2 region without any pixel overlap (Figure 3.5).

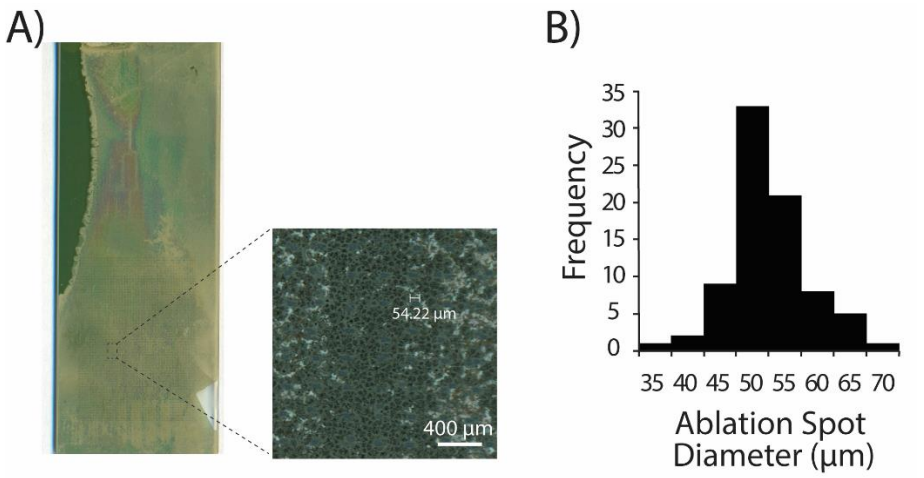

Figure 3.5 Ablation spot diameter measurements. A) image of the chip after iSAMDI-MS acquisition (left). Right: Photo of the chip after iSAMDI-MS showing individual ablation spots. The diameter of one ablation spot is indicated. B) Histogram of the diameter of 80 ablation spots. A lateral resolution of 200 μm does not oversample the dataset.

Acquisition and Analysis. MALDI imaging mass spectrometry has emerged as a powerful tool to determine the spatial distribution of small molecules,[26] metabolites,[27] peptides,[28,29] and proteins[30,31] from a two-dimensional array of mass spectra. We combined the quantitative and high-throughput features of SAMDI-MS with the spatial resolution of microfluidics and IMS in a single experimental setup and workflow (Figure 3.6).

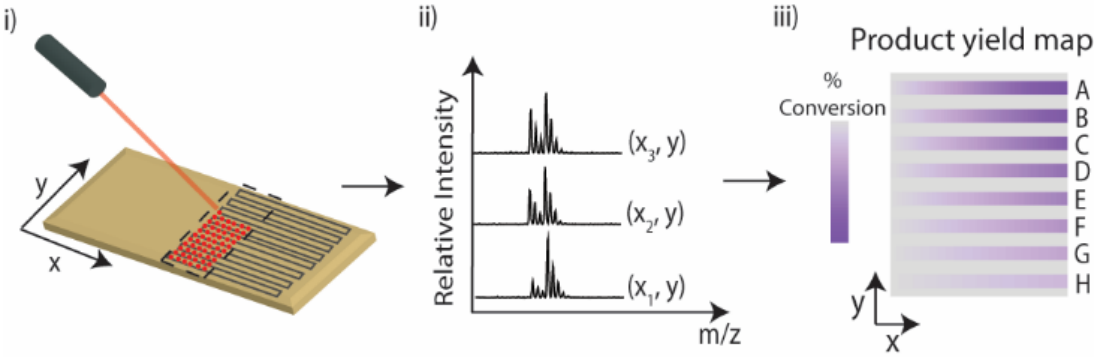

Figure 3.6 iSAMDI-MS procedure. i) A MALDI-IMS laser ablates pixels with a ROI at a lateral resolution of 200 µm. ii) iSAMDI-MS spectra are accumulated at each x,y-coordinate. iii) Imaging data is imported into MSiReader[65,66] for peak intensity extraction. A heatmap of conversion at each x, y-coordinate is obtained from the extracted data (theoretical heatmap shown).

To begin iSAMDI-MS data acquisition, an image of the matrix-coated monolayer was scanned to identify the region of interest (ROI). We selected a ROI that began at the junction between the top and bottom layers and extended along the direction of the fluid flow. The resulting ion maps of GSH, [$^{13}C_2$, ^{15}N]-GSH, and maleimide correlated well with the channel features in the bottom layer (Figure 3.7).

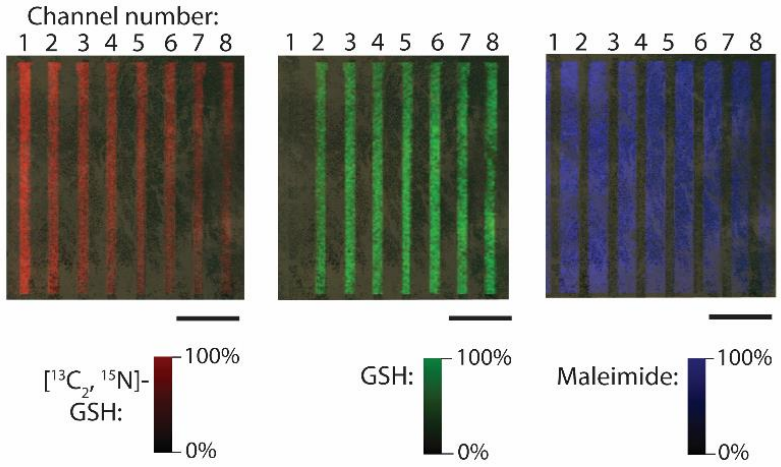

Figure 3.7 Ion maps of analyte detected with iSAMDI-MS (110 x 91 pixel array). Left: map of [$^{13}C_2$, ^{15}N]-GSH-alkanedisulfide conjugate (*m/z* 1183.20) visualized in red. Center: map of GSH-alkanedisulfide conjugate (*m/z* 1180.20) visualized in green. Right: map of maleimide-alkanedisulfide conjugate (*m/z* 873.18) visualized in blue. Scale bar= 5 mm.

The ion maps revealed the distribution of each analyte, and significantly, did not require prior spatial registration of the monolayer. The red color represents the distribution of [$^{13}C_2$, ^{15}N]-GSH-alkanedisulfide conjugate ([M+Na]$^+$), the green color represents the GSH-alkanedisulfide conjugate ([M+Na]$^+$), and the blue color represents the maleimide-alkanedisufide conjugate ([M+Na]$^+$). The presence of [$^{13}C_2$, ^{15}N]-GSH in each channel shows that hGR was successfully delivered into the bottom layer, because [$^{13}C_2$, ^{15}N]-GSH and hGR were co-injected into the top layer. The maleimide distribution confirmed that the channels did not leak during the device operation. A plot of [$^{13}C_2$, ^{15}N]-GSH- alkanedisulfide ([M+Na]$^+$) peak intensity at a fixed pixel on the x-axis showed that three to four pixels containing the ion were obtained across the 550 μm wide channels (Figure 3.8). Therefore, three to four replicate kinetic profiles were acquired at each substrate concentration. SAMDI mass spectra representing one pixel from each channel are shown in Figure 3.9.

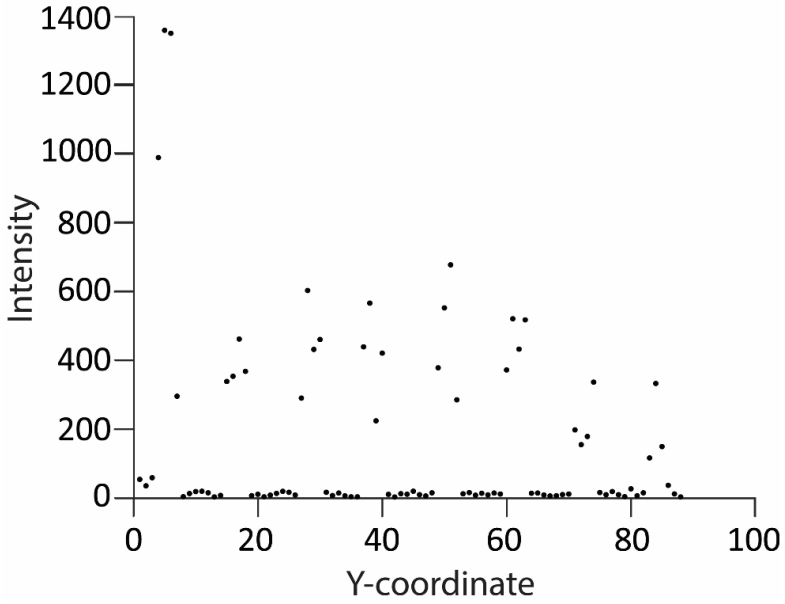

Figure 3.8 Plot of [$^{13}C_2$, ^{15}N]-GSH- alkanedisulfide (*m/z* 1183.2) peak intensity from each pixel along the y-axis at a fixed x-coordinate, x= 41. 3-4 pixels are acquired across each channel.

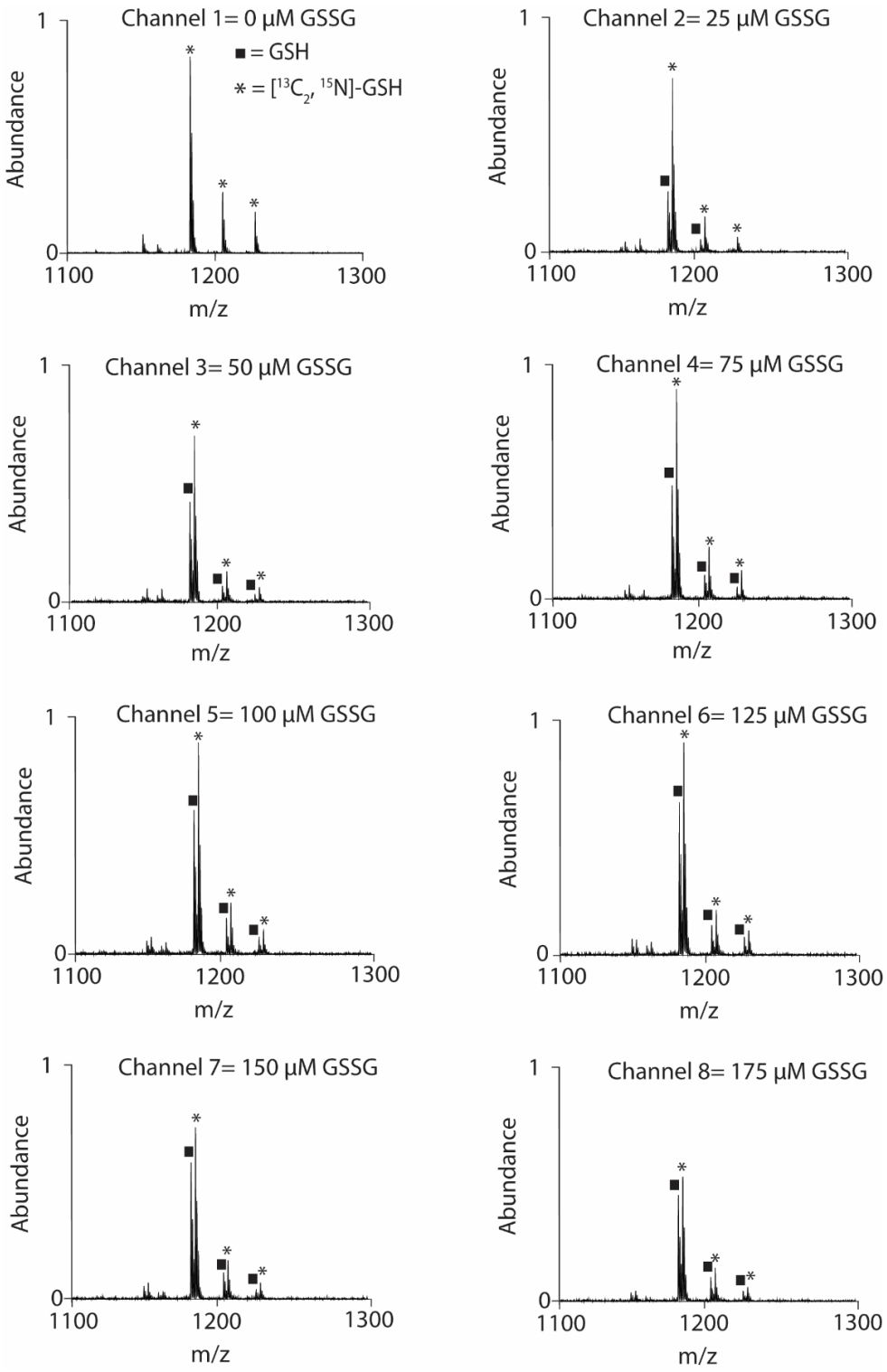

Figure 3.9 SAMDI-MS spectra of one pixel from each channel obtained from FlexImaging software at x= 258.

To demonstrate the applicability of iSAMDI-MS for assaying enzyme kinetics, we calculated the product conversion and K_m of hGR. We extracted a 108 x 88 pixel array and calculated GSH yield from each pixel located on a channel. From 9,504 pixels in the image, 2,592 were located on a channel and used for GSH product quantitation. The spatial product distribution revealed differences in relative reaction velocities in accordance with Michaelis-Menten kinetics (Figure 3.10A).

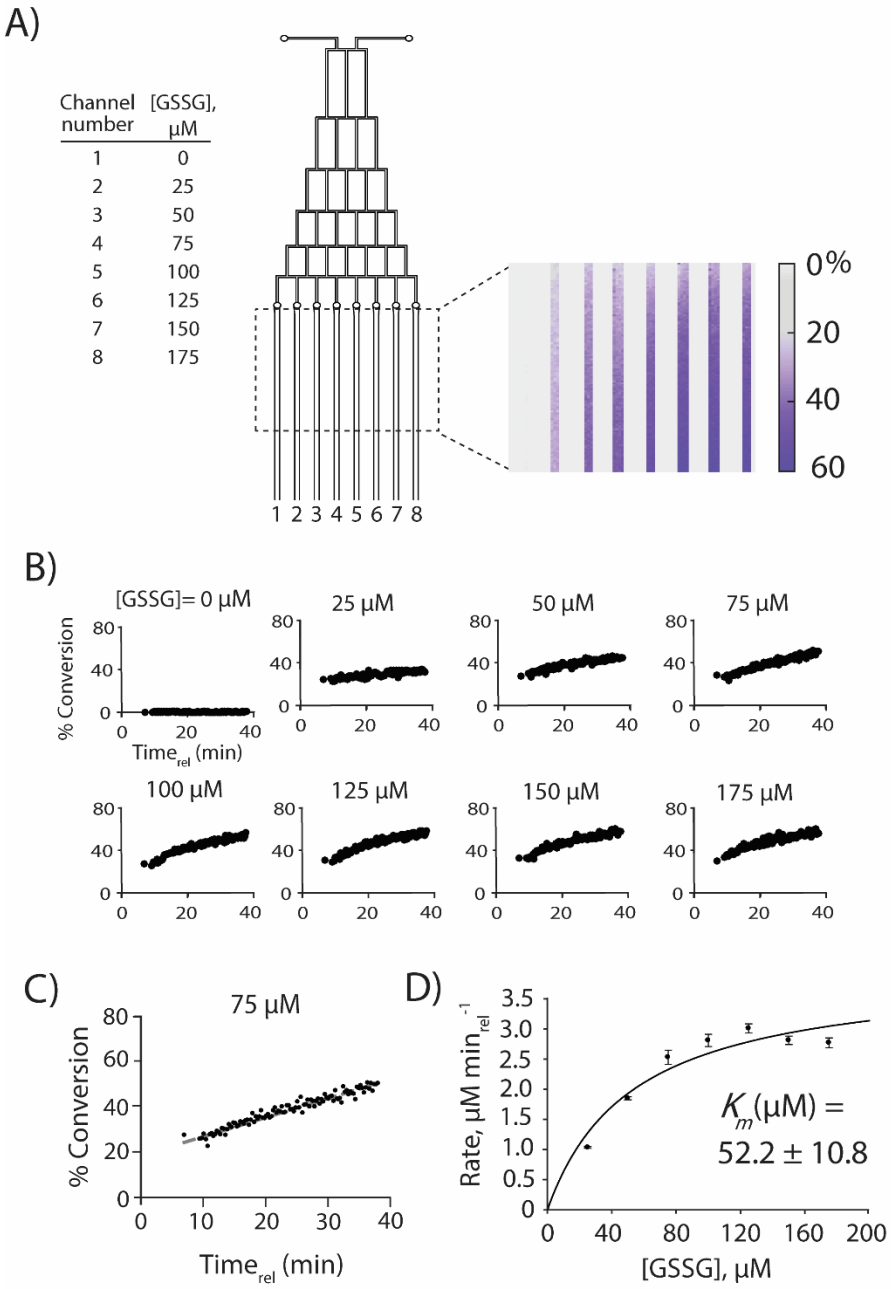

Figure 3.10 iSAMDI-MS output. A) Spatial map of hGR conversion at each x,y- coordinate (108 x 88 pixel array). B) Representative initial velocity curves from each channel; 108 data points (pixels) each; one technical replicate. C) Initial velocity curve from channel 4; 108 data points (pixels), R^2= 0.95. D) Michaelis-Menten plot showing K_m= 52.2 ± 10.8 µM. Average initial velocity ($\overline{v_0}$) is calculated from three technical replicates from each channel. Error bars: one standard deviation, three technical replicates from each channel, R^2 of 0.87.

The Michaelis-Menten constant, K_m, describes the effective affinity of an enzyme for its substrate, and is one of the most important equations for describing enzyme activity. The K_m is calculated from the Michaelis-Menten equation:

$$V_o = \frac{V_{max}[S]}{K_m + [S]} \qquad (3.1)$$

where V_o, V_{max}, and S are the initial reaction velocity, maximum reaction velocity, and the substrate concentration, respectively. We chose t=0 to be the first point on the bottom layer that intersected with the top layer. The average fluid velocity was used to approximate the elapsed time from t=0 to the first pixel in the ROI. The relative time for the fluid flow to travel 200 μm in the longitudinal direction was calculated using the average fluid velocity and plotted against product conversion (Figure 3.10B). In total, 24 unique initial velocity curves were obtained with 108 data points (pixels) each, and linear regression was used to fit each line with the slope representing V_o (Figure 3.10B, Figure 3.10C, Figure 3.11). The three V_o values from each channel were averaged and plotted as a function of substrate concentration (Figure 3.10D). Fitting this data to the Michaelis-Menten equation revealed a K_m of 52.2 ± 10.8 μM (SigmaPlot, Systat Software). Our K_m agrees well with the previously published value of 65 μM,[67–69] demonstrating the practicality and feasibility of this method.

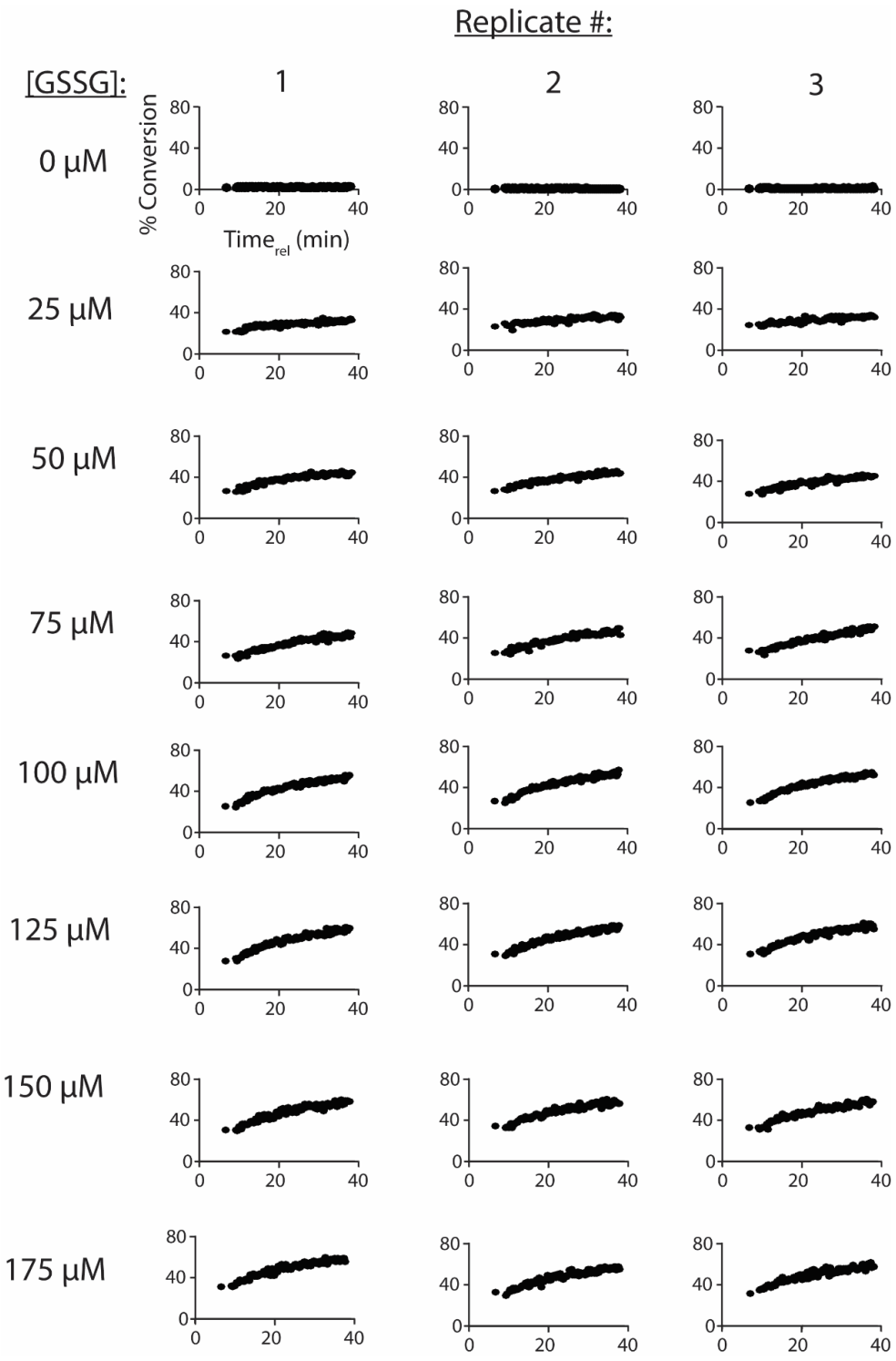

Figure 3.11 Three initial velocity curves plotted from each channel. 108 data points (pixels) in each plot.

3.3 Discussion

This chapter demonstrates how iSAMDI-MS can be integrated with a simple microfluidic device to perform high-throughput biochemical experiments with quantitative characterization of enzyme kinetics. This work is significant because it illustrates how modest amounts of reagents can be combined to perform thousands of distinct reactions. The reaction density is achieved by covalently capturing the reaction product on a self-assembled monolayer to generate a spatial map of the reaction progress. The use of self-assembled monolayers as the floor of the microfluidic device allowed the selective immobilization of the product (with the isotopically labeled calibrant) and therefore the use of SAMDI for quantitation. The use of a MALDI instrument capable of imaging was critical and represents the first example of iSAMDI-MS to obtain quantitative data on a large number of reactions. Each experiment required 60 nL of reagent mixture, which is nearly 200-fold less than the volume required for common multiwell plate formats. A total of 2,592 reactions were simultaneously analyzed to obtain the Michaelis constant, which agreed with the value reported from batch-based methods. Important work by Gardeniers and coworkers demonstrated the benefits of combining IMS and microfluidics by quantitating 29 measurement points along the length of a serpentine, porous silicon channel to monitor arginase reaction progress.[70] Our method makes a significant advance by interfacing a 3D microfluidic device with chemically-defined self-assembled monolayers to perform several thousand parallel reactions on one chip.

The development of mass spectrometers with higher imaging resolution and faster scan speeds should make it possible to analyze over one million distinct reactions in one iSAMDI-MS experiment with <10 μm pixel width. Notably, Caprioli and coworkers obtained a resolution of 2.5 μm using transmission geometry MALDI-TOF-MS.[71] Commercial MALDI-IMS

instrumentation can achieve lateral resolutions of approximately 10 μm and operate at laser pulse rates of 10 kHz. We recently surveyed iSAMDI-MS performance on the next generation of IMS instrumentation (rapifleX MALDI Tissuetyper, Bruker Daltonics) using the same self-assembled monolayer and matrix application methods described in this work, and we obtained comparable signal-to-noise and peak resolution at 10 μm lateral resolution. Collecting massive amounts of activity data from parallel experimentation will find useful applications in drug development, clinical diagnostic tests, directed evolution, and cellular activity assays.

Our approach uses a microfluidic device that is simple to design, fabricate, and operate. The device conducted thousands of reactions without requiring fluidic valves or isolated arrays of reaction chambers. With iSAMDI-MS, a variety of fluidic designs−ranging from the simplest single channel systems[72] to the most complex networks[58,73]−can provide high-throughput datasets because the reaction zones are defined by the resolution of the MALDI imaging mass spectrometer. We also used 3D printing to rapidly fabricate and prototype new device designs, which can be easily adapted to other applications given the recent and widespread implementation of 3D printers in academic and commercial laboratory settings. iSAMDI-MS combines the scalability of MALDI imaging and versatility of 3D printing to greatly advance current high-throughput assay methods.

We recognize that this particular assay requires the enzyme to generate a product with a thiol available for immobilization to the maleimide groups, and that the substrate must not bind to the monolayer. Future work may generalize this assay by using chemistries that can be activated after the flow has been established at steady-state.[74–76] In this way, iSAMDI-MS might be suitable for analyzing many different types of enzymatic and chemical reactions, including

those that utilize cysteine-terminated peptides,[77] thiol-terminated sugars,[78] and thiol-containing small molecules. We also emphasize that we did not measure k_{cat}, because translating a specific distance along the microfluidic channels into a reaction time is challenging due to dispersion.[79–81] Strategies to overcome dispersion might use droplets (plugs), as described by Ismagilov and coworkers,[80,82] and trapping the plugs over specific areas of the channel for subsequent reaction with the self-assembled monolayer.

The work presented here is a first example that demonstrates how iSAMDI-MS and fluidic structures can be combined to perform thousands of unique reactions from a small amount of reagents. Here we demonstrate the measurement of a K_m value, but we expect that this method can be extended to other applications in biochemistry and chemistry.

3.4 Experimental

Buffers. All measurements were conducted in 0.1 M potassium phosphate buffer (pH 7.5).

Self-assembled monolayer preparation. Standard glass microscope slides were cleaned using ethanol and water in a sonication bath. An electron beam evaporator (Thermionics VE-100) was used to deposit 5 nm Ti (0.02 nm s^{-1}) followed by 30 nm Au (0.05 nm s^{-1}) at a pressure between 1 x 10^{-6} and 8 x 10^{-6} Torr. The slides were soaked overnight at 25 °C in an ethanolic solution (0.5 mM total disulfide concentration) having a 2:3 ratio of an asymmetric disulfide terminated with a maleimide group and tri(ethylene glycol) group, to a symmetric disulfide terminated with tri(ethylene glycol) groups. The slides were then rinsed with ethanol and water.

Microfluidic device fabrication. Poly(dimethylsiloxane) (PDMS) masters were rendered on SolidWorks software (Figure 3.3). The master for the top layer had one 800 μm inlet branching into eight 250 μm width and 250 μm height channels. The master for the top layer had two 800 μm inlets that split and merged into eight 250 μm width and 250 μm height channels. 800 μm width and 3 mm tall posts connected the bottom layer to the top layer, and the channels expanded to a width of 550 μm and height of 550 μm after this intersection. The files were converted to stl format and printed in digital printing mode using a Stratasys Connex 350 3D printer in VeroWhite material (Stratasys Direct) with a glossy finish. The 3D printed masters were prepared for PDMS polymerization as previously described.[44] PDMS prepolymer mixture was mixed in a 1:10 ratio (w/w curing agent to prepolymer), degassed in a vacuum desiccator for 15 min, and poured into the 3D printed master. The master containing PDMS was degassed in a vacuum desiccator for 15 min and placed in a 43 °C oven overnight. The PDMS blocks were then peeled off of the mold and treated in a 130 °C oven for 10 min. The 3D printed molds were reused for additional PDMS curing cycles. A 0.8 mm biopsy punch was used to form the inlets of the top and bottom PDMS layers, and to ensure that all of the through-holes in the bottom layer were completely formed. To ensure that the punched holes in the top layer intersected with the bottom layer, the two layers were aligned under a stereo microscope (Leica M125) before forming the inlets in the top layer. The top and bottom PDMS layers were then treated with 50 W air plasma for 35 s at 200 mTorr (Solarus Plasma Cleaner, Gatan, Inc.) and aligned under a stereo microscope. The two-layer PDMS device was placed onto the Au slide functionalized with the self-assembled monolayer so that the bottom PDMS layer was in contact with the slide. The PDMS and Au slide assembly was held together using light pressure from an external clamp

made from extruded polycarbonate secured with six screws. The clamp had three 1.5 mm diameter holes to match the location of the three device inlets. PTFE tubing (0.042" outer diameter, Cole-Parmer) was inserted into each inlet via stainless steel catheter couplers (22 ga x 15 mm, Instech) and the bottom layer was primed with buffer using a syringe pump (PhD 2000, Harvard Apparatus). The top layer was primed with buffer using a second syringe pump. Any remaining bubbles were removed by individually applying flow rates > 500 μL min^{-1} to each syringe. The absence of bubbles was confirmed using a stereo microscope.

Microfluidic device calibration. Buffer was introduced into the top layer at a flow rate of 0.8 μL min^{-1}. Simultaneously, a solution of 350 μM L-glutathione reduced (≥98%, Sigma-Aldrich) and 350 μM [$^{13}C_2$, ^{15}N]-GSH (≥95% purity; glycine-13C2, ≥98%; 15N, 96-99%; ≥90% net peptide, Cambridge Isotope Laboratories, Inc.) was injected into one inlet of the bottom layer, and a solution of [$^{13}C_2$, ^{15}N]-GSH (350 μM) was injected into the second inlet of the bottom layer at a flow rate of 0.4 μL min^{-1}. The device diluted GSH into a linear gradient of 8 concentrations while maintaining the concentration of [$^{13}C_2$, ^{15}N]-GSH. After 1 h, the device was rinsed by flowing the buffer into all three inlets for 5 min at 20 μL min^{-1}. The clamp was disassembled, the PDMS layers were peeled off of the chip, and the chip was rinsed with ethanol, water, and acetone. A solution of 2',4',6'-trihydroxyacetophenone monohydrate (THAP; ≥99.5%, Sigma-Aldrich) in acetone (25 mg mL^{-1}, 80 μL) was pipetted onto the chip. We found that the matrix crystallized more densely on the area of the monolayer in contact with the microfluidic channels, which allowed me to easily locate all 8 channels using the video camera on the MALDI TOF instrument (Autoflex III, Bruker Daltonics). iSAMDI-MS spectra were acquired in reflector positive mode using a mass range 600-3000 *m/z*. The smartbeam-II laser was operated

at 200 Hz with 125 laser pulses applied per spot using the 'medium' aperture setting. The $[M+Na^+]^+$ adducts of the GSH-alkanedisulfide and $[^{13}C_2, ^{15}N]$-GSH-alkanedisulfide were extracted using flexAnalysis software (Bruker Daltonics). The % conversion was calculated using the monoisotopic peak intensity of GSH (I_{GSH}) and the monoisotopic peak intensity of $[^{13}C_2, ^{15}N]$-GSH ($I_{[13C2, 15N]\text{-}GSH}$), and plotted in Figure S2, Supporting Information.

$$\% \text{ Conversion} = 100 \times \frac{I_{GSH}}{I_{GSH} + I_{[^{13}C_2, ^{15}N]\text{-}GSH}} \qquad (3.2)$$

The response follows a linear dilution profile, demonstrating that the bottom layer generates a serial dilution and that calculating the % conversion from the extracted $[M+Na^+]^+$ adducts is quantitative.

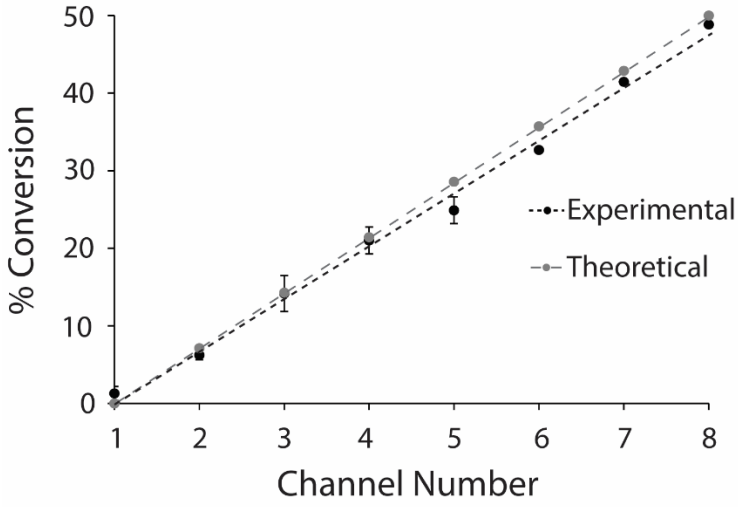

Figure 3.12 % conversion from obtaining SAMDI-MS spectra from each channel in the bottom layer.

Microfluidic experiments for determining K_m. Buffer was introduced into the top layer at 0.8 μL min^{-1}. Simultaneously, a solution of oxidized glutathione (350 μM, ≥98%, Sigma) was

injected into one inlet of the bottom layer and buffer was injected into the other inlet of the bottom layer at a flow rate of 0.4 μL min^{-1}. The device was operated for 25 min to equilibrate the flows. The top layer inlet was immediately replaced with a solution of NADPH (200 μM, ≥97%, Roche), [$^{13}C_2$, ^{15}N]-GSH (350 μM) and human glutathione reductase (865 nM, Sigma), and flowed at 0.8 μL min^{-1}. The flow rate into both inlets of the bottom layer was kept at 0.4 μL min^{-1}. The device was operated for 1 h. The clamp was disassembled, the PDMS layers were peeled off of the chip, and the chip was rinsed with ethanol, water, and acetone.

Mass spectrometry imaging. Matrix (25 mg mL^{-1} THAP in acetone) was applied by pipetting (80 μL) on top of the slide and letting the matrix solution fall to the base of the slide. A 22.0 x 18.2 mm region of interest (ROI) was selected using FlexImaging software (Bruker Daltonics). MALDI-IMS was acquired by creating an AutoXecute method as previously described.[31] Spectra were acquired with a 200 μm lateral resolution and with 125 laser shots accumulated per pixel using the 'medium' aperture setting. The laser pulse rate was 200 Hz and spectra were obtained with a mass window of 600-3000 *m/z*.

Image analysis and quantitation. Ion intensity maps were generated on FlexImaging software at 1183.2 ± 0.2 Da, 1180.2 ± 0.2 Da, and 873.2 ± 0.2 Da, corresponding to the [$^{13}C_2$, ^{15}N]-GSH-alkanedisulfide, GSH-alkanedisulfide, and maleimide-alkanedisulfide conjugate, respectively. The mis file was converted to an imzML using FlexImaging software and imported into MSiReader v1.00. A 108 x 88 pixel region downstream of the top and bottom layer junction was selected on MSiReader. Peak intensities of 1180.2 ± 0.2 Da and 1183.2 ± 0.2 Da were exported into Excel and the % conversion was determined using Equation 3.2. Three to four rows

of pixels in each channel contained GSH and [$^{13}C_2$, ^{15}N]-GSH bound to the self-assembled monolayer. The space between the channels did not have any bound analyte and the conversion in these locations were set to zero. A rectangular 108 x 88 pixel array reporting the % conversion was plotted in a heatmap (MATLAB R2016a). The flow velocity was determined using Q=Av, where Q is the volumetric flow rate and A is the cross-sectional area of the channel. The amount of time required for the fluid to flow downstream across each 200 μm pixel was calculated and plotted against the % conversion. Linear regression was used to determine the slope of each plot, and the three replicates from each channel were averaged to obtain V_0. The initial velocities were plotted as a function of GSSG concentration and fitted to the Michalis-Menten model (Enzyme Kinetics Module, SigmaPlot 12.0, Systat Software).

Ablation spot diameter determination. The microfluidic device was operated with hGR, GSSG, NADPH, and [$^{13}C_2$, ^{15}N]-GSH. MALDI-IMS was acquired as previously described. The diameter of 80 ablation spots were recorded using a stereozoom microscope (Nikon SMZ1500) and NIS-Elements D 3.0 software (Nikon).

Chapter 4

Using Microfluidics and Imaging SAMDI-MS to Characterize Reaction Kinetics

This work was performed in collaboration with Patrick O'Kane and Blaise Kimmel.

4.1 Introduction

Microfluidic systems have shown unprecedented levels of precision, miniaturization, and operational control over traditional benchtop and batch-based reactions. For example, Hollfelder and coworkers analyzed a chemical reaction with a rate constant ~ 3 x 10^4 M^{-3} s^{-1} by fusing two droplets containing the reactant and recording the reaction progress with a camera operating at 2 kHz.[83] Microfluidic devices have also been designed to screen reaction conditions. Cremer and coworkers built a device that can screen 36 temperatures for the synthesis of CdSe nanocrystals, 14 temperatures for studying lipid bilayer phase transition, and 14 temperatures for the activation energy of alkaline phosphatase.[84] However, analysis of reaction progress in microfluidic devices has been mainly limited to optical methods, which require the use of fluorescent or UV-adsorbing products that limit applicability towards a small subset of chemical reactions.

Mass spectrometry is a powerful analytical technique that, when properly integrated with fluidics, can address these limitations by analyzing mixtures of compounds without the need for labels in a straightforward way. Recently described approaches have coupled microfluidic outlet streams directly to ESI-MS[85–87] or combined matrix with outlet droplets for subsequent analysis by MALDI-MS.[88–90] These methods highlight the benefits of integrating unbiased detection strategies with microfluidics to provide high-throughput experimental data. However, ESI-MS and MALDI-MS require sampling an appreciable volume from the reactor outlet, and salts (as well as some solvents) adversely affect instrument performance, thus sacrificing sensitivity and

temporal resolution on product conversion. Mass spectrometric approaches that are sensitive, high-throughput, and do not require product workup will present new opportunities for on-chip chemical reaction monitoring.

In this chapter, we use imaging self-assembled monolayers for matrix-assisted laser/desorption ionization mass spectrometry (iSAMDI-MS) to describe the kinetic profile of a chemical reaction. In contrast to typical applications of fluidic approaches that sample product from the outlet stream or use optical tools for measuring reaction progress, we designed a device that incorporates a chemically defined self-assembled monolayer on the floor of the channel that can be directly analyzed with a MALDI-TOF mass spectrometer. This monolayer is functionalized to covalently bind the reactant and product from the flow above; therefore, it samples the reaction mixture as it flows through the microfluidic channel. The monolayer therefore collects a spatiotemporal record of the reaction, which can later be read and quantified using iSAMDI-MS. We also show how models of the dispersion front of the flow were necessary to analyze the images and extract the second order rate constants for the reaction. In the example we present here, we quantified 15,720 data points using only 160 μL of reagent and we determine the pH-dependent rate constants for a chemical reaction.

4.2 Design Rationale

We designed a microfluidic device for monitoring the progress of a chemical reaction, as described in Figure 4.1. The device has two inputs − one for each reactant − that diffusively mix at the base of a Y-junction and travel along the length of a single, unidirectional channel. The floor of the microfluidic device is functionalized with a self-assembled monolayer that

covalently immobilizes the thiol-containing reactant and product by reaction with a maleimide group on the monolayer.[91] In this way, the monolayer records the reaction progress and the distance from the Y-junction corresponds to the reaction time. Removal of the microfluidic cassette from the bottom substrate reveals the monolayer that contains a spatiotemporal record of reaction progress, which can be analyzed by iSAMDI-MS.

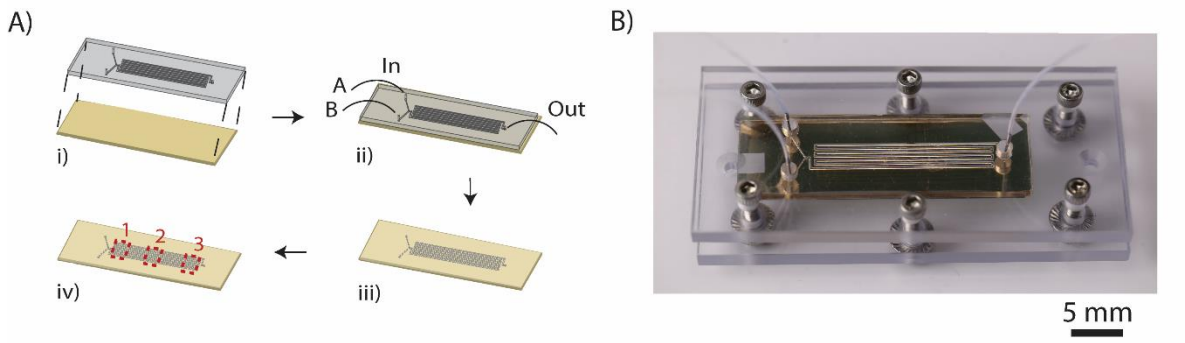

Figure 4.1 Chemical reaction kinetics microfluidic platform design. A) Design and operation of the microfluidic device. i) A PDMS structure with the fluidic design is joined to a gold-coated slide functionalized with self-assembled monolayer. ii) Reactants A and B are simultaneously injected into the respective inlet. iii) The PDMS chip is removed and matrix is applied to the slide. iv) iSAMDI-MS is used to quantitate immobilized reactants in three regions on the slide. B) A photograph of the microfluidic chip and clamp assembly.

4.3 Results

Peptide ligation reaction. We recently identified a novel chemical ligation reaction in which an α-keto aldehyde reacts with a peptide containing an N-terminal cysteine residue to join the two molecules by way of an α-hydroxy amide bond (Figure 4.2A). This reaction can be understood from previous work that showed methylglyoxal reacts with free thiols in aqueous solution to generate a lactyl thioester.[92,93] We observed that the corresponding reaction with a peptide having an N-terminal cysteine underwent subsequent intramolecular acyl transfer to generate the amide product, in analogy to native ligation reactions.[94]

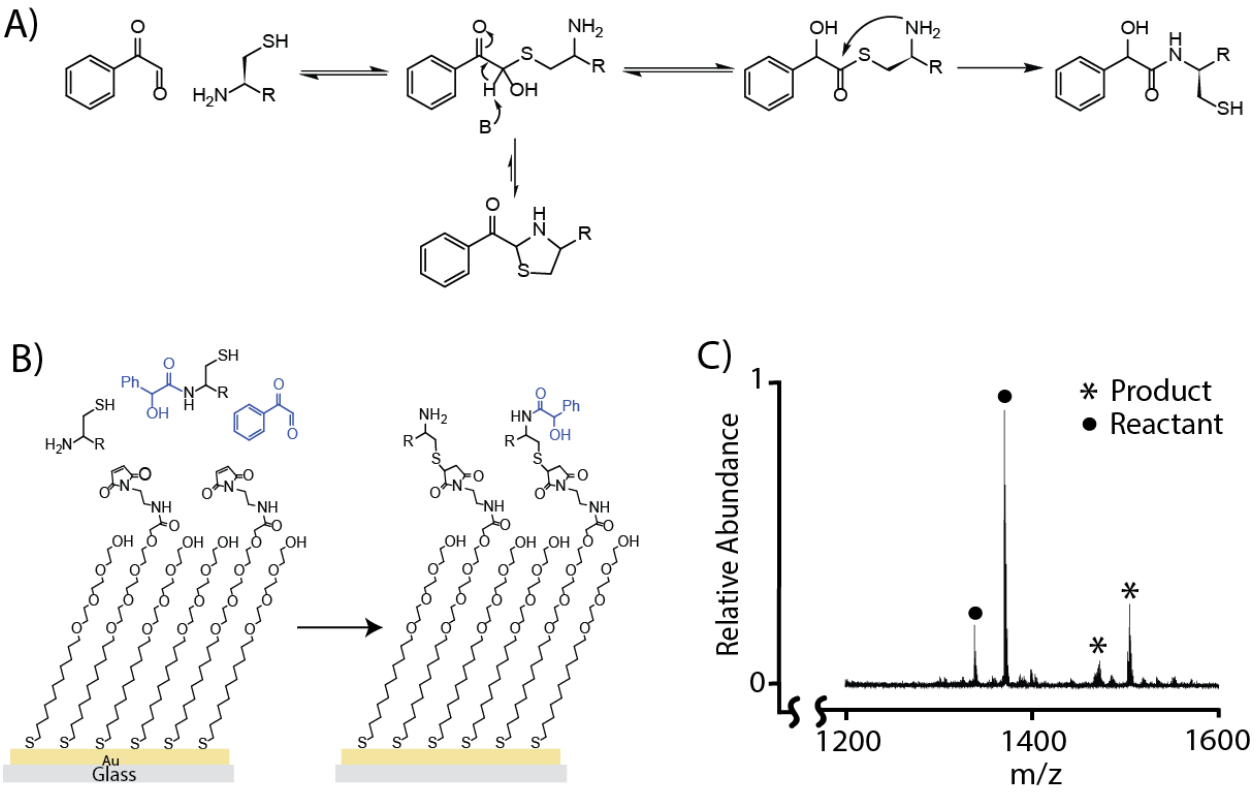

Figure 4.2 Ligation reaction schematic and SAMDI-MS detection. A) Mechanism for the ligation reaction used in this work. B) Self-assembled monolayer presenting maleimide groups reacts with the cysteine-terminated peptide and its adduct. C) SAMDI-MS spectrum of the monolayer after immobilization of the reaction product.

In the work described in this chapter, we use phenylglyoxal because it lacks enolizable protons that could lead to side products. Also, both the reactant peptide and ligation product contain a free thiol that enables them to be covalently captured onto the maleimide-functionalized self-assembled monolayer for detection (Figure 4.2B). We note that these species may also reversibly form a thiazolidine ring, which is observable by MALDI-TOF mass spectrometry of the reaction mixture but is not observed by SAMDI-MS because it does not contain a free thiol for immobilization (Figure 4.3). The SAMDI-MS spectra of the ligation

reaction show peaks corresponding to immobilization of the unreacted peptide and the ligation product (Figure 4.2C).

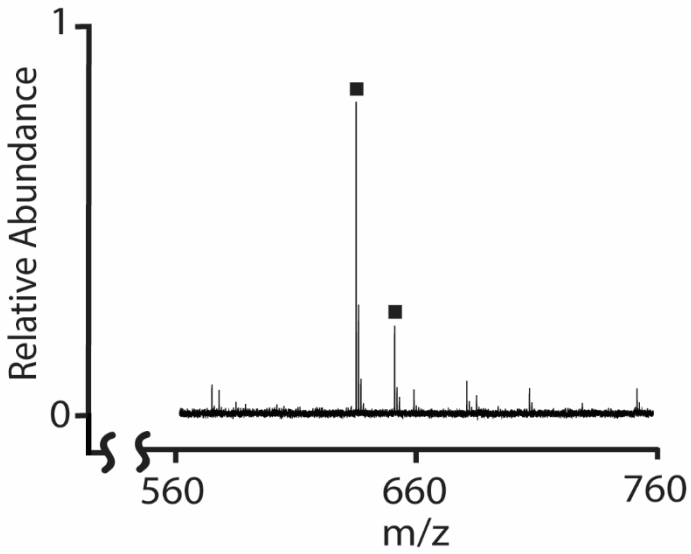

Figure 4.3 MALDI-MS spectrum of thiazolidine ring. Black boxes identify thiazolidine ring peaks.

Microfluidic device design and operation. We performed the peptide ligation reaction in a poly(dimethylsiloxane) (PDMS) microfluidic device containing a Y-shaped microfluidic channel with two inlets and one outlet. We cast the PDMS block from 3D printed masters to avoid the use of a cleanroom and to enable rapid design prototyping (Figure 4.4).[44] Separate solutions of phenylglyoxal and the peptide, each at a concentration of 2 mM, were simultaneously injected into separate inlets and allowed to diffusively mix at the base of a Y-junction, where they continued to react as the solution flowed along a single channel that was 340 mm long, 550 μm wide, and 250 μm tall. In the flow, we included a peptide (0.25 mM) lacking an N-terminal cysteine that is unable to undergo internal rearrangement to form the permanent hydroxy-amide bond. This served as an internal standard for monitoring imaging

performance and consistency. The thiol-containing peptide reactant, hydroxy-amide ligated product, and calibrant underwent immobilization to the monolayer as the fluid front flowed down the channel. The monolayer presents maleimide at a density of 20% relative to a tri(ethylene glycol) background and once saturated, it serves as a record of the reaction profile from the channel. After flowing the reactants through the device, we removed the PDMS block from the chip and applied matrix to the chip as previously described.[95]

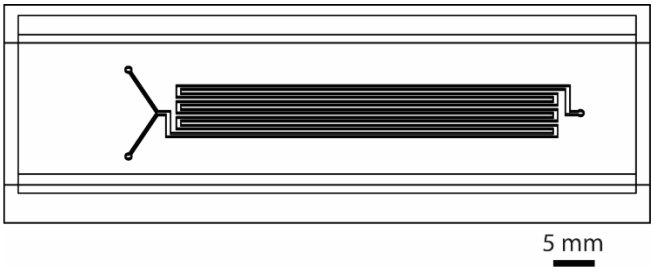

Figure 4.4 SolidWorks rendering of the PDMS master.

We used imaging mass spectrometry (iSAMDI-MS) to generate mass intensity maps of the molecules immobilized to the monolayer, as described by us recently.[95] iSAMDI-MS acquires individual SAMDI-MS spectra corresponding to each pixel, where each pixel (i.e. spectrum) reports the chemical composition of the fluid above the self-assembled monolayer. The resulting dataset therefore serves as a spatial map of mass spectra containing maleimide-terminated alkanedisulfides functionalized with the reactant and product, and which represent the extent of reaction at each position in the channel. These pixels correspond to a distinct reaction time (depending on the position down the channel and the flow rate in the channel) and therefore provide a kinetic profile for the reaction (Figure 4.5A). Here, we used iSAMDI-MS to image three regions by acquiring spectra in reflector positive mode with a 200 μm lateral resolution.

We performed experiments where the pH of the buffer was either 6.8, 7.2, 7.6, or 8.0; the spatial maps of hydroxy-amide conversion at each pH are plotted in Figure 3B. Each iSAMDI-MS dataset includes approximately 1,200 individually addressable reactions that occurred in the microfluidic device.

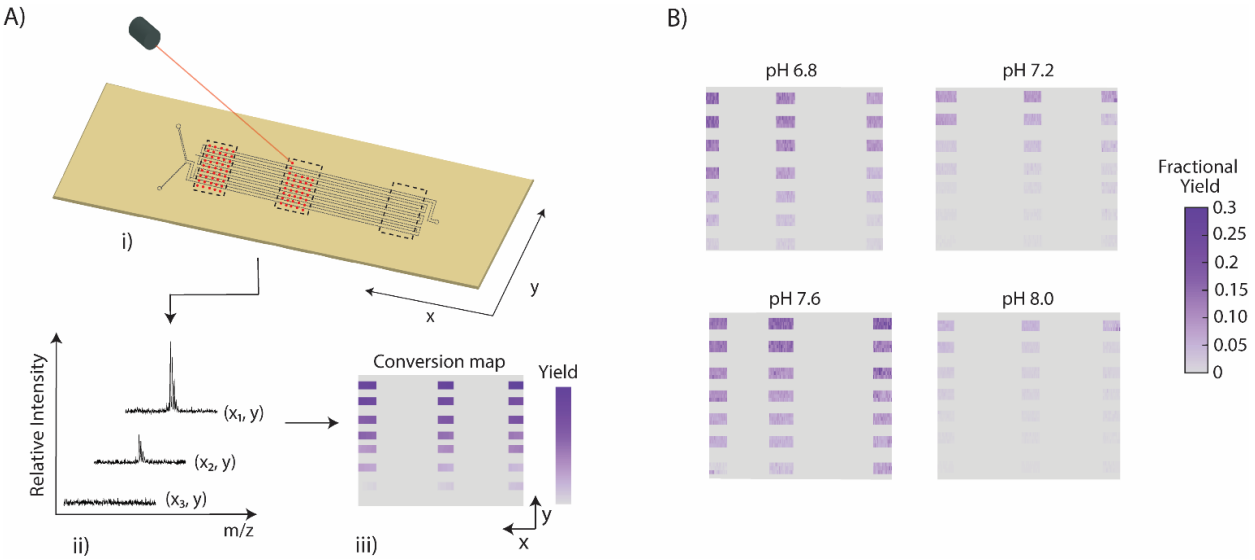

Figure 4.5 iSAMDI-MS procedure and output. A) iSAMDI-MS procedure. i) Three measurement regions on the chip are scanned with a MALDI-MS laser. ii) Each spectrum represents a pixel in the measurement region, and the product yield increases along the channel length. iii) The product yield is extracted from each pixel and plotted into a heatmap. B) Heatmaps of fractional product yield at pH 6.8, 7.2, 7.6, and 7.8.

Determining Fluid Velocity, Immobilization Rate and Dispersion Characteristics. We determined the fluid velocity inside the channel in order to determine the exact relationship between position on the surface and reaction time in the channel. A solution of 1 mM fluorescein was injected into both inlets and flowed at a rate of 0.1 µL min^{-1}. We obtained images of the fluid front passing through a 12 mm x 12 mm region of the reactor at 30-s intervals with a confocal microscope (Figure 4.6A). The average fluorescence intensities in 14 regions (each 200 µm x 600 µm) were plotted against time (Figure 4.6B, Figure 4.7). The resulting curves were fit

with a sigmoidal function and the time at which the curves reached half the maximum intensity was plotted against the distance from the Y-junction (Figure 4.6C). We fit the plot with linear regression to obtain the velocity of the fluid through the channel. The experimentally determined fluid velocity of 1.96 mm min^{-1} is 35% greater than the fluid velocity calculated from Q = Av, where Q is the volumetric flow rate and A is the cross-sectional channel area. The 3D printed PDMS masters had rounded corners instead of sharp 90-degree edges and light pressure was applied from an external clamp to keep the PDMS and chip together. We believe that both factors decreased the cross-sectional channel area and contributed to an increase in observed fluid velocity. We also determined the average dispersion coefficient across the three fluorescein experiments to be 0.71 mm^2 s^{-1} using Equation 4.1:

$$E_{max} = \left(\frac{4\pi D}{uL}\right)^{-\frac{1}{2}} \qquad (4.1)$$

The calculated Peclet number was 836, suggesting that the convective flow of the fluid had a greater effect on the reaction rate than diffusive transport of the peptide species. Thus, the axial dispersion model (ADM) better describes this system.

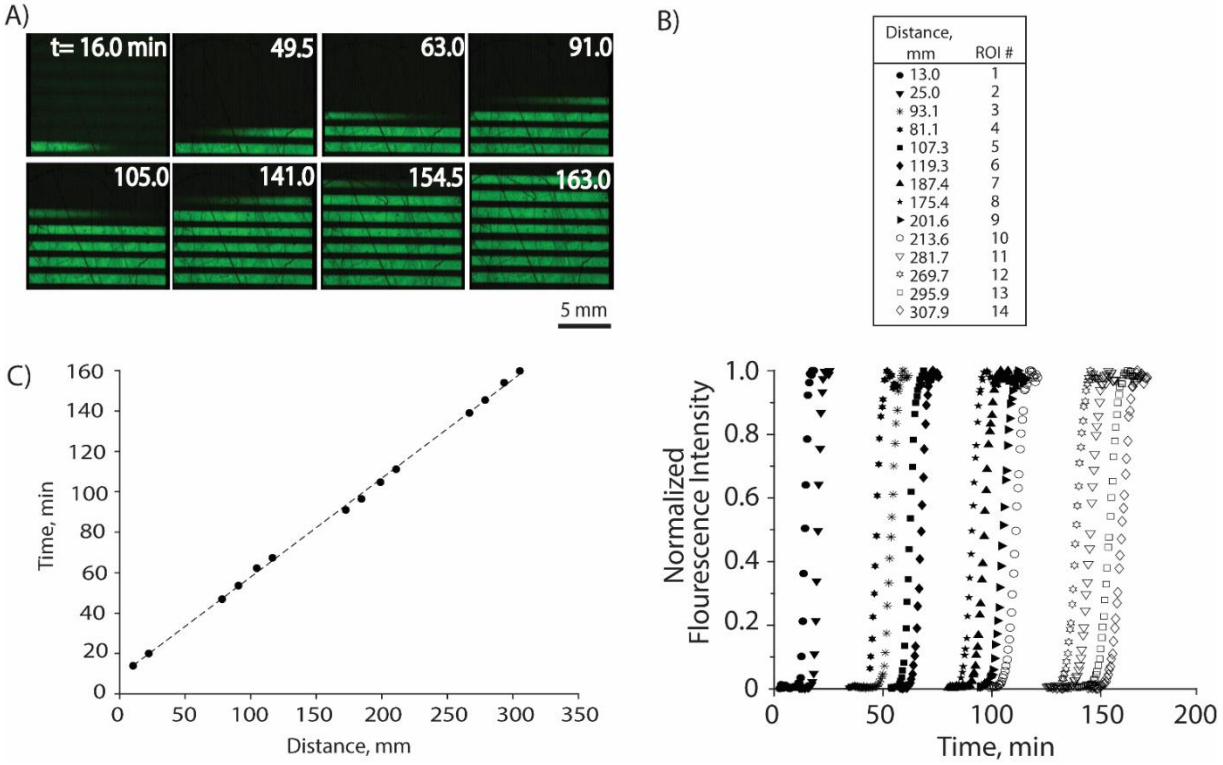

Figure 4.6 A) Fluorescein was injected into the device channel at a concentration of 1 mM and a confocal microscope was used to image the flow through the device. B) Fluorescence intensity was monitored for 14 distinct regions in the channel. This plot shows the normalized fluorescence intensity, relative to time, for each position. The intensity plot at each region adopts a sigmoidal profile, characteristic of dispersion in the fluid front. C) Plot of the time to half maximum fluorescence intensity at the 14 regions versus there distance down the channel provides a linear relationship where the slope gives the fluid velocity. R2= 0.99, y= 0.49x + 8.98.

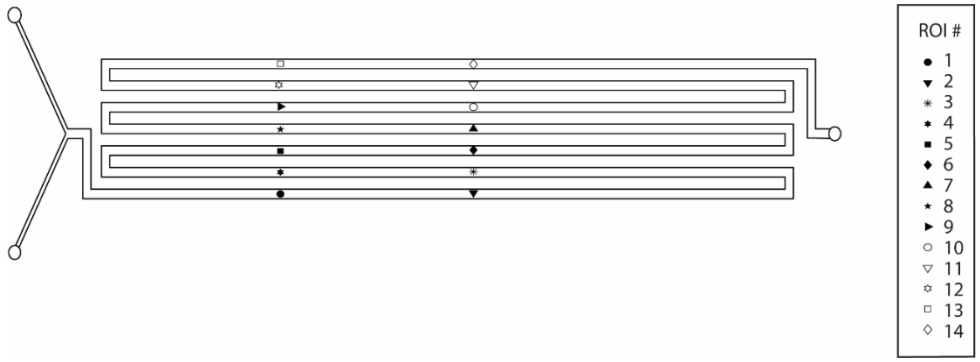

Figure 4.7 ROI locations.

We recognized that it is possible for immobilization of the reactants and products—which we collectively refer to as the ‘reaction species’ to include the reactant peptide (which was present at the same concentration as the phenylglyoxal), the ligated peptide, and the calibrant peptide—to occur from the dispersion front, where the concentration deviates from that of the bulk flow. The amount of sampling occurring from the dispersion front should be dependent on the rate of the immobilization reaction used. In order to develop a complete understanding of the system, we experimentally determined the second order rate constants for the reaction between the peptide and the maleimide on the surface. We used liquid handling robotics to dispense peptide solutions of varying concentrations and at 15 s intervals across 384-spot arrays presenting monolayers identical to those used in the microfluidic device. The reactions were rinsed from all spots after a fixed time, such that each spot recorded the immobilization yield for a unique reaction time. In this way, we generated kinetic profiles for the immobilization reaction over several peptide concentrations by performing SAMDI-MS and comparing the area under the curve of the unreacted maleimide to that of the peptide functionalized monolayer. Each concentration was fitted to a pseudo-first order rate law, as the soluble peptide is present in great excess relative to the surface-bound maleimide. The pseudo-first order rate constants were plotted against the concentration of peptide to determine the second order rate constant for the immobilization reaction (Figure 4.8).

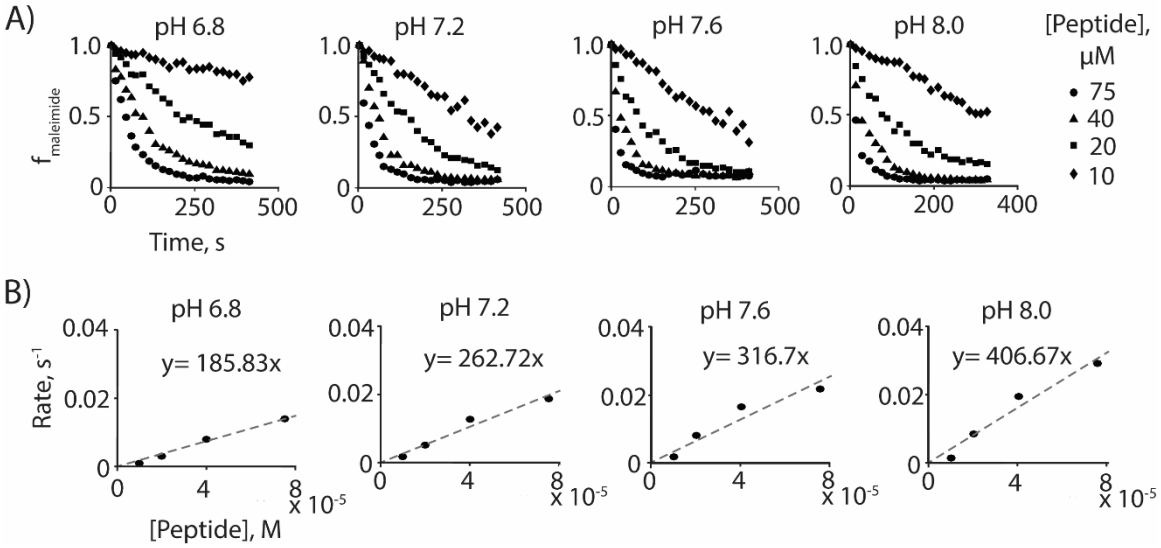

Figure 4.8 Determining immobilization kinetics of analytes to the maleimide SAM. A) For each buffer condition, the immobilization of the peptide CAK(Me_3)SA to the surface was monitored using SAMDI-MS over time and at a range of concentrations. This was used to determine the pseudo 1st order rate at each concentration of peptide, as the peptide is always present in large excess relative to the surface density of maleimide. B) For each pH, the pseudo 1st order rate constants were ploted relative to the concentration of peptide, giving a linear relationship where the slope is equal to the 2nd order rate constant for the reaction between the solution phase peptide and the maleimide surface.

We determined the rate constants for immobilization to be 186, 263, 317, and 407 M^{-1} s^{-1} at pH values of 6.8, 7.2, 7.6, and 8.0, respectively. These data show that reaction of the thiols with maleimide is quite fast and that the rate increases with pH. These rapid immobilization rates also suggest that significant immobilization of reactants likely occurred in the region of the dispersion front, where the concentration of the reaction species was well below that of the concentrations in the steady state flow. We also calculated the Damköhler number for this reaction. The Damköhler number is a dimensionless parameter defined by the ratio of the rate of immobilization to the rate of convective mass transfer (Equation 4.2). We found the Damköhler number to be greater than 1 for all pH conditions described above, showing that the

immobilization kinetics are not only fast, but that immobilization to the surface is rapid relative to the flow rate in the channel. This further suggests that it is necessary for us to develop a model of immobilization to account for the effects of dispersion.

$$Da = \frac{kC_{a,0}^{n-1}}{\frac{u}{L}} \qquad (4.2)$$

Incorporation of Dispersion with Immobilization Kinetics. We used MATLAB to produce a model that simulates the concentration profile of the phenylglyoxal ligation reaction species in the dispersion front. The model also uses the rate constant for immobilization to build a description of the immobilization kinetics which incorporates the concentration gradient found in the dispersive regime. We first used the rate law describing the immobilization of the reaction species to the floor of the channel (Equation 4.3), where *k* is the second order rate constant for immobilization to the surface, Γ is the surface density of maleimide, and *g(t)* represents the total concentration of the reaction species. We modeled *g(t)* using the fluorescein imaging experiment presented in the previous section. The curves plotted in Figure 4.6B show normalized fluorescence intensity tracked at various positions along the channel as fluorescein was injected at a concentration matching that of the peptide in the ligation reactions. The sigmoidal shape of the curves is due to the dispersion front and this front is elongated at positions further down the channel. To obtain *g(t)*, a standard 4-parameter sigmoidal function (Equation 4.4) was fit to these fluorescence profiles. The monolayers used in this work present maleimide-terminated alkanethiolates at an initial density of 1.53×10^{-10} mol cm^{-2} (Γ).[96]

$$\frac{d\Gamma}{dt} = -kg(t)\Gamma \qquad (4.3)$$

$$g(t)=\frac{a+b}{1+\left(\frac{t}{c}\right)^{d}} \qquad (4.4)$$

Integration of Equation 4.3 gives the kinetic model that describes the immobilization of the reaction species to the channel floor in the dispersive region of flow. In Figure 4.9, we plot the time-dependent density of immobilized reaction species for each pH and at two fixed points in the channel (region 1 and region 14, representing positions near the beginning and end of the channel). The plots also show the solution phase concentration profile, *g(t),* for those same fixed positions in the channel.

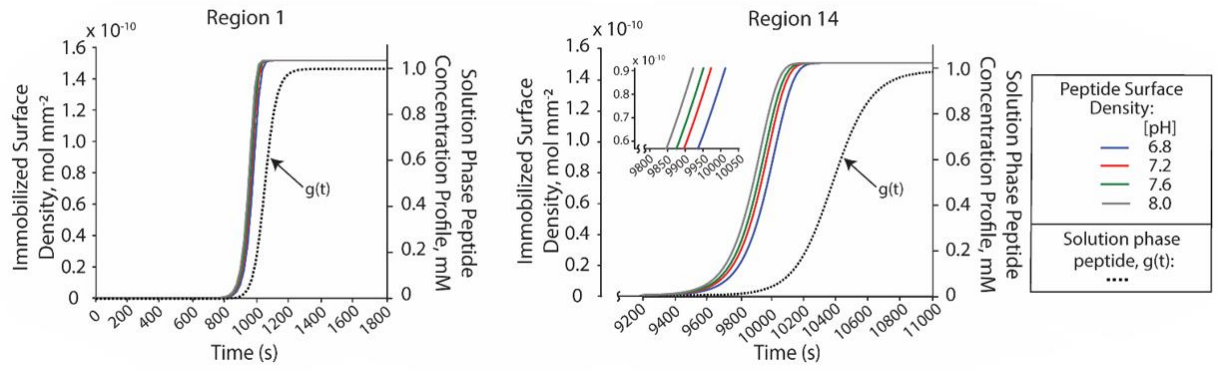

Figure 4.9 A model of immobilization occurring in the channel that incorporates both dispersion and the experimentally determined rate constants for the reaction between the maleimide surface and solution phase peptide. The plots show the pH dependent immobilization (colored lines, left y-axis) alongside the solution phase concentration and dispersion front (dashed line, right y-axis) for two fixed positions in the channel. Region 1 is a position early in the channel and region 14 is a position at the end of the channel (Figure 4.7). The inset highlights the effect of pH on the maleimide immobilization chemistry. Due to the rapid rate of immobilization, complete surface coverage is achieved before the dispersion front passes across the surface for all pH condition.

This model shows that in all cases, the immobilization reaction is completed before the bulk concentration is achieved in the flow (that is, before the dispersion front has passed over the

surface). When looking at a position near the end of the channel, broadening of the dispersion front leads to an even greater deviation between the concentration sampled by the surface and the concentration in the bulk flow. Additionally, the time required for complete immobilization increases as the dispersion front elongates. As the pH of the reaction increases, the rate constant for immobilization also increases, leading to saturation of the surface at earlier points in the dispersion front (Figure 4.10).

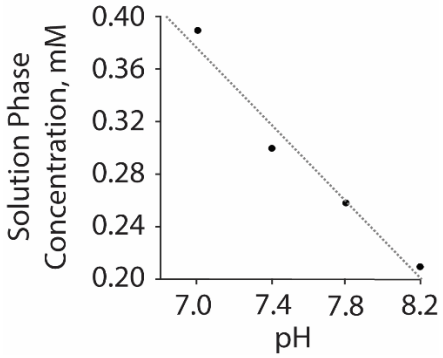

Figure 4.10 Average solution phase concentration at surface saturation v. solution pH (R^2= 0.9668).

Determination of Phenylglyoxal Ligation Kinetics. Finally, we used this model to analyze 14 positions in the channel for each pH condition, and to determine the time-weighted average concentration of reaction species during the immobilization at each position. To do so, we determined the time at which the reaction with the surface reached completion and then used this time as the upper limit for integration of the rate law (Equation 4.3), giving the average concentration for the soluble reaction species at the surface (Figure 4.11A). In this analysis, time and position in the channel are equivalent representations of reaction progress.

Returning to the iSAMDI-MS heatmaps of the channel floors after the reaction, each pixel gives the fractional yield of the reaction at the corresponding position in the channel. To determine the second order rate constant for the reaction of phenylglyoxal and the peptide in the channel, we first determined the concentration of the product in the channel (at each pixel) by multiplying the fractional yield observed by mass spectrometry by the concentration determined by our model. This concentration represents the yield of the ligation reaction at any given point in the channel. To determine the second order reaction rate constant for the ligation reaction, we plotted the reciprocal of the concentration of the reactant peptide over time (Figure 4.11B). The slope of these plots gives the second order rate constant of the reactions, which we determined to be $0.38 \pm 0.06\ M^{-1}\ s^{-1}$, $0.48 \pm 0.04\ M^{-1}\ s^{-1}$, $0.62 \pm 0.05\ M^{-1}\ s^{-1}$, and $0.62 \pm 0.01\ M^{-1}\ s^{-1}$, at the respective pH values of 6.8, 7.2, 7.6, and 8.0These rates that we obtain are comparable to those for native chemical ligation reactions of thioesters and N-terminal cysteine residues.[97] Native chemical ligation also begins with nucleophilic attack by the thiol of a cysteine residue on a thioester, and competes with an irreversible thiol-to-amine acyl transfer. We observe that our reaction is pH-dependent, where an increase in pH from 6.8 to 7.6 yields an increase in rate but an increase in pH from 7.6 to 8.0 leads to no significant change. The pKa of an N-terminal amine and cysteine are 8.0[98] and 8.5,[99] respectively, and explains our observed pH rate dependency.

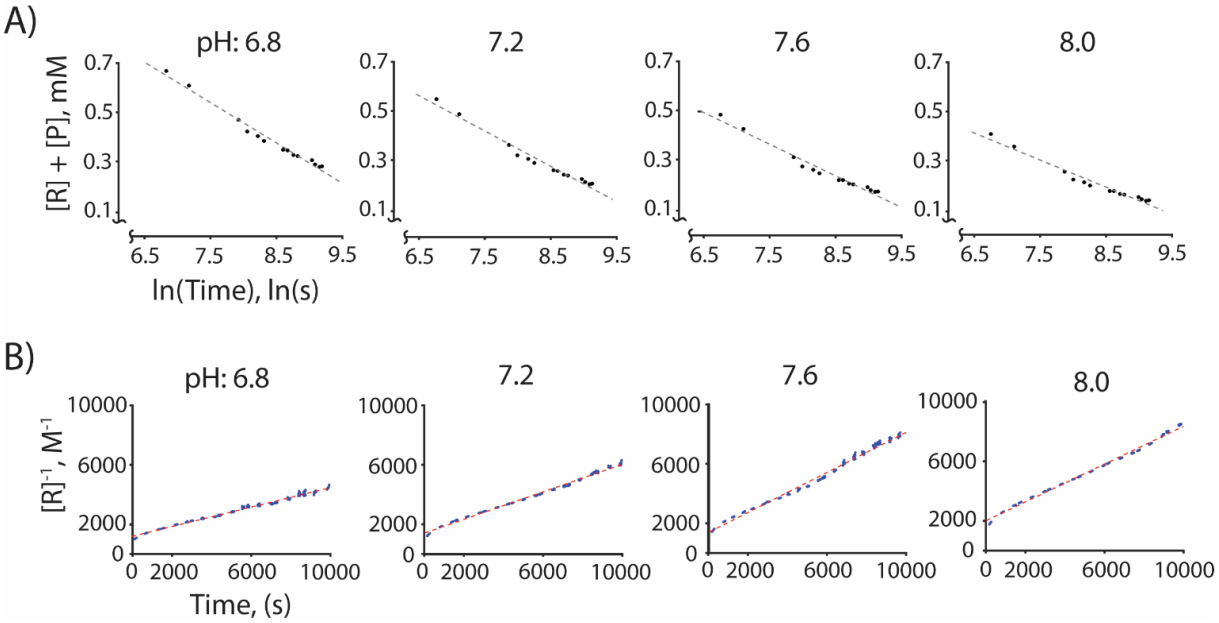

Figure 4.11 A) Here, t = time in seconds. Across each pH condition, our model of immobilization kinetics was used to determine the solution phase concentration of reaction species sampled by the surface. The plots presented here show the solution phase concentration sampled by the surface as it relates to time (i.e., position in the channel). [R] + [P] represents the combined solution phase concentration of reactant peptide and ligated peptide product. The concentration sampled by the surface adopts a logarithmic trend with respect to position in the channel, with the concentration sampled by the surface decreasing for positions further along the length of the channel. B) The concentration sampled by the surface was multiplied by the fractional yield of the ligation reaction determined experimentally from imaging the channel floor with iSAMDI-MS. This gave the absolute yield of the ligation reaction for all positions imaged in the channel, which was plotted according to a standard second order rate plot. The plots for each pH condition are seen here and adopt, well behaved, linear relationships where the second order rate constant is given by the slope.

4.4 Discussion

In this chapter we demonstrate how iSAMDI-MS can be used to characterize the rate constant for a chemical reaction at a temporal resolution and with an amount of reactant that would be impractical to perform using current approaches. By performing reactions in flow and recording the reaction progress through covalent immobilization of the reactant and product to

the floor of the channel, the temporal resolution is determined by the reaction flow rate and the spatial resolution of the MALDI mass spectrometer. Here, we image the surface at a pixel resolution of 200 μm, which corresponds to a temporal resolution of 6.1 s. Further, we acquired a total of 15,720 spectra and analyzed these data to obtain pH-dependent rate constants for the reaction between an N-terminal cysteine and phenylglyoxal.

One challenge with microfluidic devices is the dispersion zone that separates regions of fluid with different compositions. This is one reason why segmented flow methods have been developed to localize reagents into droplets or plugs.[100,101] Our approach was less compatible with the segmented formats because the monolayer must be in direct contact with the flowing reactants. Yet, the rapid immobilization kinetics for the reactants meant that we were not capturing product from the steady-state region of the flow but rather from the dispersion front. To relate the immobilization kinetics to the concentrations of these molecules in the flow, we developed a model that simulated the dispersion and used experimentally-determined immobilization rate constants to simulate the amount of reactant and product that underwent immobilization. In this way, we could relate the density of product on the surface to the concentration of product in the steady state flow, and therefore we could extract the true second order rate constant for the reaction. This work is significant because it describes the first microfluidic device operating under continuous flow that uses an in-situ capture reaction to overcome dispersion.

A corresponding limitation of this approach is that it requires that the reactants and products contain a functional group to enable immobilization. The maleimide chemistry used in this work requires thiols for immobilization. However, we note that many other reactions,

developed by our group and others, can be used for immobilization, including alkynes and azides, activated esters and amines, Diels-Alder reactants, and others.[91,102–107] We have also recently described a traceless immobilization method that uses a photogenerated carbene to rapidly and covalently immobilize a broad range of molecules, and this may serve as a more generalizable immobilization strategy in future applications.[108] Hence, we anticipate many ways in which the methodology described here can be applied to other reactions.

By integrating the reaction steps with product isolation in a single device, we simplify the analysis of rate constants and minimize manual reagent handling. Previous combinations of microfluidic systems and mass spectrometry have required the collection of the reaction products by arraying on a second substrate (for MALDI-MS) or directly interfacing the device with a mass spectrometer. Both are time-consuming and can generate uncertainty in the kinetic profile if the reactions are not adequately quenched or are not sampled properly. In addition, it is difficult to integrate bulky equipment with microfluidic devices. Here, we simply rinse out the remaining reagent from the fluidic device, remove the chip entirely from the fluidic element, and acquire iSAMDI-MS directly from the chip.

Finally, we note the efficiency of this approach offers in performing high throughput experiments. We acquired approximately 1,200 data points from each device using 12 µL of reagent, which corresponds to 10 nL of reagent for each data point. Current commercial mass spectrometers can perform iSAMDI-MS at a resolution of over 15 million data points with 10 µm pixel resolution. Reactions that consume picoliter volumes of reagent will be possible with devices that contain nanometer-scale channels and reaction wells.[109,110] In addition, devices can be designed to contain multiple reaction channels for parallel reaction screening.

In summary, we developed an approach based on SAMDI mass spectrometry that performs high throughput experiments in microfluidic cells to determine the rate constant for a chemical reaction. This approach is enabled by the use of self-assembled monolayers on the floor of the channels, which allows both for selective immobilization of reactants and direct analysis by SAMDI mass spectrometry. This approach allows for massively parallel experimentation using minimal reagent and does not require tedious approaches for isolating reaction products or for labels used to quantitate products. We expect that this and related work will find use in combinatorial chemistry and drug screening applications.

4.5 Experimental

Self-assembled monolayer preparation. Standard glass microscope slides were cleaned in ethanol and then water in a sonication bath. An electron beam evaporator (Thermionics VE-100, Thermionics) was used to deposit 5 nm of Ti (0.02 nm s^{-1}) followed by 30 nm of Au (0.05 nm s^{-1}) at a pressure 1-8 x 10^{-6} Torr. The slides were immersed 16 h at 25 °C in an ethanolic solution (0.5 mM total disulfide concentration); the solution had a 1:4 ratio of an asymmetric disulfide terminated with a maleimide group and tri(ethylene glycol) group, to a symmetric disulfide terminated with tri(ethylene glycol) groups.[91] The slides were then rinsed with ethanol and then water, and dried with a stream of nitrogen.

Microfluidic device fabrication. The PDMS master was rendered on SolidWorks software (Dassault Systémes SolidWorks Corporation) and had two 800 μm diameter inlets and one 800 μm diameter outlet (Figure 4.4). The long, winding reaction channel was 250 μm tall and 550

μm wide. The 3D printed masters were prepared for PDMS polymerization as previously described.[44] A 0.8 mm biopsy punch was used to form the inlets and outlet in the PDMS block. The PDMS block was treated with 50 W air plasma for 35 s at 200 mTorr (Solarus Plasma Cleaner, Gatan, Inc.) to render the PDMS surface hydrophilic. The PDMS was then aligned with the gold-coated slide functionalized with the self-assembled monolayer. The PDMS and gold slide assembly were held together using light pressure from an external clamp made from extruded polycarbonate secured with 6 screws. The clamp had three 1.5 mm diameter holes that matched the location of the two inlets and outlet of the device.

Microfluidic device operation. Polytetrafluoroethylene (PTFE) tubing (0.042" outer diameter, Cole-Parmer) was inserted into the outlet via stainless steel catheter couplers (22 ga x 15 mm, Instech) and the device was primed with buffer using a syringe pump (PhD 2000, Harvard Apparatus). The outlet was disconnected from the syringe pump while keeping the tubing and catheter in the PDMS block. The priming process was repeated by flowing buffer through the two inlets. The device was placed inside a heat block at 37 ° C and the top of the heat block was covered with styrofoam and aluminum foil to fully enclose the device. Buffer was flowed through both device inlets at 0.1 uL min^{-1} for 1 h to allow the device to equilibrate. Simultaneously, a solution of phenylglyoxal in buffer (2 mM) was injected into one inlet at 0.1 μL min^{-1} and a solution of reactant peptide in buffer (2 mM) and calibrant peptide (0.5 mM) was injected into the other inlet at 0.1 μL min^{-1}. After mixing, each reactant was present at 1 mM and the calibrant was present at 0.25 mM all in buffer containing 100 mM BisTris, 10 mM phosphate and 4 mM $MgCl_2$. Importantly, this buffer system contains no nucleophilic amines that may react

with the phenylgloxal. After 4.5 h, buffer was flowed through both inlets at 100 µL min^{-1} to rinse the device. The PDMS block was removed from the chip and the chip was rinsed with ethanol, water, and acetone. This experiment was repeated across buffer pH's of 6.8, 7.2, 7.6, and 8.0.

Mass spectrometry imaging. Matrix (25 mg mL^{-1} THAP in acetone) was applied by tilting the slide at a 45 ° angle, pipetting matrix (80 µL) on top of the slide and letting the matrix solution fall to the base of the slide where excess matrix was absorbed by a Kimwipe. Three ~ 5 mm x 9 mm regions of interest (ROIs) were selected at the beginning, middle, and end of the device, covering all 7 serpentine channels, using FlexImaging software (Bruker Daltonics). MALDI Imaging Mass Spectrometry (MALDI-IMS) was acquired by creating an AutoXecute method as previously described.[111] Spectra were acquired with a 200 µm lateral resolution and with 125 laser shots accumulated per pixel. The laser pulse rate was 200 Hz and spectra were obtained with a mass window of 600-3000 *m/z*. The .mis file was loaded into FlexImaging software and converted to .imzML format. The FlexImaging output is shown in Figure 4.12, which confirms that the device did not leak during operation, and that the quantity of reactant decreases and quantity of product increases along the channel length.

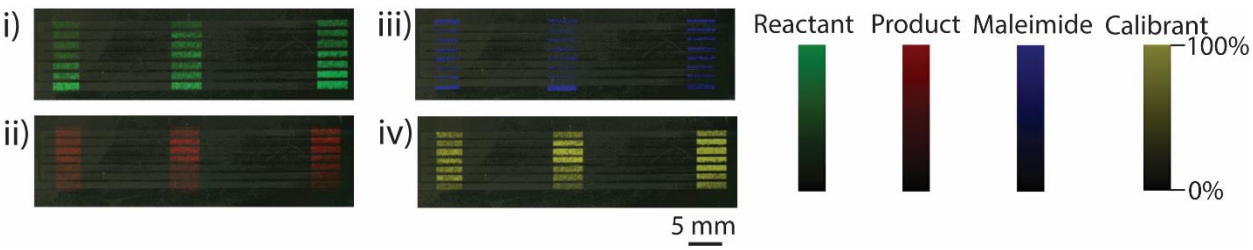

Figure 4.12 Ion maps of analyte detected with iSAMDI-MS. i) Map of the reactant-maleimide alkanedisulfide (*m/z* 1370.9 ± 0.2) visualized in green. ii) Map of the product-maleimide alkanedisulfide (*m/z* 1504.9 ± 0.2) visualized in red. Iii) Map of maleimide-alkanedisulfide (*m/z* 873.6 ± 0.2) visualized in blue. iv) Map of the calibrant-alkanedisulfide (*m/z* 1384.8 ± 0.2) visualized in yellow.

Image analysis and quantitation. The.imzML file was imported into MSiReader v1.00. The entire imaging region (including the three ROIs and all spaces in-between) was selected. Peak intensities of 1370.9 ± 0.2 Da, 1504.9 ± 0.2 Da, and 1384.8 ± 0.2 Da corresponding to the reactant-maleimide alkanedisulfide conjugate, product-maleimide alkanedisulfide conjugate, and peptide calibrant-maleimide alkanedisulfide conjugate, respectively, were exported into Excel. The fractional conversion of product was calculated using Equation 4.5:

$$\text{fractional conversion} = \frac{I_P}{I_P + I_S} \qquad (4.5)$$

where I_P is the monoisotopic peak intensity of the product-maleimide alkanedisulfide conjugate and I_S is the monoisotopic peak intensity of the reactant-maleimide alkanedisulfide conjugate. 3-4 rows of pixels corresponded to the self-assembled monolayer in contact with the fluidic channel and contained immobilized analyte. The pixels in between the channels did not have bound analyte, and the fractional product conversion in these channels was set to 0. A ~218 x 56 pixel array of fractional hydroxy-amide conversion was plotted in a heatmap at each buffer pH (MATLAB R2016a, Mathworks).

iSAMDI-MS ROI distance determination. The slide was viewed under a stereozoom microscope (Nikon SMZ1500) after iSAMDI-MS acquisition. The distance between the first row of ablation spots of the top ROI and the Y-junction, and the distance between the last row of ablation spots of the bottom ROI and the outlet were measured with NIS-Elements D 3.0 software (Nikon, Figure 4.13).

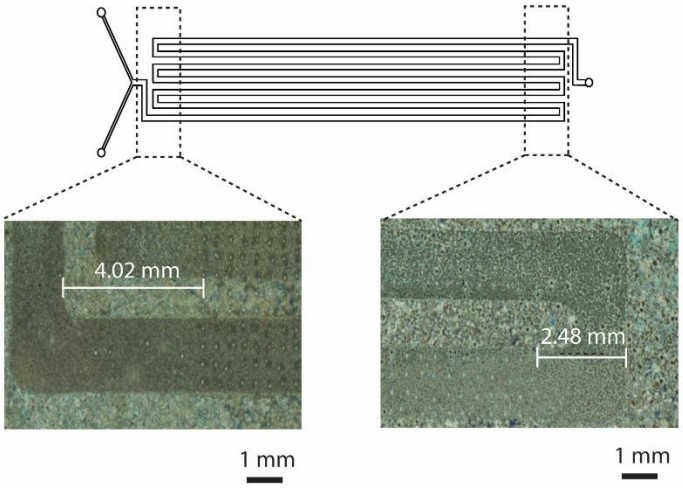

Figure 4.13 Microscope images of the chip after iSAMDI-MS acquisition. The distances between the first column of ablation spots and the channel edge are indicated.

Ionization efficiency evaluation. The relative ionization efficiencies of the reactant and product were determined to validate that the fractional yields obtained from iSAMDI-MS accurately represented the ratios bound to the SAM. Solutions of pure reactant and product were individually pipetted onto a chip functionalized with a self-assembled monolayer presenting maleimide at a density of 20% against a background of tri(ethylene glycol) groups. The solutions were incubated on the chip at room temperature for 1 h in a humidity chamber. The chip was rinsed with ethanol and then water, and THAP matrix was applied as previously described.

SAMDI-MS spectra were obtained from 125 accumulated shots with a fixed stage to simulate iSAMDI-MS acquisition conditions (Autoflex III, Bruker Daltonics). The peak intensities for the reactant- maleimide alkanedisulfide, product-maleimide alkanedisulfide, and tri(ethylene glycol) alkanedisulfide peaks were extracted with FlexAnalysis software (Bruker Daltonics). The ionization of the reactant peak and product peak relative to the tri(ethylene glycol) peak was calculated using Equation 4.6:

$$\% \text{ ionization} = \frac{I_Z}{I_Z + I_{EG3}} \times 100 \qquad (4.6)$$

where I_Z represents the monoisotopic peak intensity of the product-maleimide alkanedisulfide conjugate or reactant-maleimide alkanedisulfide, and I_{EG3} represents the monoisotopic peak intensity of the tri(ethylene glycol)-alkanedisulfide conjugate. The % ionization for the reactant and product were 21.5 ± 0.59 and 26.1 ± 1.35, respectively, demonstrating that their ionization efficiencies are approximately equivalent and that the calculated fractional conversion from iSAMDI-MS accurately represented the ratio of reactant and product bound to the self-assembled monolayer.

Flow velocity determination. The microfluidic device was assembled as previously described and primed with 100 mM Bis-Tris, 10 mM phosphate buffer (pH 7.6). Solutions of fluorescein sodium salt (1 mM, Sigma-Aldrich) were simultaneously flowed into both inlets at 0.1 μL min^{-1} for 4 h. Images of a 13 mm x 13 mm region were acquired every 30 s for 4 h using an inverted fluorescent confocal Nikon Ti Eclipse microscope (Nikon) at 1 x magnification. The distance between the leftmost pixel in the image to the channel Y-junction was determined by

moving the sample stage stepwise until the Y- junction appeared in the viewing region. The coordinates of both points were noted and used to calculate the distance of each ROI from the Y-junction. Three 200 µm x 200 µm ROIs were selected across the width of each channel on the left side and the right side of the image to yield 6 ROIs per channel (42 ROIs total) using NIS-Elements software (Nikon). The fluorescence intensity over time was extracted from each ROI and imported into Excel. The fluorescence intensity was normalized between 0 and 1. The three ROIs across each channel were averaged to yield a total of 14 normalized fluorescence intensity curves (two curves for each of the 7 channels, taken from the left side and right side of the image). Sigmoidal fits were made using SigmaPlot 12.0 software (Systat Software) and the time to reach half maximal fluorescence intensity was recorded and plotted against distance from the Y-junction. Linear regression was used to calculate the velocity of the fluid. The time-dependent solution-phase concentration profile was then described by the function $g(t)$, a standard 4-parameter sigmoidal function (Equation 4.3), where a, b, c, and d were fit by regression of the experimental fluorescein data and t represents time (MATLAB 2018 Curve Fitting Toolbox).

Dispersion coefficient determination. The stepwise function for the injected fluorescein concentration profile was modeled as a pulse by mirroring the fluid front at the maximum fluorescein concentration for each ROI in MATLAB 2018a (MathWorks). The average residence time for the fluid pulse at each spot was determined by the averaged integration of fluorescein concentration along the length of the channel. Dividing the length of the channel over the average residence time yields the superficial velocity of the channel at that point, which we confirmed by comparative analysis to our experimentally determined flow velocity. The pulse

shape was transformed into a dimensionless residence time distribution function and the curve maximum yielded the dispersion coefficient of the system.[112] The local maximum of this curve (E_{max}) has a defined relationship between the superficial velocity (*u*), length (*L*), and dispersion coefficient of the system (*D*) (Equation 4.1)

Determination of immobilization kinetics. The rate of immobilization of the thiol-containing peptide to the maleimide presenting surface was determined experimentally using 384-spot monolayer arrays, presenting the same 20% maleimide-terminated monolayer used in the microfluidic device. A Multi-Drop Combi liquid handling robot (Thermo Fisher) was used to dispense peptide solutions across the arrays, at varying concentrations and at each of the pH conditions used in the device. Reaction timepoints were generated every 15 to 20 seconds by automated deposition and the array was rinsed with distilled water at the end to stop all reactions. SAMDI-MS was performed using an AB Sciex 5800 series MALDI-TOF mass spectrometer (AB Sciex) and the yield of each reaction was quantified by integrating the area under the peak for the unreacted maleimide and the peptide coupled maleimide peaks. For each pH, the yield over time was fit to the pseudo 1st order rate law. The pseudo 1st order rate constants were then used across multiple peptide concentrations to determine the pH-dependent second order rate constants for the immobilization of the peptide to the maleimide surface.[113]

Dimensionless parameters for modeling convective flow. We considered two distinct models to describe the fluid movement through the microfluidic systems; the axial dispersion model (ADM), where the convection of the fluid dominates, and the tank-in-series model

(TISM), in which the dispersion of the fluid drives the mass transfer for the system.[114] Utilizing the dispersion coefficient for the microfluidic system, the axial Peclet number was determined as Pe = uL/D, where u is the superficial velocity of the fluid, L is the channel length, and D is the dispersion coefficient.[115] Peclet numbers greater than 100 indicate that convective mass transfer acts as the primary driving force over axial diffusion.[116] To measure time scales between the reaction kinetics and the convective mass transfer, we leveraged the Damköhler number (Da) where k is the rate constant of immobilization, $C_{a,0}$ is the initial concentration of the reacting peptide species, n is the rate order of the immobilization reaction, L is the length of the channel, and u is the superficial velocity as utilized in Equation 4.2:[117]

Chapter 5

Characterization of Enzyme-Ligand Interactions with Imaging SAMDI-MS

This work was performed in collaboration with Lindsey Szymczak.

5.1 Introduction

Enzyme-ligand interactions are important for understanding metabolic regulation, cellular signaling, and disease progression. The Hill equation is often used to characterize enzyme-ligand interactions, where the Hill coefficient (*n)* describes the degree of cooperativity and $K_{0.5}$ describes the ligand concentration required for half maximal activity. Various methods have been developed for determining these parameters, but they are challenging and not easily adapted towards high-throughput screening applications. For example, X-ray crystallography has been used to identify the degree of cooperativity by determining the crystal structure at a stepwise gradient of ligand concentration, but is limited by the ease of enzyme crystallization and is not applicable towards high-throughput applications.[118] Another approach relies on isothermal titration calorimetry, which provides precise thermodynamic and kinetic data, but is low-throughput and consumes large quantities of protein.[119] Techniques adaptable towards high-throughput screens include fluorescence polarization[120] and fluorescence resonance energy transfer (FRET)[121], but the need for labels can interfere with native enzyme activity and are not easily modified towards new binding interactions. Surface-plasmon resonance (SPR) is a medium-throughput, label-free technique that has also been used to measure enzyme-ligand interactions, but the need to attach the enzyme or the ligand to the SPR chip may compromise the binding kinetics.[122,123] Challenges in the design of enzyme-ligand binding assays limit our understanding of the roles that small

molecules play in biology, and there remains a need for high-throughput strategies to quantitatively measure enzyme-ligand interactions.

In this chapter, we describe a high-throughput strategy for determining the Hill coefficient (*n*) and ligand concentration required for half-maximal activity ($K_{0.5}$) using iSAMDI-MS. We use a 3D microfluidic device that requires only 20 μL reagent and three inputs to generate a quantitative, spatially resolved map of 3,007 data points in one experiment. We have previously shown that iSAMDI-MS can perform and analyze thousands of reactions in a single experiment for calculating the Michaelis constant and rate of a chemical reaction.[95] Here, we use iSAMDI-MS to gain insight on the processes that control ligand-induced enzyme activation.

An important feature of this method is that the native enzyme activity is used to measure the extent of ligand binding. Traditional assays do not report the on resulting enzyme activity but instead study conformational changes or ligand affinities. However, many ligand interactions activate the catalytic activity of the enzyme, necessitating the characterization of ligand binding in relation to activation. Here, we use the rate of product conversion to characterize the extent of ligand-enzyme binding.

We apply this method towards studying the Ca^{2+}-induced activation of peptidylarginine deiminase type 2 (PAD2). PAD2 is involved in the progression of several diseases, including breast cancer,[118] rheumatoid arthritis,[124] and macular degeneration.[125] PAD2 is present in the cytoplasm[126] but requires calcium concentrations nearly 10-fold greater than intracellular levels for maximal activity.[127] Therefore, assays that measure PAD2 activation are important for studying its function and guiding the design of therapeutics. Several techniques have been developed to detect PAD-mediated citrullination and have been important for furthering our

understanding of this enzyme family,[128–134] but rely on labels and secondary reporters or are difficult to adapt to high-throughput assays. We developed a label-free assay using the SAMDI-MS methodology to detect PAD2 activity. The SAMDI-MS assay allows for greater adaptability towards a wide range of enzyme types and avoids false positives and false negatives that are common in techniques that rely on labels and secondary reporters. We use this assay with iSAMDI-MS to analyze several thousand reactions on one chip and show that PAD2 binds Ca^{2+} cooperatively with a $K_{0.5}$ value in good agreement with previous results.

5.2 Results

We designed a 3D microfluidic device to conduct all mixing and reaction steps required to calculate *n* and $K_{0.5}$, as shown in Figure 5.1. The device consists of two PDMS fluidic layers− the bottom layer partitions a solution of ligand into a linear gradient of 8 concentrations and the top layer delivers a constant concentration of enzyme to the bottom layer. The bottom layer consists of a 2-input/8-output pyramidal network leading into 8 parallel Y-shaped channels. The top layer consists of a 1-input/8-output channel network. The Y-shaped channels have two inputs− one for the ligand and the other for the enzyme− that diffusively mix at the base of the junction. A junction connects the enzyme input of each Y-shaped channel to the top layer to ensure the delivery of a constant enzyme concentration to the bottom layer.

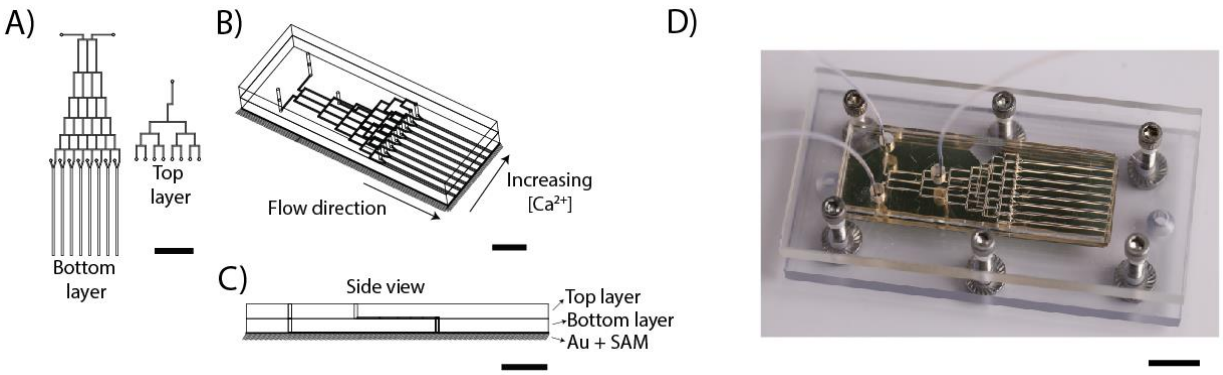

Figure 5.1 Hill kinetics microfluidic device design and assembly. A) Top view of both layers, B) Assembled device, C) Side view. Scale bar= 10 mm, D) Device and clamp assembly. Scale bar= 5 mm.

The two fluidic layers are placed on top of a chip functionalized with a self-assembled monolayer presenting the enzyme substrate at a density of 10% against a background of tri(ethylene glycol)-terminated alkanethiolates. The self-assembled monolayer was functionalized with the peptide substrate through reaction of the cysteine with maleimide. During the device operation, the enzyme in the top layer becomes partitioned into 8 channels, which enter the bottom layer and diffusively mix with the ligand at the base of each Y-junction. Upon contacting the stream of ligand, the enzyme becomes activated and modifies the peptide on the floor of the channel. After flowing the reagents through the device for 1 h, the reaction is quenched and the fluidic elements are removed from the chip. iSAMDI-MS is acquired on the chip to generate a spatial map of product yield, which is used to calculate n and $K_{0.5}$.

PAD2 catalyzes the conversion of arginine to citrulline, which results in a mass increase of 0.98 Da. This is challenging to reliably detect on a MALDI mass spectrometer, so we used trypsin to detect the presence of citrullination (Figure 5.2).

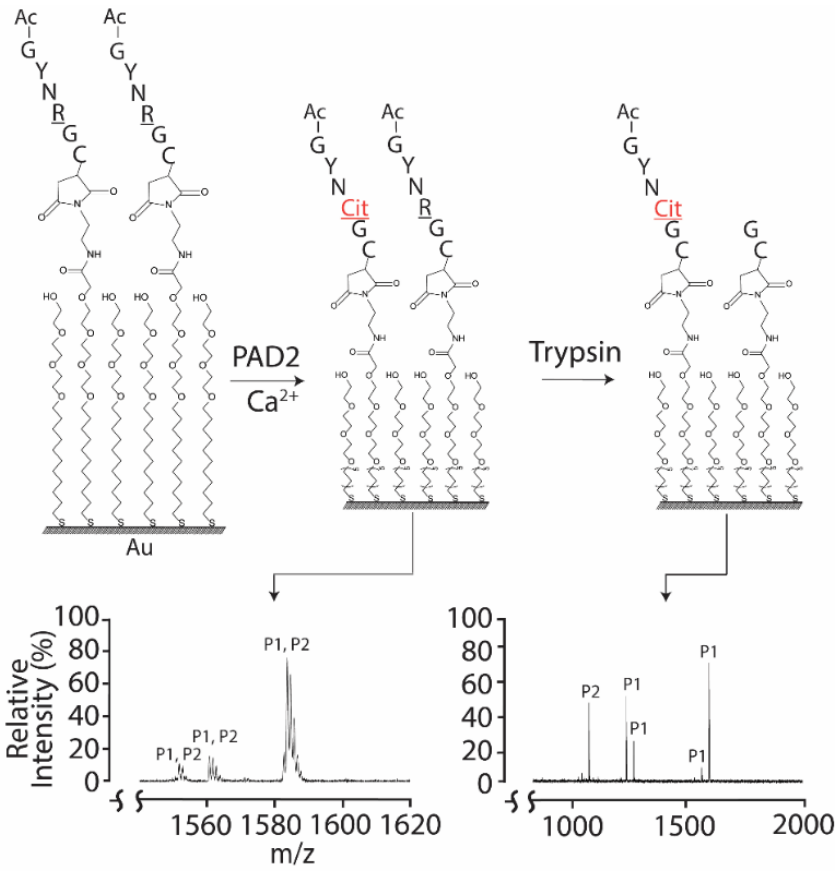

Figure 5.2 Assay for detecting PAD2 citrullination. The PAD2 peptide substrate (Ac-GYNRGC) is immobilized onto a self-assembled monolayer. The monolayer is treated with PAD2 and Ca^{2+}. Treatment of the monolayer with trypsin reveals peaks representing the un-citrullinated, proteolyzed peptide (P2) and the citrullinated peptide (P1).

Trypsin has been shown to selectively hydrolyze arginine and lysine residues, but not citrulline residues.[135] To determine the peptide sequence for use in the assay, we treated a peptide library with the sequence Ac-G**XZ**RGC (**X** and **Z** denote all amino acids except cysteine, lysine, and arginine) with PAD2 and then trypsin. We found that the sequence Ac-GYNRGC provided high PAD2 activity and signal-to-noise with SAMDI-MS (Figure 5.3).

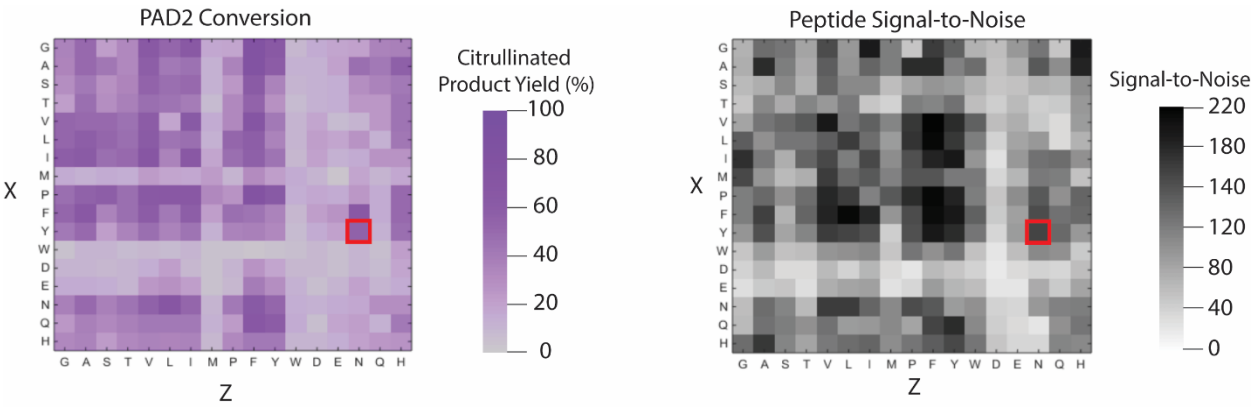

Figure 5.3 Heat maps of the Ac-GXZRGC peptide library. Left: heat map of PAD2 activity on Ac-G**XZ**RGC peptide library. Mean, n=2. Right: heat map of the signal-to-noise of the Ac-G**XZ**RGC peak in the peptide library. Mean, n=2. A red box highlights Ac-GYNRGC in both heat maps.

Moving forward with this sequence, we demonstrated that the trypsin detection strategy is quantitative by immobilizing known ratios of Ac-GYNRGC and Ac-GYNCitRGC and treating the surface with trypsin (Figure 5.4). We then calculated the percent of citrullinated peptide in the resulting spectra with the following equation:

$$\%\ \text{citrullination} = \frac{I_{Cit}}{I_{Cit}+I_R} \times 100 \qquad (5.1)$$

where I_{Cit} is the monoisotopic peak intensity of the citrullinated peptide conjugated to the maleimide-alkanedisulfide and I_R is the monoisotopic peak of the trypsinized peptide conjugated to the maleimide-alkanedisulfide. A linear response is observed with a slope approximating 1.0 (R^2= 0.9961, y = 0.9884x + 0.032), demonstrating that this method is quantitative. No proteolysis is observed when the citrullinated product is bound to the surface, while complete proteolysis is observed when the uncitrullinated substrate is bound to the surface. Together, this demonstrates that trypsin proteolysis specifically detects citrullination for use with SAMDI-MS.

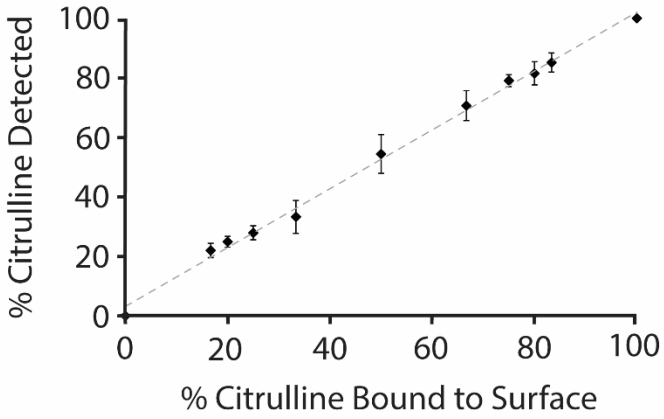

Figure 5.4. Quantitating the level of citrullination on the self-assembled monolayer. Known ratios of Ac-GYNRGC and Ac-GYNCitGC were mixed and applied to a self-assembled monolayer. SAMDI-MS spectra were aquired from each ratio and the % citrullination was quantified. The amount of citrullination was plotted against each known peptide ratio. A linear fit (R^2= 0.9961, y = 0.9884x + 0.032) shows that the phenylglyoxal modification can be used to quantitate the amount of citrullinated product. Mean ± SD, n=3.

To begin the device operation, the PAD2 substrate Ac-GYNRGC was covalently immobilized to the maleimide on the self-assembled monolayer through Michael addition of the terminal cysteine residue. The top and bottom layers were aligned on the chip presenting the substrate-functionalized self-assembled monolayer (Figure 5.5). A linear gradient of ligand was generated by injecting 1.6 mM $CaCl_2$ into one inlet of the bottom layer and buffer (100 mM Tris (8.0), 50 mM NaCl) into the other inlet at 1.0 µL min^{-1}. Simultaneously, a solution of 1.6 µM PAD2 and 200 µM tris(2-carboxyethyl)phosphine hydrochloride (TCEP) was injected into the top layer at 2.0 µL min^{-1}. The reagents were allowed to flow through the device for 1 h. During this time, $CaCl_2$ diffusively mixed with PAD2 at the base of the Y-junction and activated PAD2, catalyzing the conversion of arginine to citrulline. Afterwards, a solution of 2 mM ethylenediaminetetraacetic acid (EDTA) in 100 mM Tris pH (8.0), 50 mM NaCl was manually injected into each inlet at ~200 µL min^{-1} to quench the PAD2 reaction by chelating excess Ca^{2+}.

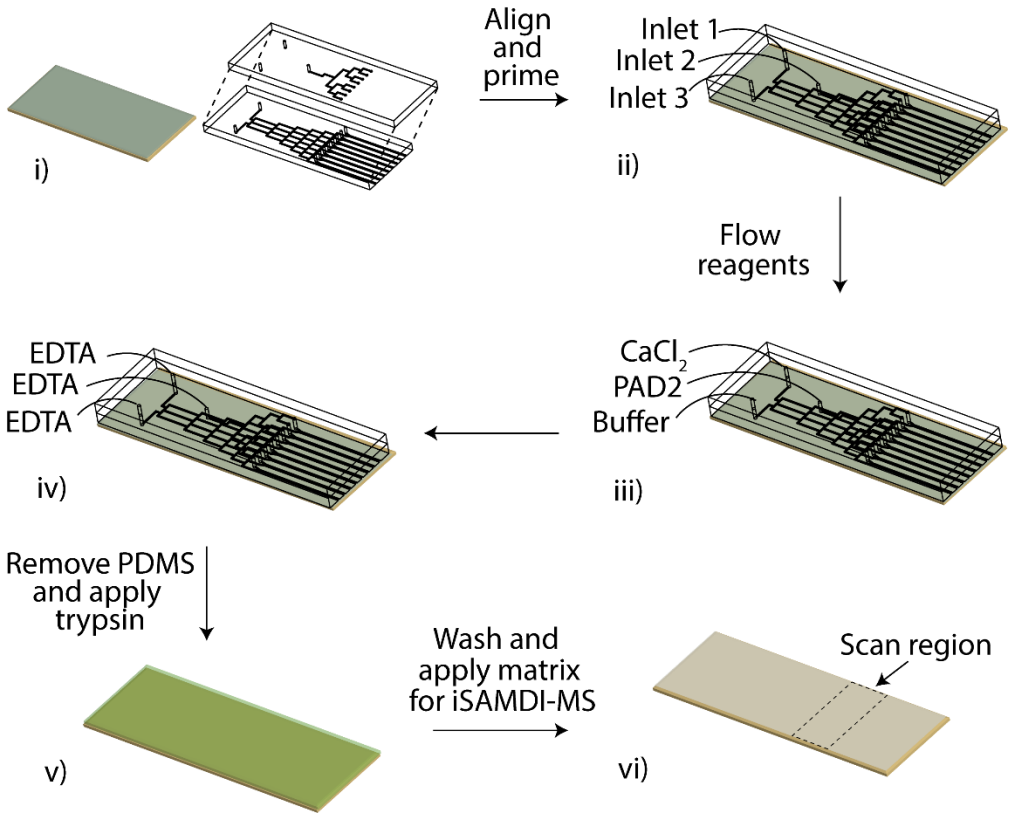

Figure 5.5 Schematic of microfluidic reactor assembly and operation. i) The bottom and top layers are aligned using the 8 through-holes in the bottom layer and placed onto the peptide-functionalized self-assembled monolayer. ii) Tubing is inserted in to all three inlets and the device is primed. iii) Solutions of CaCl2, buffer, and PAD2 are simultaneously introduced into inlets 1, 2, and 3, respectively. iv) Buffer containing EDTA is introduced into all three inlets to quench the reaction. v) The top and bottom layers are removed from the chip and the chip is rinsed. v) Matrix is applied to the chip and a region is scanned with iSAMDI-MS.

iSAMDI-MS was acquired in a 6.2 mm x 19.4 mm region of interest (ROI) on the chip with 200 µm lateral resolution. The resulting spatial map is a 31 x 97 array of pixels, where each pixel represents the yield of citrullinated product (Figure 5.6A). In the absence of Ca^{2+}, no PAD2 activity is observed. Longer reaction times (i.e. greater distances from the Y-junction) and higher Ca^{2+} concentrations yield more citrullinated product, indicating a higher fraction of activated

PAD2. No citrullination was observed in between the channels, indicating that trypsin uniformly cleaves the unmodified peptide. Notably, we observe that PAD2 citrullination favors the bottom edge of the channel immediately after the Y-junction. This is because the diffusion coefficients of Ca^{2+} and PAD2 are on the order of 10^{-5} cm^2 sec^{-1}[136] and 10^{-7} cm^2 sec^{-1},[137] respectively, and Ca^{2+} diffuses across the fluidic channel significantly faster than PAD2.

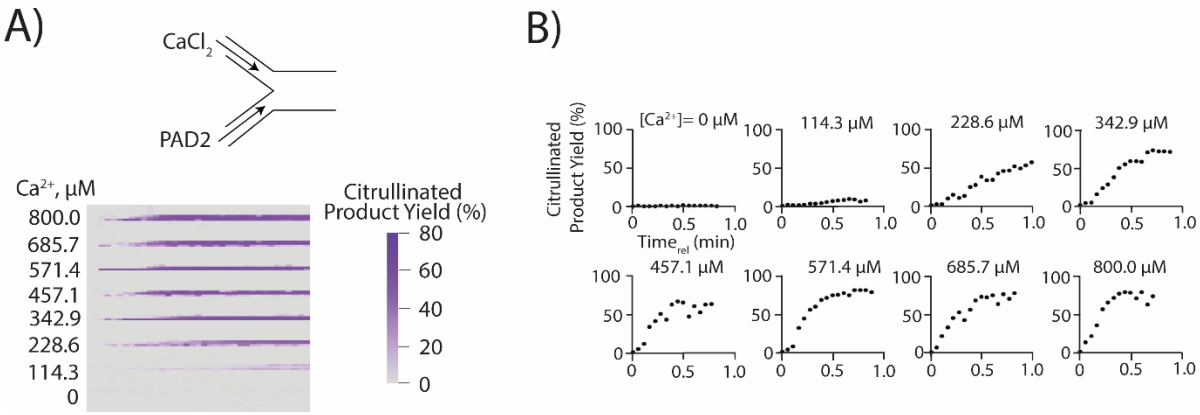

Figure 5.6 iSAMDI-MS output. A) Spatial map of PAD2 citrullination at each x,y- coordinate (31 x 97 pixel array). B) Representative initial velocity curves from each channel. The data is plotted as a function of relative time, or $time_{rel}$, due to dispersion.

Three pixels comprise the width of each channel, and the average product yield along the channel length was fitted to the Hill equation to obtain *n* and $K_{0.5}$:

$$f_{Product} = \frac{[Ca^{2+}]^n}{K_{0.5} + [Ca^{2+}]^n} \qquad (5.2)$$

where $f_{Product}$ is the citrullinated product yield (%) and $[Ca^{2+}]$ is the concentration of calcium (Figure 5.7). The experiment was repeated three independent times to obtain $n = 5.4 \pm 0.9$ and $K_{0.5} = 244 \pm 100$ µM . Our results are consistent with those by Thompson and coworkers, which report a crystal structure of PAD2 with 6 Ca^{2+} binding sites with $n>1$ and $K_{0.5} = 180 \pm 20$ µM.[118] Similar binding kinetics were observed in PAD4, showing convergence within the PAD enzyme family.[138]

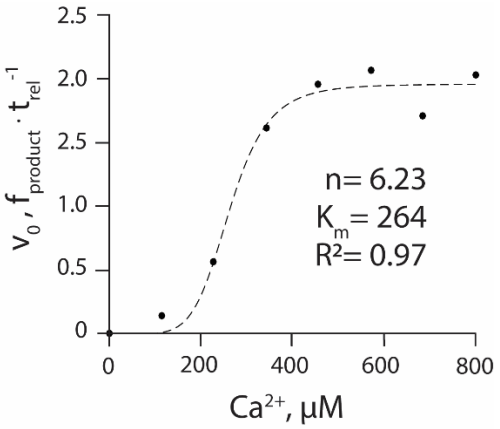

Figure 5.7 Hill plot from one experimental replicate (*n*= 6.2, $K_{0.5}$= 264 µM, R^2= 0.97). V_0 is plotted as the percent of citrullinated product over relative time (min).

PAD2 citrullination occurs very fast with k_{cat} values of 1.4 s^{-1} and 0.72 s^{-1} on peptides consisting of histone H4 residues 4-15 and 4-21, respectively.[139] The fluid flow rate and iSAMDI-MS pixel resolution allowed us to calculated the initial velocity before the reaction reached saturation. Faster reactions are easily attainable by increasing the flow rate or decreasing the pixel resolution. In this work, 93 data points were collected in each channel with a 200 µm pixel resolution. The number of pixels can be greatly increased by using commercial MALDI mass spectrometers capable of imaging at 10 µm pixel resolution (rapifleX MALDI Tissuetyper, Bruker Daltonics).

5.3 Discussion

Here we present a high-throughput strategy to characterize the degree of cooperativity and $K_{0.5}$ of an enzyme–ligand binding interaction through use of iSAMDI-MS. A 3D microfluidic device with just 3 inputs conducted all of the necessary experiments to characterize the Hill kinetics of Ca^{2+}-PAD2 binding, while requiring minimal reagent and bench time. A key feature

that distinguishes this method is that the extent of ligand binding is a function of the enzyme activity, because ligand affinities or conformational changes fundamentally do not provide a readout of the resulting enzymatic activity and may overlook the contribution of ligand binding to enzyme activation. In addition, we introduce a high-throughput assay that measures PAD2 activity without the use of secondary reporters or fluorescent labels. We envision that this methodology will have great use in high-throughput screening applications and will be extended towards other methods of activation in biology such as proteolysis,[140] protein-protein binding,[141] and prodrug activation.[142]

5.4 Experimental

Self-assembled monolayer preparation. Standard glass microscope slides were cleaned using ethanol and water in a sonication bath. An electron beam evaporator (Thermionics VE-100) was used to deposit 5 nm Ti (0.02 nm s^{-1}) followed by 30 nm Au (0.05 nm s^{-1}) at a pressure between 1 x 10^{-6} and 8 x 10^{-6} Torr. The slides were soaked overnight at 25 °C in an ethanolic solution (0.5 mM total disulfide concentration). The solution had a 1:4 ratio of an asymmetric disulfide terminated with a maleimide group and tri(ethylene glycol) group, to a symmetric disulfide terminated with tri(ethylene glycol) groups. The slides were then rinsed with ethanol and water.

PAD2 expression and purification. A pET-16b vector encoding for PAD2 was obtained from Thermo Fisher Scientific- GeneArt with the codons optimized for *E. coli* expression. The vector was transformed into BL21DE3pLysS *E. coli* using chemical transformation methods. 2xYT media (5 mL) with carbenicillin and chloramphenicol was seeded with PAD2

BL21DE3pLysS *E. Coli* and allowed to grow overnight at 30 °C while shaking at 240 rpm. The next morning, the culture was added to 2xYT media (500 mL) supplemented with carbenicillin and chloramphenicol, and grown at 30 °C while shaking until the OD_{600} reached ~0.45. The culture was cooled at 4 °C and PAD2 expression was induced with 0.5 mM IPTG overnight under shaking at 25 °C. The bacteria were pelleted by centrifugation and lysed in buffer (50 mM sodium phosphate (7.5), 500 mM NaCl, 0.5 mM EDTA, 10 % glycerol (v/v), 0.1% Triton X-100, 50 mL) containing Bug Buster (10x, 2 mL) and one cOmplete-Mini protease inhibitor tablet. The overexpressed PAD2 contained an N'-terminal His tag and was purified on a nickel immobilized metal affinity chromatography (IMAC) column. Fractions were eluted off of the nickel column with a gradient of 5-500 mM imidazole in 50 mM sodium phosphate (7.5), 500 mM NaCl, 0.5 mM EDTA, 10 % glycerol (v/v), 0.1% Triton X-100. The eluted fractions were combined and concentrated to 1 mL in a 25 mL Amicon 30 kDa cutoff Centrifugal Filter Unit (Millipore). The PAD2 was further purified using size exclusion chromatography on an Akta FPLC (GE Healthcare) using running buffer (50 mM sodium phosphate (7.5), 500 mM NaCl). Fractions containing PAD2 were confirmed by SDS-PAGE, pooled and concentrated, and stored at 80 °C in 50% glycerol (Figure 5.8).

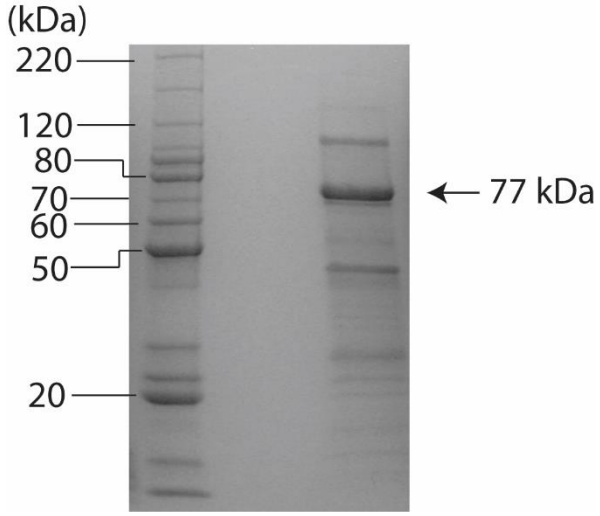

Figure 5.8 SDS-PAGE of PAD2 expressed and purified from *E. Coli*.

Microfluidic device fabrication. PDMS masters were rendered on SolidWorks software (Figure 5.9). The master for the top layer had one 800 µm inlet branching into eight 250 µm width and 250 µm height channels. The master for the top layer had two 800 µm inlets that split and merged into eight 250 µm width and 250 µm height channels. 800 µm width and 3 mm tall posts connected the bottom layer to the top layer, and the channels expanded to a width of 550 µm and height of 550 µm after this intersection. The files were converted to .stl format and printed in digital printing mode using a Stratasys Connex 350 3D printer in VeroWhite material (Stratasys Direct) with a glossy finish. The 3D printed masters were prepared for PDMS polymerization as previously described.[44] PDMS prepolymer mixture was mixed in a 1:10 ratio (w/w curing agent to prepolymer), degassed in a vacuum desiccator for 15 min, and poured into the 3D printed master. The master containing PDMS was degassed in a vacuum desiccator for 15 min and placed in a 43 °C oven overnight. The PDMS blocks were then peeled off of the mold

and treated in a 130 °C oven for 10 min. The 3D printed molds were reused for additional PDMS curing cycles.

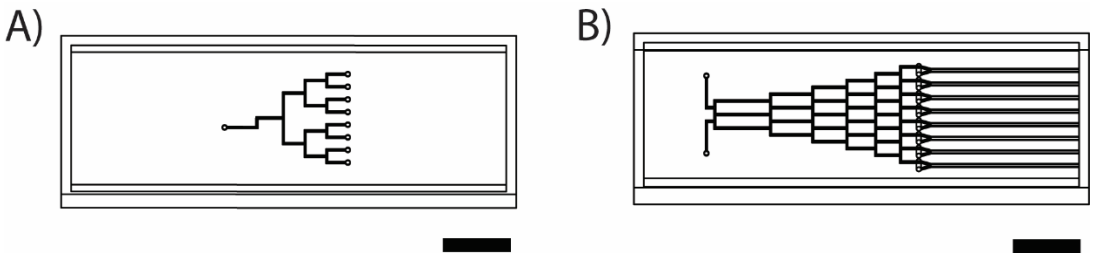

Figure 5.9 SolidWorks renderings of PDMS masters. A) top layer, B) bottom layer. Scale bar= 10 mm

A solution of Ac-GYNRGC peptide (100 µM) in 100 mM Tris (8.0), 0.01% Triton X-100 was added to a microscope slide functionalized with the self-assembled monolayer. This was allowed to incubate in a humidity chamber for 1 h at room temperature. Then, the side was rinsed with ethanol and water. The two-layer PDMS device was assembled and primed as previously described and held together with light pressure from an external clamp.[95] The priming buffer was 100 mM Tris (pH 8.0), 50 mM NaCl.

External calibration. Solutions containing different ratios of Ac-GYNRGC and Ac-GYNCitGC (100 µM total peptide) were prepared in 100 mM Tris (8.0). 2.5 µL of each peptide solution was individually spotted in separate areas of a gold-coated glass slide functionalized with the SAM. The slide was incubated in a humidity chamber for 1 h at 25 °C. The slide was rinsed with ethanol and water, and dried under a stream of N_2. A stock solution of trypsin was prepared by adding a solution of 150 µL 50 mM acetic acid and 50 uL glycerol to an ampule of lyophilized trypsin (20 µg, Sequencing Grade Modified Trypsin, Promega). This glycerol stock

was stored at -80 °C in 20 µL aliquots. A 180 µL solution of 40 mM ammonium bicarbonate, 0.01% Triton X-100 was added to a 20 µL aliquot of trypsin. This solution was then pipetted onto the entire slide and allowed to react at room temperature for 1 h at 25 °C in a humidity chamber. The slide was treated with 2',4',6'-trihydroxyacetophenone monohydrate (THAP, 25 mg mL^{-1} in acetone) and three SAMDI-MS spectra were obtained from each spot. The % citrullination was quantified using the peak intensity of the citrullinated peptide (I_{Cit}) and the peak intensity of the substrate peptide (I_R) on flexAnalysis software (Bruker Daltonics):

$$\% \text{ Citrullination} = 100 \times \frac{I_{Cit}}{I_{Cit}+I_R} \qquad (5.3)$$

Microfluidic device operation. A solution of 100 mM Tris (pH 8.0), 50 mM NaCl, 100 µM tris(2-carboxyethyl)phosphine hydrochloride (TCEP), 1.75 µM PAD2 was introduced into the top layer at 2.0 µL min^{-1}. Simultaneously, a solution of 1.6 mM $CaCl_2$, 100 µM TCEP, 100 mM Tris (pH 8.0), 50 mM NaCl was injected into one inlet of the bottom layer and 100 mM Tris (8.0), 50 mM NaCl was injected into the other inlet of the bottom layer at a flow rate of 1.0 µL min^{-1}. The device was operated for 1 h. Afterwards the inlet of the top layer was replaced with a solution of 100 mM Tris (pH 8.0), 50 mM NaCl, 3 mM ethylenediaminetetraacetic acid (EDTA) and 1 mL was manually injected. Then, the inlets leading to the bottom layer were replaced with a solution of 100 mM Tris (pH 8.0), 50 mM NaCl, 3 mM EDTA and 1 mL was manually injected into the device. The clamp was disassembled, the PDMS layers were peeled off of the chip, and the chip was rinsed with ethanol and water. 50 mM acetic acid (200 µL) was added to an ampule containing 20 µg lyophilized trypsin, and this solution was then added to 1.8 mL of 40 mM ammonium bicarbonate, 0.01% Triton X-100. The chip was placed in a humidity chamber at

room temperature for 1 h and then rinsed with ethanol, water, and acetone. Matrix (25 mg mL^{-1} THAP in acetone) was applied by tilting the slide at a 45 ° angle, pipetting matrix (80 µL) on top of the slide and letting the matrix solution fall to the base of the slide where excess matrix was absorbed by a Kim wipe.

Mass spectrometry imaging. A 31 x 97 pixel ROI was selected with FlexImaging software (Bruker Daltonics). MALDI-IMS was acquired by creating an AutoXecute method as previously described.10 Spectra were acquired with a 200 µm lateral resolution and with 125 laser shots accumulated per pixel using the 'medium' aperture setting. The laser pulse rate was 200 Hz and spectra were obtained with a mass window of 600-3000 m/z.

Image analysis and quantitation. Ion intensity maps were generated on FlexImaging software at 1050.8 ± 0.2 Da and 1584.3 ± 0.2 Da, corresponding to RGC-alkanedisulfide and Ac-GYNRGC-alkanedisulfide, respectively (Figure 5.10A). The .mis file was converted to an .imzML using FlexImaging software and imported into MSiReader v1.00. Peak intensities of 1050.8 ± 0.2 Da and 1584.3 ± 0.2 Da were exported into Excel and the % conversion was determined using equation (5.3). Three to four rows of pixels in each channel contained RGC and Ac-GYNCitGC bound to the self-assembled monolayer. The % conversion was plotted in a heatmap (MATLAB R2016a). The flow velocity was determined using Q=Av, where Q is the volumetric flow rate and A is the cross-sectional area of the channel. The amount of time required for the fluid to flow downstream across each 200 µm pixel was calculated and plotted against the % conversion. Linear regression was used to determine the slope of each plot, and the

three replicates from each channel were averaged to obtain V_0. The initial velocities were plotted as a function of Ca^{2+} concentration and fitted to the Hill equation (Enzyme Kinetics Module, SigmaPlot 12.0, Systat Software). This was repeated two more times to obtain three experimental replicates. The reported $K_{0.5}$ and n values were obtained from averaging the $K_{0.5}$ and n values obtained from each experimental replicate.

Verification of $CaCl_2$-induced PAD2 activation. I verified that the increase in PAD2 activity at the base of the Y-junction is due to activation by Ca^{2+}. A solution of 1.6 mM $CaCl_2$, 1.75 µM PAD2, and 200 µM TCEP in buffer (100 mM Tris pH 8.0, 50 mM NaCl) was injected into the top inlet at 2.0 µL min^{-1}. Simultaneously, buffer (100 mM Tris pH 8.0, 50 mM NaCl) was introduced into each inlet of the bottom layer at 1.0 µL min^{-1}. The device was operated and analyzed by iSAMDI-MS as previously described. The FlexImaging software output shows that citrullination immediately begins at the intersection between the top and bottom layers and continues along the channel length (Figure 5.10B). This is in contrast the to the experimental replicates that have a gradient of Ca^{2+} in the bottom layer, where PAD2 activity starts at the base of the Y-junction after diffusively mixing with the Ca^{2+} stream.

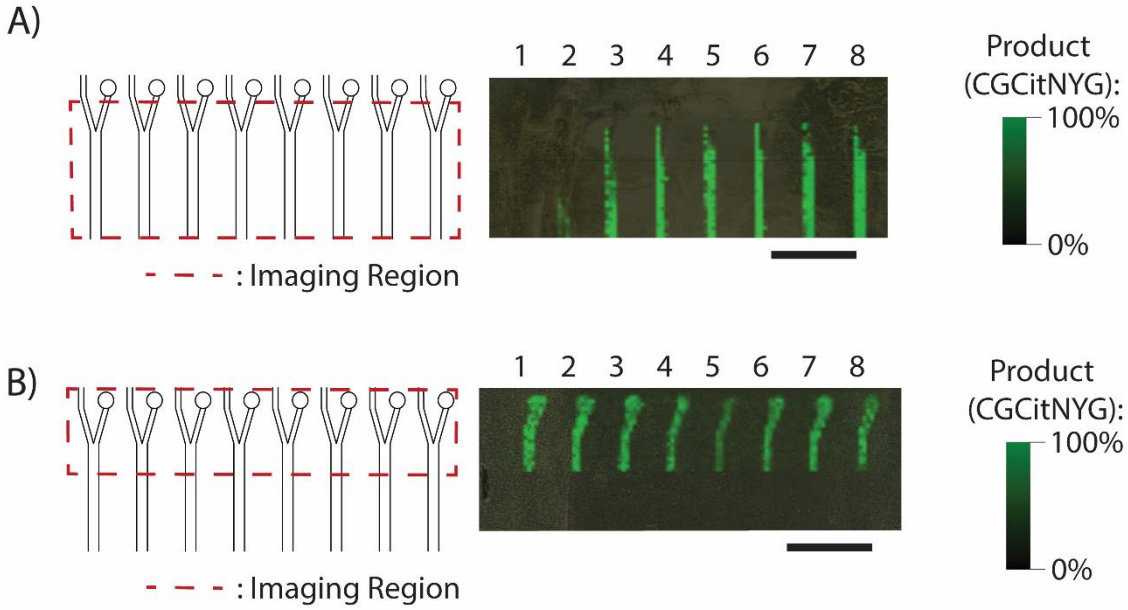

Figure 5.10 Control ion maps of citrullinated peptide detected with iSAMDI-MS. A) Ion map of the citrullinated product-maleimide alkanedisulfide conjugate (*m/z* 1584.1 ± 0.2) visualized in green. Scale bar= 5 mm. B) Ion map from a control study where PAD2 is pre-mixed with $CaCl_2$ and injected into the top inlet. The citrullinated product-maleimide alkanedisulfide conjugate (*m/z* 1584.1 ± 0.2) is visualized in green. Scale bar= 5 mm.

Peptide library construction and analysis. The Ac-GXZRGC peptide library was synthesized using standard solid-phase peptide synthesis on SynPhase polymamide lanterns with Fmoc-Rink amide linkers purchased from Mimotopes. Fmoc- and side chain-protected amino acids and N-acetyl-glycine were purchased from Anaspec or Sigma-Aldrich. Pybop, N-methyl morpholine, and dimethyl formamide were purchased from Fisher or Sigma-Aldrich. 96-well filter plates purchased from Arctic White and a 96-well plate vacuum manifold from Millipore were used for synthesis. Lanterns were swelled in dimethylformamide (DMF) for 1 hour, drained, and then separated into individual wells in four 96-well filter plates. The linkers on the lanterns were Fmoc-deprotected with a solution of 20% piperidine in DMF for 20 minutes. The lanterns were drained and rinsed with DMF using vacuum filtration. Cysteine was then coupled

to each lantern for 20 minutes using Fmoc-Cys(Trt)-OH, Pybop and N-methyl morpholine (NMM) in 250 µL DMF at a molar excess of 8:8:16, respectively to the loading capacity of the lanterns. The lanterns were then drained and rinsed with DMF using vacuum filtration. Fmoc-deprotection, rinsing, and coupling reactions were repeated until the last amino acid (N-acetyl-glycine) was coupled. Following the last coupling reaction, the lanterns were rinsed with DMF and dichloromethane, then dried under vacuum for 1 hour. The lanterns were transferred into new 96-well plates, and treated for 2 hours with a solution of 95% trifluoroacetic acid (TFA), 2.5% triethylsilane, and 2.5% H_2O to allow for amino acid side chain deprotection and peptide cleavage from the lanterns. The lanterns were discarded and the TFA was evaporated under nitrogen. The peptides were resuspended in 0.1% TFA in H2O and lyophilized. The peptides were then resuspended again in 0.1% TFA in H2O to a final concentration of 500 µM. Peptides were verified using MALDI mass spectrometry.

To prepare the peptide arrays, steel plates were washed in hexanes and then ethanol and rinsed with water and then ethanol. Using a Thermionics E-beam evaporator and masks with 384 spots, 50 angstroms of titanium was evaporated onto the steel plates. Following titanium evaporation, 300 angstroms of gold was evaporated over the titanium. The 384 gold spotted plates were soaked for 48 hours at 4 ºC in a 1 mM total disulfide monolayer solution of 0.8 mM tri(ethylene glycol) disulfide and 0.2 mM tri(ethylene glycol)-maleimide disulfide in ethanol. The monolayer self-assembles onto the gold spots presenting a functional maleimide group at a density of 10% with an tri(ethylene glycol) background.

The peptide library was neutralized by dilution in 50 mM Tris pH 7.5 to a concentration of 50 µM. The peptides were pipetted onto the 384 spotted gold plates and incubated in a

humidity chamber at room temperature for 1 hour to allow for immobilization through 1,4-Michael addition of the thiol side chain of cysteine to the maleimide on the surface. The arrays were washed with water and then ethanol and dried under nitrogen.

Peptide library assays. The trypin assay was conducted by dissolving an ampule of lyophilized trypsin (20 µg) in 200 µL 50 mM acetic acid. This was added to 1.8 mL 40 mM ammonium bicarbonate. A liquid handling robot (Thermo Scientific Multidrop Combi) dispensed 2.5 µL of this trypsin solution onto each spot on the peptide library array plate. The plate was placed in a humidity chamber at room temperature for 1 h. Then, the plate was rinsed with ethanol and water. The PAD2 assay was conducted by dispensing a solution of 875 nM PAD2, 10 mM $CaCl_2$, 100 mM Tris (8.0), 50 mM NaCl onto the peptide library array plate using a liquid handling robot. The robot dispensed 2.5 µL of PAD2 solution onto each spot. The plate was incubated at room temperature in a humidity chamber for 30 min, then rinsed with ethanol and water. Then, the trypsin assay was conducted on the plate as previously described. The peptide array plates were treated with a matrix solution (10 mg/mL THAP in acetonitrile with 0.1% TFA)

Analysis was conducted on an AbSciex 5800 MALDI TOF/TOF mass spectrometer in batch mode with 600 shots accumulated per spot with continuous stage motion. The area under the curve (AUC) for peaks representing the intact peptide-alkanedisulfide conjugates and the trypsinized peptide-alkanedisulfide conjugates were extracted using Profiler software. The citrullinated product yield (%) was calculated using the following equation:

$$\text{Citrullinated product yield (\%)} = \frac{AUC_{Cit}}{AUC_{Cit}+AUC_{Tryp}} \times 100 \qquad (5.4)$$

where AUC_{Cit} represents the citrullinated peptide-alkanedisulfide conjugate and AUC_{Tryp} represents the trypsinized peptide-alkanedisulfide conjugate. The trypsinized product yield was calculated using the following equation:

$$\text{Trypsinized product yield (\%)} = \frac{AUC_{Tryp}}{AUC_{Tryp}+AUC_{Intact}} \times 100 \qquad (5.5)$$

where AUC_{Intact} represents the intact peptide-alkanedisulfide conjugate and plotted in Figure 5.11.

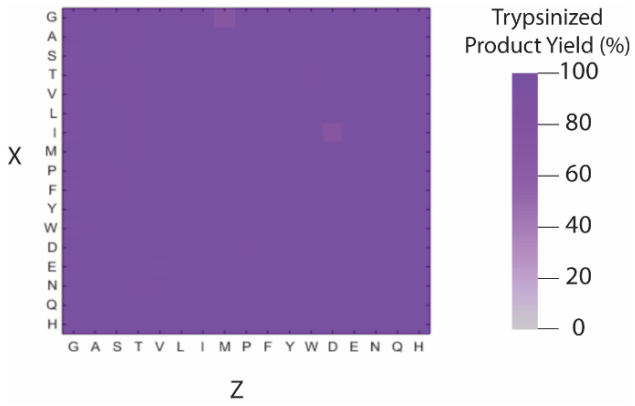

Figure 5.11 Heat map of trypsin activity without PAD2 treatment. Mean, n=2.

Chapter 6

An Immobilized Enzyme Reactor for Spatiotemporal Control over Reaction Products

This chapter is adapted from the following published work:
Grant, J.; Modia, J.; Roll, J.; Perkovich, P.; Mrksich, M. *"An Immobilized Enzyme Reactor for Spatiotemporal Control over Reaction Products"* Small 2018, doi: 10.1002/smll.201800923.

6.1 Introduction

Enzymes are responsible for almost every metabolic transformation in the living cell. Therefore, enzyme networks must perform robustly despite competing reactions, flux imbalances, and accumulation of toxic intermediates. To overcome these challenges, cells often organize metabolic reactions spatially and temporally using membrane-bound enzymes and highly ordered enzyme complexes. In this manner, metabolic processes involving multiple enzymatic transformations efficiently channel metabolites between active sites to effectively control the reaction products and their rates of formation. One characteristic of a spatiotemporally organized reaction network is that the same set of enzymes can generate unique reaction products depending on the order of enzyme-mediated reactions. A notable example of such organization is observed in the synthesis of highly branched and complex oligosaccharides in the Golgi apparatus, where an ordered array of membrane proteins sequentially adds or removes glycans on a protein substrate. In this way, an exponential number of glycoforms can be produced simply by rearranging the order of modification as the substrate moves between the *cis* and *trans* cisternae.[143,144] This spatiotemporal, modular design can produce a variety of metabolically useful compounds from a small subset of enzymes without diverting resources towards producing, or possibly evolving, a new enzyme for catalyzing each desired reaction

product. The strategies that cells use to organize metabolic and signaling cascades has inspired efforts in the laboratory to develop compartmentalized and spatiotemporally-controlled systems capable of performing multi-step enzyme cascades.[145–147]

Compartmentalization provides many advantages over traditional batch processes because multiple reaction steps can be individually interrogated and optimized.[148] Recent work has demonstrated strategies to sequentially organize two or more enzymes on solid supports for performing multistep transformations. For example, packed-bed reactors have been used to arrange enzymes in series using streptavidin, Ni-NTA, and anti-FLAG coated beads.[149–152] Microfluidic devices integrated with valves or magnetic components have organized enzyme-coated beads in well-defined regions on a chip,[152–154] which is beneficial for reducing dead volume.[153] An important feature of multi-enzyme cascade systems is the ability to precisely control the order of each reaction. To demonstrate the importance of maintaining correct enzyme order in a reaction sequence, three recent studies observed a significant increase in product yield when two enzymes were correctly ordered along a fluidic stream and negligible yield when the enzymes were arranged out of order.[155–157] Of particular interest are methods that use site-selective immobilization to co-localize multiple enzymes on the same chip for circumventing the need to separate each reaction in different compartments, as demonstrated by Niemeyer and coworkers using DNA hybridization.[155] These examples illustrate the immense value in spatially organizing enzymes for increasing the yields of products in tandem reactions; however, this important work did not investigate how microfluidic chips with identical compositions can provide different mixtures of reaction products dependent on the order of modification.

In this chapter, we describe a microfluidic reactor having two enzymes organized such that a substrate in the flow stream will encounter the enzymes sequentially. The two enzymes, peptidylarginine deiminase type 1 (PAD) and acetyltransferase p300/CBP associated factor (PCAF) catalyze citrullination and acetylation, respectively, on a histone H3-derived peptide substrate (Ac-TARK^{Ac}STGGKAPC). These two enzymes were of particular interest because treatment of the substrate with the two enzymes gives different products depending on the enzyme order.[158] This temporal dependence is due to a "crosstalk" wherein PCAF is unable to acetylate a peptide that is first citrullinated, though the acetylation state has no effect on PAD-mediated citrullination of the peptide (Figure 6.1). By spatially organizing PAD and PCAF along the fluidic chip we can tailor the device in favor of citrullinated or acetylated H3 peptide production.

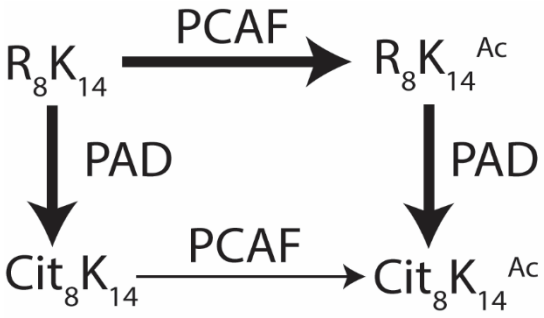

Figure 6.1. Schematic of crosstalk between Arg8 citrullination and Lys14 acetylation on the H3 peptide substrate. PCAF modifies K_{14} at a high rate if R_8 is un-citrullinated. However, PCAF modifies K_{14} at a much slower rate if R_8 is citrullinated.

6.2 Results

Design of the spatiotemporal fluidic system. Our approach is based on a microfluidic chip that has one enzyme covalently patterned on the chip surface for a defined length and the second

enzyme patterned in a downstream region of the channel for a defined length (Figure 6.2). In this way, a substrate introduced into the device will initially encounter the first enzyme which converts it to an intermediate—where the time for this first reaction depends on the flow rate and length of channel having the immobilized enzyme—and which then encounters the second enzyme that converts the intermediate to the final product. Finally, the surface of the chip downstream of the second enzyme presents a thiol-reactive maleimide group that serves to capture the cysteine-containing substrate and products. Self-assembled monolayers for matrix laser desorption/ionization mass spectrometry (SAMDI-MS) offers the significant advantage of detecting and quantifying all reaction species−substrate, intermediate, and product−directly on the reactor chip. This ability to and quantitate all reaction products on the chip avoids the need to isolate and analyze each product.

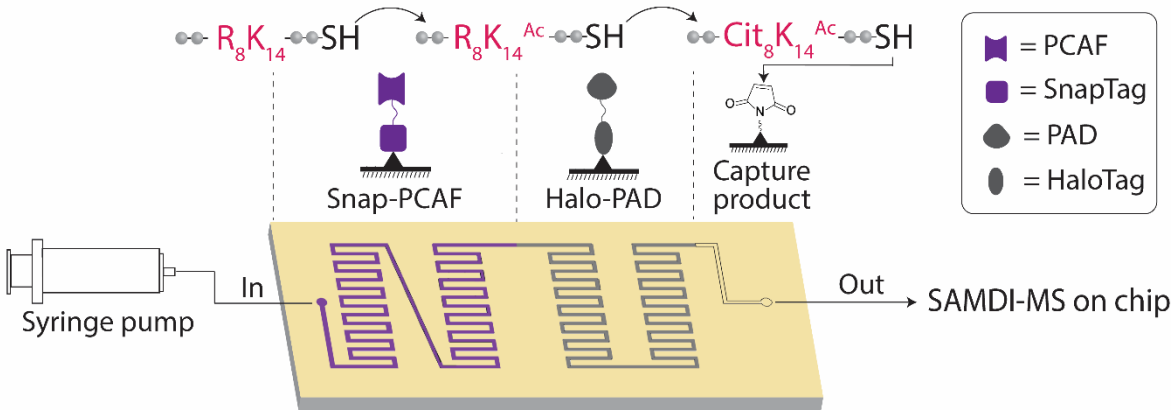

Figure 6.2 Overview of the reactor chip assembly and operation. A unidirectional microfluidic channel with an inlet and an outlet is placed onto a gold-coated microscope slide functionalized with a self-assembled monolayer. The chip has two enzymes, Snap-PCAF and Halo-PAD, patterned in discrete regions along the fluidic channel. A H3 peptide substrate flows through the chip—where it first encounters Snap-PCAF—and becomes acetylated. The acetylated product of the first reaction is the substrate for the next enzyme reaction by Halo-PAD, which citrullinates the peptide. A thiol on one end of the peptide covalently binds to maleimide functional groups in a downstream capture region. The products are analyzed by SAMDI-MS.

The chip is a glass slide modified with a self-assembled monolayer of alkanethiolates on gold presenting maleimide groups at a density of 5% against a tri(ethylene glycol) background. The latter prevents both nonspecific protein adsorption and immobilized protein denaturation,[159,160] and is important for ensuring a consistent enzyme density and maintaining the activity of the enzymes. The Mrksich group previously reported a protein immobilization method wherein fusion proteins are covalently attached to a self-assembled monolayer using chemically orthogonal irreversible ligands.[161,162] For this work we immobilized PAD and PCAF to different regions in the channel using two enzyme-substrate pairs (Figure 6.3).

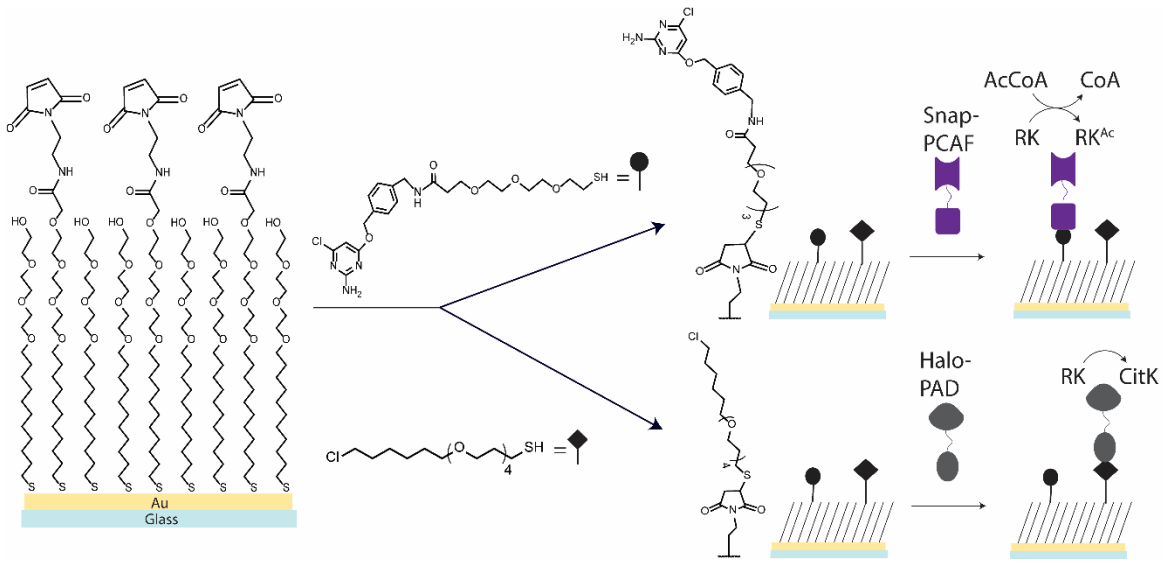

Figure 6.3 Strategy for PCAF and PAD immobilization. A self-assembled monolayer displaying maleimide is functionalized with SnapTag capture ligand (top) or HaloTag capture ligand (bottom) through reaction of the thiol. PCAF and PAD were prepared as SnapTag and HaloTag fusion proteins, respectively. The SnapTag domain is covalently captured via a 2,6-dichloropyramidine substrate and the HaloTag domain is captured via a hexylchloride to present PAD and PCAF on the surface of the self-assembled monolayer.

The first enzyme is SnapTag, an engineered O6-alkylguanine alkyltransferase that site-specifically reacts with benzylguanine and benzylchloropyrimidine derivatives via a nucleophilic cysteine.[163–165] The second enzyme is HaloTag, an engineered haloalkane dehalogenase that covalently reacts with primary alkylchlorides via a nucleophilic aspartate.[166] The HaloTag and SnapTag proteins react with capture ligands based on an alkylchloride and benzylchloropyrimidine derivative, respectively, on the monolayer. We prepared the capture ligands with a free thiol to allow their immobilization to monolayers presenting the maleimide groups (Figure 6.4).

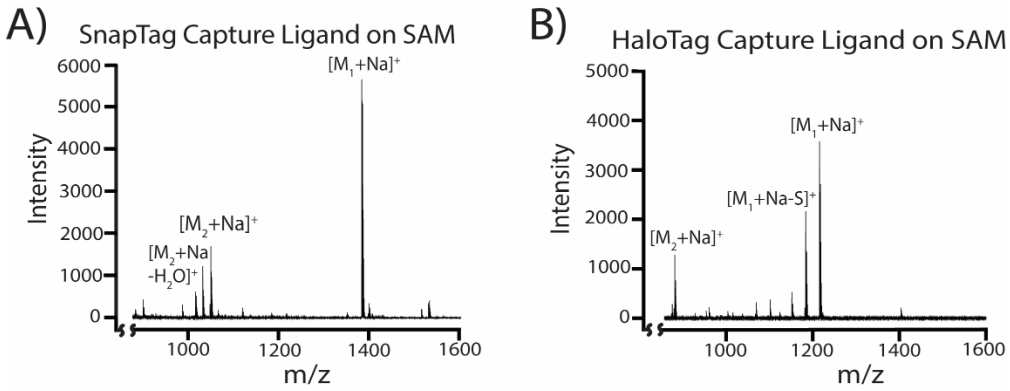

Figure 6.4 SnapTag and HaloTag immobilization on the SAM. A) A SAMDI spectrum of the monolayer functionalized with SnapTag capture ligand has a peak at *m/z* 1357.4 corresponding to the ligand-alkanedisulfide conjugate and peaks at *m/z* 1023.2, 1005.2 corresponding to ligand-alkanethiol conjugates. B) A SAMDI spectrum of the monolayer functionalized with HaloTag capture ligand has a peaks at *m/z* 1215.4, 1183.4 corresponding to ligand-alkanedisulfide conjugates and a peak at *m/z* 881.3 corresponding to the ligand-alkanethiol conjugate.

We generated the HaloTag fusion protein from an expression construct based on the commercially available pET-16b vector, where HaloTag is N-terminally fused to PAD with an $(EAAAK)_4$ peptide linker. Similarly, we generated the SnapTag fusion protein as an N-terminal fusion to PCAF, separated by the standard $(EAAAK)_4$ helical linker. Hence, these fusion

proteins—HaloTag-PAD (Halo-PAD) and SnapTag-PCAF (Snap-PCAF)—each have the enzyme domain that will be active in the channel and a capture domain that is used to immobilize them on the chip. We expressed the Halo-PAD construct in the BL21(DE3)pLysS *E. coli* strain and the Snap-PCAF construct in the BL21(DE3) *E. coli* strain. We expressed both fusion constructs using standard induction with isopropyl β-D-1-thiogalactopyranoside (IPTG) and purified expressed proteins using an included His-tag for nickel column affinity chromatography, followed by size exclusion chromatography. The resulting Halo-PAD and Snap-PCAF fusion proteins are 112.1 kDa and 43.7 kDa, respectively (Figure 6.5).

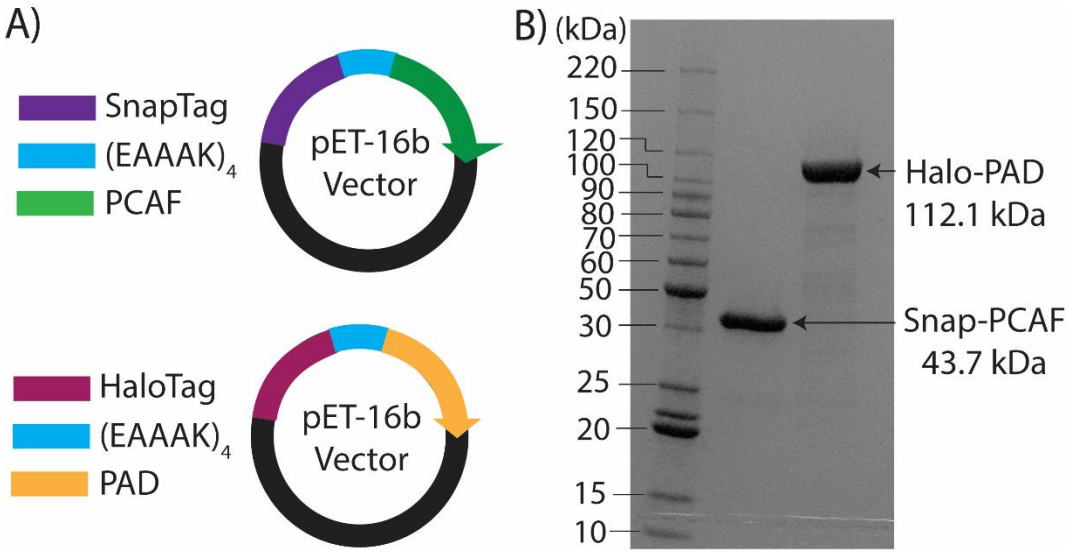

Figure 6.5 Expression and purification of fusion proteins. A) Expression of Snap-PCAF (top) and Halo-PAD (bottom). Snap-PCAF and Halo-PAD fusion proteins were constructed in pET-16b plasmids. The PCAF and PAD plasmids were introduced into Bl21(DE3) *E. coli* and BL21(DE3)pLysS *E. coli*, respectively, for protein expression. B) SDS-PAGE of purified Halo-PAD and Snap-PCAF.

We fabricated the microfluidic element—which is subsequently brought into contact with the self-assembled monolayer—from PDMS. We used 3D printed molds instead of commonly-

used photolithographically patterned masters because 3D printing allowed me to rapidly prototype different designs without requiring use of a cleanroom and the ability to build and test many mold replicates in a short period of time. (Figure 6.6). 3D printed molds have been previously fabricated using PDMS for microfluidic applications and post-treatment methods using combinations of heat, oxygen plasma, or silanization have been reported to improve PDMS polymerization on the 3D printed mold.[167,168] Here, we simply heat-treated PolyJet 3D printed molds and then poured the PDMS prepolymer mixture directly into the mold. Our molds were printed using a Stratasys Connex 350 3D printer with VeroWhite material and the molds did not require any modification other than a simple heat treatment step to support PDMS polymerization and rapid removal.

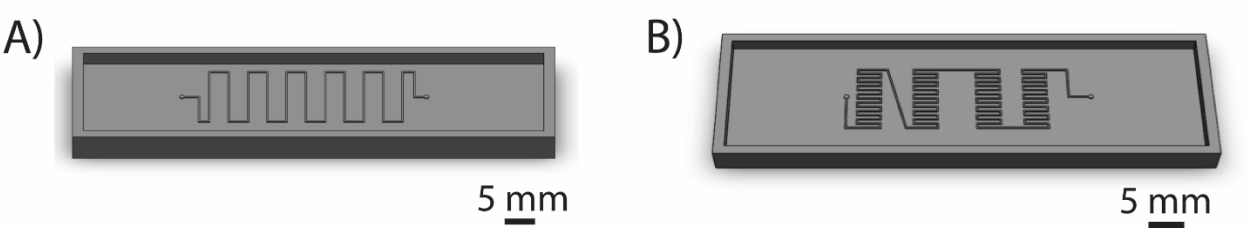

Figure 6.6 SolidWorks renderings of PDMS masters. A) SolidWorks rendering of the 3D printed mold for fabricating PDMS replicates used for individual PAD and PCAF activity studies. B) SolidWorks rendering of the 'NU' 3D printed mold used for tandem enzyme reaction studies.

Single enzyme reactions with immobilized PCAF. We first investigated each of the enzyme-mediated reactions on its own, beginning with acetylation of the H3 peptide in a chip having immobilized Snap-PCAF followed by a downstream region presenting the maleimide group for effluent capture (Figure 6.7A).

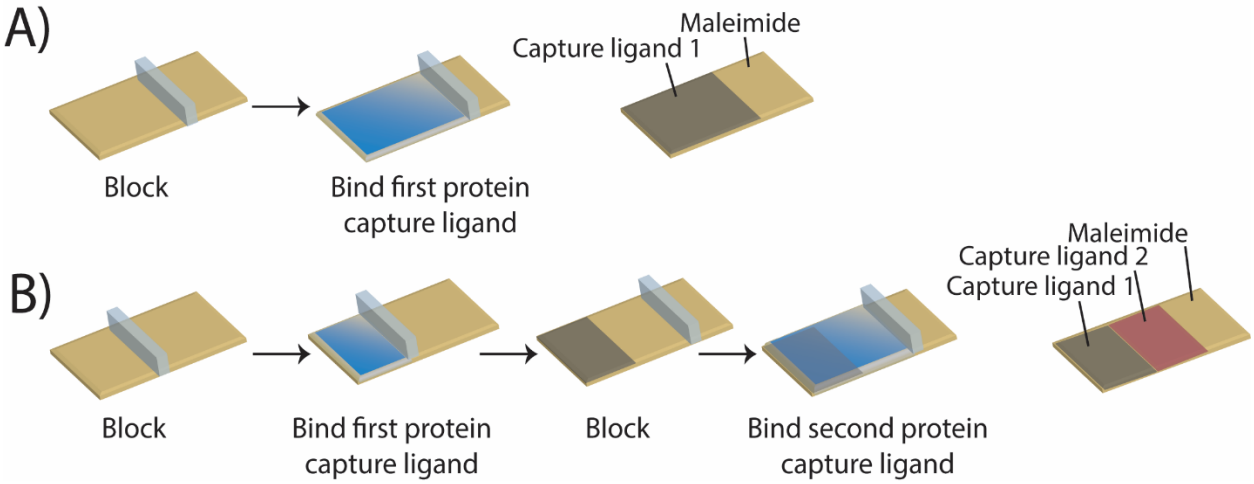

Figure 6.7 Procedure for patterning capture ligands. A) A PDMS block is placed onto a gold coated glass slide functionalized with the maleimide self-assembled monolayer. A solution of capture ligand is pipetted onto the side of the PDMS block where immobilized enzyme is desired. Rinsing the capture ligand solution leaves an area of the chip patterned with capture ligand. B) To immobilize a second capture ligand, the PDMS block is moved to an adjacent, unfunctionalized area of the chip and the binding process is repeated. The second capture ligand can be incubated on top of the first capture ligand because all of the maleimide sites are already occupied by the first capture ligand.

We first patterned the SnapTag capture ligand on a stripe of the monolayer by reacting the ligand on the maleimide monolayer for 1 h. Figure 6.8 shows a schematic of the procedure for operating the device once the capture ligand has been patterned. We aligned the PDMS block with microchannel features on the self-assembled monolayer, ensuring that the SnapTag capture ligand was located upstream of the effluent capture region. We inserted tubing into the inlet and outlet with the inlet connected to a pressure-driven syringe pump. We primed the device with Tris HCl (pH 8.5) buffer containing Triton X-100, then injected a solution of Tris HCl (pH 8.5) buffer containing Snap-PCAF and Triton X-100 to immobilize the enzyme. The Triton X-100 was added to further ensure nonspecific protein adsorption to the chip and channel walls. We

next washed any remaining Snap-PCAF out of the device using Tris HCl (pH 8.0) buffer. Lastly, we removed the outlet tubing, dried the tubing with nitrogen, and inserted it back into the device.

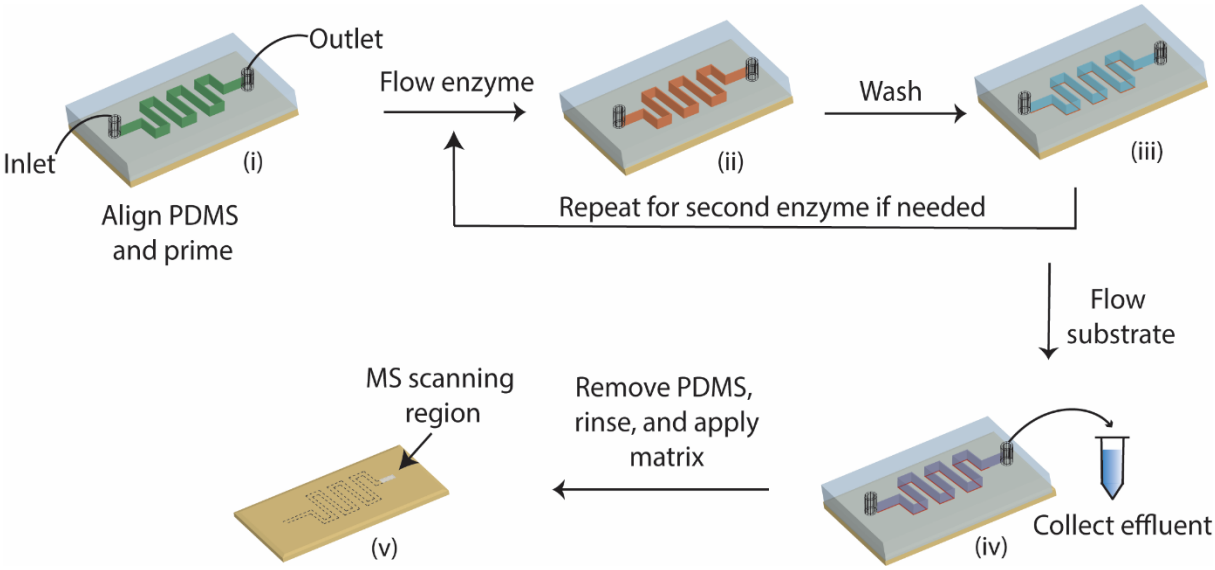

Figure 6.8 Procedure for fabricating and operating the fluidic reactor on the self-assembled monolayer. A PDMS block with microchannel features is placed on the chip prepared in Figure 6.7 with tubing inserted into the inlet and outlet. The outlet is located on the side of the chip that is free of capture ligand. (i) The channel is primed with buffer and (ii) the enzyme is flowed through the chip. (iii) A wash step removes non-immobilized enzyme and steps ii-iii are repeated if a second enzyme will be immobilized on the chip. (iv) A solution of peptide substrate and cofactors are introduced at the inlet and the effluent is collected. (v) The PDMS block is peeled from the chip and the effluent capture region is analyzed by SAMDI-MS.

To verify the acetyltransferase activity of Snap-PCAF, we flowed the H3 peptide substrate at a flow rate ranging between 0.1 and 0.4 µL min^{-1}. After flowing for 1.5 reactor volumes, we collected the effluent (for subsequent analysis) and the PDMS slab was peeled off of the chip. The chip presenting the self-assembled monolayer was rinsed with ethanol and water and treated with 2,4,6-tri-hydroxyacetophenone (THAP) matrix in acetone to be subsequently analyzed by SAMDI-MS. We noticed that the matrix crystallized more densely on the region of

the reactor chip exposed to the channel, which enabled us to easily locate the captured reaction species using the video camera in the MALDI-MS instrument.

Performing SAMDI-MS on the reactor chip produced spectra with mass-to-charge values corresponding to the H3 peptide bound to the maleimide-terminated alkanethiolate (and the corresponding disulfide) (Figure 6.9A).

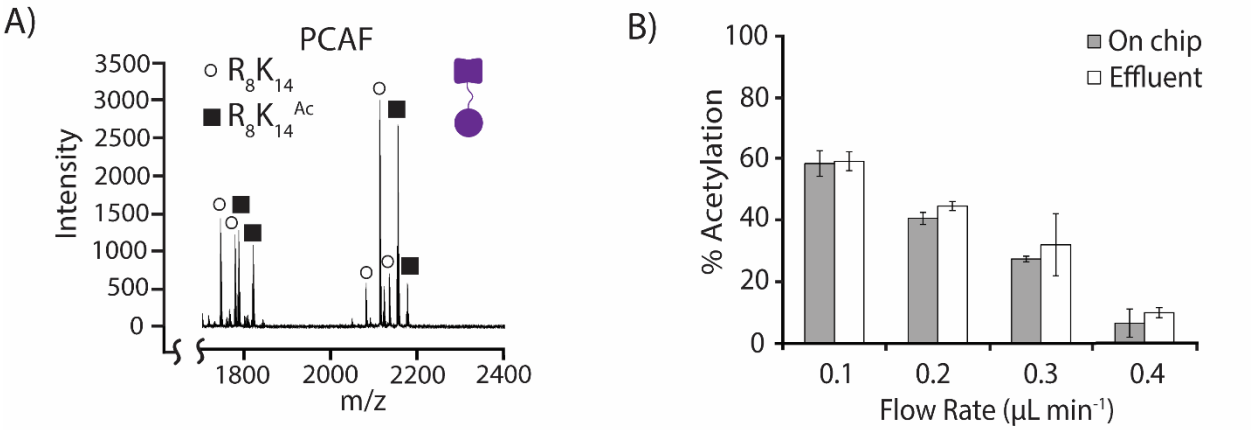

Figure 6.9 PCAF activity in the device. a) A SAMDI-MS spectrum of the collected effluent from the PCAF reactor. Acetylation increases the substrate mass by 42 Da. The proton, sodium, and potassium monoisotopic substrate (circles) and product peaks (squares) were integrated to calculate the percent of acetylated product. b) The yield of the acetylated product was calculated from the reactor chip and collected effluent at different flow rates. Mean ± SD (n=3).

Acetylation by PCAF corresponds to an increase in molecular weight of 42 Da. We studied the effect of flow rate on PCAF acetylation by assembling reactors where substrate was flowed at 0.1, 0.2, 0.3, and 0.4 µL min^{-1} (Figure 6.9B). It is significant that the geometry of our channel— where the height is 250 µm— together with these flow rates ensure efficient mixing of substrates throughout the channel. We calculated the product yield from Equation 6.1 using the integrated area under the peaks (AUC) for the substrate and product:

$$\% \text{ product} = \frac{AUC_{product}}{AUC_{product}+AUC_{substrate}} \times 100 \qquad (6.1)$$

These data reveal that PCAF acetylates K_{14} and that decreasing the substrate flow rate increases the yield of acetylated product. This result supports other immobilized enzyme systems that report an increase in product yield at decreasing flow rates−likely attributed to mass transfer effects.[169,170] Next, we ran a control experiment where we flowed a synthetically citrullinated H3 peptide (CitK) at 0.1 uL min^{-1} over immobilized Snap-PCAF to confirm that citrullination decreases the yield of acetylated peptide (Figure 6.10).

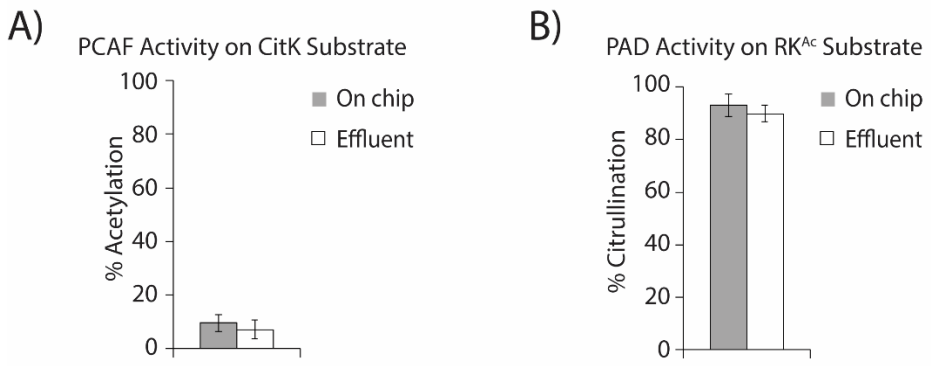

Figure 6.10 PAD and PCAF controls in the device. A) Acetylated product yield when the synthetically citrullinated (CitK) substrate was flowed over immobilized Snap-PCAF at 0.1 µL min-1. B) Citrullinated product yield when the synthetically acetylated H3 substrate (RKAc) was flowed over immobilized Halo-PAD at 0.1 µL min-1. Mean ± SD (n=3).

To determine the product yield from the collected effluent, we incubated the effluent for 1 h on a separate chip presenting a maleimide at a density of 10%. We repeated the SAMDI-MS analysis steps previously described for each flow rate. The product yield calculated on the reactor chip matched the product yield on the collected effluent chip, demonstrating that the

reaction and analysis can both be carried out on the reactor chip. This saves time and material associated with collecting the effluent for subsequent analysis.

Single enzyme reactions with immobilized PAD. We performed analogous experiments to confirm the citrullination of the peptide by PAD. Using a mass spectrometric readout was challenging because conversion of arginine to citrulline increases the substrate mass by only 1 Da. To address this problem, we chemically derivatized the citrulline moiety by reaction with phenylglyoxal prior to analysis with SAMDI-MS (Figure 6.11A).

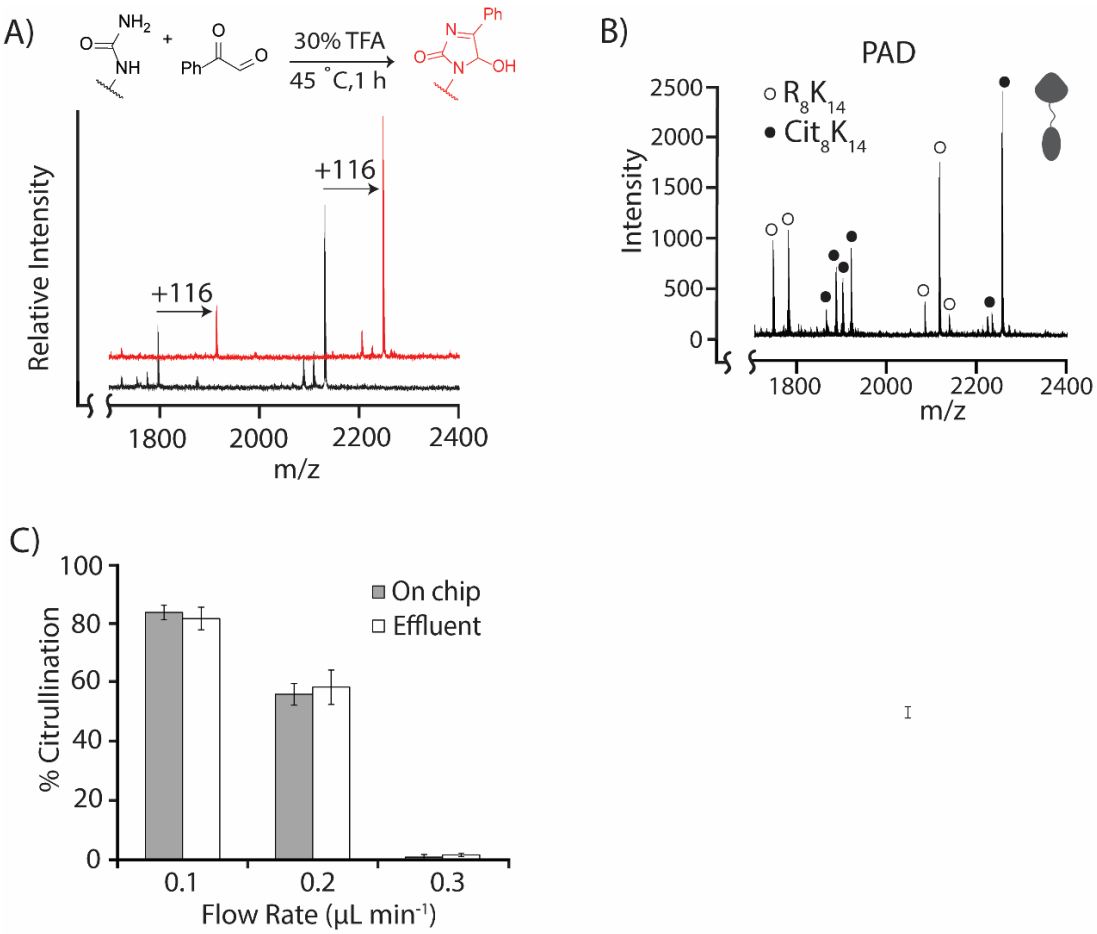

Figure 6.11 PAD activity in the device. a) SAMDI-MS spectra of unconverted substrate (black, RK^{Ac}) after treatment with phenylglyoxal shows no mass shift. Treating citrullinated substrate (red, $CitK^{Ac}$) with phenylglyoxal is quantitative and increases the mass by 116 Da. b) SAMDI-MS spectrum of the collected effluent labeled with phenylglyoxal from the PAD reactor. The proton, sodium, and potassium monoisotopic substrate peaks (open circles) and product peaks (closed circles) were integrated to calculate the percent of citrullinated product. c) The citrullinated product yield was calculated at different flow rates from the collected effluent and on the reactor chip. Mean ± SD (n=3).

Phenylglyoxal has been previously shown to specifically react with the urea group of citrulline residues using acidic conditions at elevated temperatures.[171] To initially demonstrate that this labeling strategy works well on the self-assembled monolayers presenting the H3 peptide, we immobilized the H3 peptide containing residues R_8K_{14} and Cit_8K_{14} on separate

monolayers. We applied a solution of phenylglyoxal in 30% trifluoroacetic acid in water at 45 °C for 45 min. We observed complete conversion of the Cit_8K_{14} peptide to the expected phenylglyoxal adduct, as indicated by a +116 Da mass increase. None of the un-citrullinated R_8K_{14} peptide was converted to the phenylglyoxal adduct, demonstrating that this method is selective for citrulline. We also showed that this method is quantitative by immobilizing known ratios of $R_8K_{14}^{Ac}$ and $Cit_8K_{14}^{Ac}$ peptide and determining the percent of 'product' formation from the SAMDI spectra (Figure 6.12). Phenylgloyxal selectively modified the citrulline moiety in a mixture of arginine and citrulline-containing peptides. This experiment also demonstrates that the two peptides bind to the self-assembled monolayer at approximately the same rate.

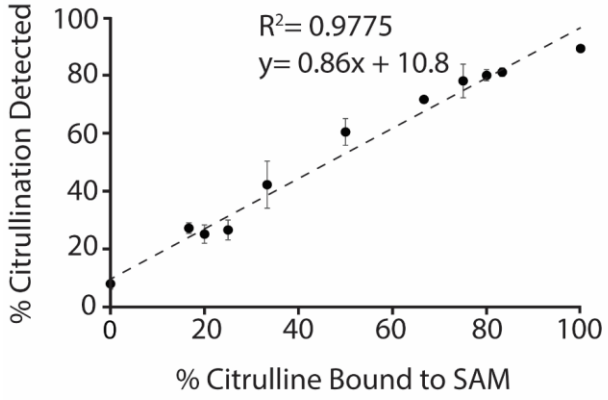

Figure 6.12 Using phenylglyoxal to quantitate the level of citrullinated product. Known ratios of $R_8K_{14}^{Ac}$ $Cit_8K_{14}^{Ac}$ were mixed and applied to a self-assembled monolayer. SAMDI-MS spectra were aquired from each ratio and the % citrullination was quantified. The amount of citrullination was plotted against each known peptide ratio. A linear fit (R^2= 0.9775, slope= 0.86) shows that the phenylglyoxal modification can be used to quantitate the amount of citrullinated product. Mean ± SD (n=3).

Using the same assay described for Snap-PCAF, we confirmed deiminase activity of immobilized Halo-PAD. After treating the reactor chip and collected effluent chip with

phenylglyoxal, the SAMDI-MS spectra revealed a +116 mass shift indicative of the H3 peptide with phenylglyoxal-modified citrulline. Next, we studied the effect of flow rate on PAD citrullination by preparing separate reactors for each flow rate experiment (Figure 6.11C). Similar to PCAF, the yield of citrullinated product increases when flow rate decreases. However, conversion by PAD appears to be more sensitive to changes in flow rate than does PCAF.

Spatiotemporally controlled tandem enzyme reactions. PCAF and PAD participate in a 'crosstalk' where they act on a peptide derived from histone H3. Initial citrullination of R_8 strongly decreases the acetylation of residue K_{14} by PCAF. Hence, the three products that follow from treatment of the peptide by the two enzymes— $R_8K_{14}^{Ac}$, Cit_8K_{14}, and $Cit_8K_{14}^{Ac}$— are formed in different yields depending on the order of enzyme treatment. We controlled the order of the two reactions by sequentially patterning PCAF and PAD along the reactor chip. Using the 'NU' PDMS block as a reference (Figure 6.7B) we prepared two reactor chips labeled pattern I and pattern II. Pattern I was generated by binding the SnapTag ligand for PCAF capture on the upstream 'N' and the HaloTag ligand for PAD capture on the downstream 'U' region. Pattern II was generated by binding the HaloTag ligand for PAD capture on the upstream 'N' and the SnapTag ligand for PCAF capture on the downstream 'U' region (Figure 6.13A, 6.13B). To immobilize each enzyme, we flowed Halo-PAD, buffer, and then Snap-PCAF through the channel. We then flowed the substrate (100 μM) at 0.1 μL min^{-1} and analyzed the products that were captured to the monolayer as described earlier. The flow rate of 0.1 μL min^{-1} was chosen because it resulted in the highest acetylated and citrullinated product yield within a reasonable operating time of 3.5 h. SAMDI-MS spectra reveal peaks with a +116 Da and +158 Da mass shift, representing the Cit_8K_{14} and $Cit_8K_{14}^{Ac}$ products, respectively, in both patterns (Figure

6.13C, 6.13D). Mass spectra from pattern I show that $Cit_8K_{14}^{Ac}$ and Cit_8K_{14} are the major products that comprise approximately 90% of the product fraction. Strikingly, the spectra from pattern II reveal only one major product, Cit_8K_{14}, that comprises approximately 70% of the product fraction. The remainder of the product fraction in pattern II consists of small quantities of R_8K_{14}, $R_8K_{14}^{Ac}$, and $Cit_8K_{14}^{Ac}$. The differences in product composition from patterns I and II reveals a strong dependence on enzyme order in the production of Cit_8K_{14} and $Cit_8K_{14}^{Ac}$. Taken together, spatiotemporally organizing both enzymes on the chip gave distinct products that were consistent with the PAD-dependent crosstalk. Additionally, the product yield on the reactor chip approximates the product yield from the effluent in both patterns. This feature adds great utility to the reactor as the analysis is performed directly on the chip.

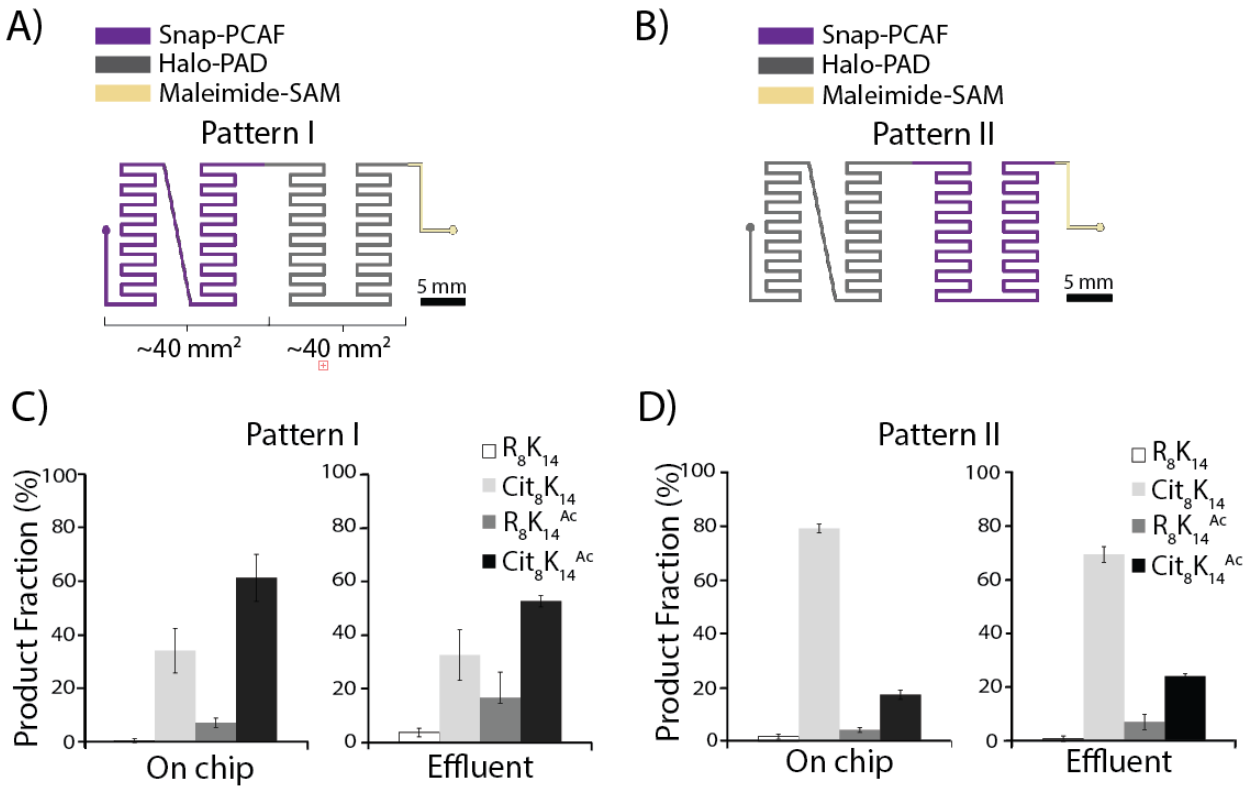

Figure 6.13 PAD and PCAF tandem activity. a) Regions of the fluidic channel with Snap-PCAF (purple), Halo-PAD (grey), and available for effluent capture (gold). The fluidic channel has a 'NU' design, where each enzyme is patterned on either the 'N' or the 'U' and the 'N' and 'U' each have a surface area of 40 mm^2. Pattern I has Snap-PCAF patterned on the 'N' and Halo-PAD patterned on the 'U' b) Quantitation of R_8K_{14}, $R_8K_{14}^{Ac}$, Cit_8K_{14}, and $Cit_8K_{14}^{Ac}$ yields on the reactor chip and from the collected effluent in pattern I. Mean ± SD (n=3). c) Pattern II has Halo-PAD patterned on the 'N' and Snap-PCAF patterned on the 'U' d) Quantitation of R_8K_{14}, $R_8K_{14}^{Ac}$, Cit_8K_{14}, and $Cit_8K_{14}^{Ac}$ yields on the reactor chip and from the collected effluent in pattern II. A reduction in $Cit_8K_{14}^{Ac}$ and increase in Cit_8K_{14} is observed in pattern II, where PAD precedes PCAF in the reaction sequence. Mean ± SD (n=3).

6.3 Discussion

In this chapter, we describe a spatiotemporal approach for organizing enzymes and substrates that participate in a multi-step reaction. We use a microfluidic device paired with self-assembled monolayers to enable enzymes to be sequentially patterned along the chip surface. In this way, a substrate introduced into a flowing buffer encounters the enzymes separately and in

an order dictated by the direction of flow. Because we used two enzymes that install post-translational modifications on a peptide substrate— and where there is a 'crosstalk' between the enzymes— we demonstrated that the major product depended on the order of enzyme treatment. This principle, where the spatiotemporal organization of a common set of reactants can give different reaction products, is a common feature in biology but remains little explored in traditional organic synthesis.[172]

The device benefits from a modularity which allowed us to study a reaction sequence step-by-step and analyze the products on the same chip. The ability to independently vary the position of each enzyme and the reaction time of the substrate over the immobilized enzymes gave us distinct product mixtures. In addition, the ability to perform a multistep enzyme reaction and quantify the reaction products directly on the fluidic chip simplified analysis while negating the need to sacrifice effluent for downstream product analysis. This single-surface approach to reactivity and detection should be broadly applicable to other multi-enzyme reaction systems.

It is significant that the product yields from the collected effluent approximately equal the yield observed on the reactor chip. The lateral channel length required for complete mixing in the axial direction at 0.1, 0.2, 0.3, and 0.4 μL min^{-1} flow rates was 61.7, 123.4, 185.1, and 246.84 μm, respectively (D= 4.22 x 10^{-6} cm^2 s^{-1} [173]).[174] The diffusion lengths were very small compared to the length of the microfluidic channels (~181.2 mm `N`, ~181.2 mm `U`, ~12.5 mm maleimide capture region), thus the exchange between the reaction products and bulk occurred rapidly and did not generate large concentration gradients throughout the length of the device. We also referred to work by Manalis and coworkers to consider the possible generation of a thin depletion layer of peptide directly above the immobilized enzyme and maleimide capture

regions.[175] That work reported COMSOL simulations of biosensors with analyte flowing into a rectangular channel and becoming captured in a downstream region. We found that a depletion zone does not exist over the immobilized enzyme ('N' or 'U'), and a very thin depletion zone relative to the height of the channel exists over the maleimide capture region. We expect that this thin depletion zone lowered the concentration of analyte directly above the maleimide capture region. We observe complete binding of analyte to the maleimide throughout the capture region, confirming that the depletion zone does not lower the concentration of the analyte enough to prevent complete reaction with the surface.

Patterning two enzymes on a microfluidic chip facilitated the conversion of the substrate first to an intermediate, and finally to the product. Three recent reports also describe the patterning of two enzymes on a solid support and observed enhanced rates of product formation through substrate channeling.[176–178] Those examples did not use flow to deliver the intermediate to the second enzyme but instead relied on diffusion. Our example ensures a more efficient transfer of the intermediate to the second enzyme. Further, microfluidic devices have a large surface-to-volume ratio and small length scales that allow for fast mass transfer, which can serve to remove inhibitory products and reduce product inhibition of the enzymes.[148] We believe that this approach can be applied towards the biochemical production of target compounds, which would require calculating the apparent Michaelis constant ($K_{m,app}$) and k_{cat} of the immobilized fusion enzymes for optimizing reaction efficiency and productivity. Future studies will focus on optimizing flow rate and substrate concentration to maximize the product output using a minimum channel surface area.

The use of self-assembled monolayers enabled important features of our approach. Taking advantage of the ability to control the surface chemistry, we were able to use enzyme-reactant pairs to covalently functionalize the surface with enzymes of interest. A tri(ethylene glycol) background provided resistance to nonspecific adsorption, giving the necessary control needed to pattern proteins. Additionally, the self-assembled monolayers provided an elegant way of capturing and analyzing the resulting products of the enzyme reactions directly on the chip. The reaction products were flowed over and captured on regions of monolayer functionalized with maleimide, allowing the products to be analyzed directly by SAMDI-MS. SAMDI-MS has been applied to measuring a broad range of enzyme activities and offers a general method for quantitating reaction products.[179]

We were able to covalently and selectively pattern enzymes in defined regions on the 2D reactor surface by using orthogonal active site chemistries for immobilization. This allowed me to know exactly where each reaction took place and to control the reaction times of substrate and intermediates over the immobilized enzymes. DNA hybridization has also been used to pattern areas of active enzyme on a variety of DNA architectures in microfluidic and non-microfluidic systems.[176,177,180–185] This method has been applied towards studying single enzyme activities and multi-enzyme reaction cascades. Our approach uses covalently-bound enzymes that generate a permanent bond between the enzyme and the surface. Expressing the handle for protein immobilization as a fusion protein is advantageous because it does not require chemical modification of the enzymes after expression−a process which can reduce enzyme activity and yield.

We also showed that phenylglyoxal can be used to selectively modify citrullinated products for detection by mass spectrometry. This method has wide applications beyond the system reported in this chapter, as recent work has suggested that the PAD family of enzymes play pathophysiological roles in a variety of human diseases including rheumatoid arthritis, psoriasis, cancer, Alzheimer's disease and multiple sclerosis.[186] Compounds that inhibit certain PAD isoforms show promise in treating or slowing down the progression of these diseases.[187,188] Profiling the substrate specificity of PAD isoforms will generate insight for developing selective inhibitors.[189] Previous assays have used trypsin to detect citrullination with mass spectrometry because it cleaves after arginine residues but not citrulline residues.[190] However, trypsin also cleaves lysine residues, which complicates the analysis of substrates containing a mixture of trypsin cleavage sites. Phenylglyoxal labeling is a direct and quantitative method for identifying the substrate specificity of PAD isoforms on different peptide sequences.[191] We were able to quantitatively label $CitK^{Ac}$ and CitK with phenylglyoxal to address the extent of citrullinated product yield on the reactor chip.

We also describe a method to cast PDMS directly onto 3D printed molds, overcoming the time and facility barriers constraining current photolithographic methods to prepare PDMS molds. 3D printing enabled us to rapidly prototype different mold designs and build many mold replicates in less time without the need for specialized facilities. We describe a method that only requires a heat treatment step after 3D printing to allow PDMS polymerization and rapid removal. This method can be applied to a wide variety of channel designs as well as in applications outside of microfluidics such as single cell analysis, nanoparticle synthesis, and soft

robotics.[192–194] Future work may use 3D printing to create the entire microfluidic device, as described by Folch and coworkers.[195,196]

6.4 Conclusion

The approach we describe in this chapter may be extended to other enzyme-mediated transformations for targeted biosynthesis of products and mixtures. Advantages over existing procedures that use packed-bed capillaries or planar supports are that reaction product depends on the order of enzyme covalently immobilized to the channel floor and that product analysis occurs on the chip.[149,153] Tuning the flow rate and order of patterned enzymes allows for the step-by-step optimization of complex biosynthetic pathways. We believe that this method can be extended to systems involving three or more enzymes using cutinase-, CLIP-, or tetracysteine-tagged proteins in addition to the HaloTag and SnapTag systems presented in this work.[161,197,198] Systems that rigorously separate and control the order of enzyme reactions can be used for accessing specific biosynthetic products in high yields. We believe this approach is simpler and more versatile than many other methods for carrying out and studying multistep enzyme reactions, and it will find many applications in biochemical syntheses.

6.5 Experimental

Reagents. THAP, acetyl coenzyme A, phenylglyoxal hydrate, β-D-thioglucose sodium salt, and complete protease inhibitor tablets (EDTA-free) were purchased from Sigma Aldrich. Amino acids and peptide synthesis reagents were purchased from Anaspec. pET-16b vectors encoding for Snap-PCAF and PAD1 were obtained from Thermo Fisher Scientific- GeneArt with

the codons optimized for *E. coli* expression. Oligonucleotide primers were purchased from Integrated DNA Technologies. Bug Buster (10x) was purchased from EMD Millipore. BL21DE3 *E. coli* and Gibson Assembly Master Mix were purchased from New England Biolabs. BL21DE3pLysS *E. coli* was purchased from Promega. PDMS prepolymer mixture was purchased from Ellsworth Adhesives. Neodymium magnets were purchased from Ace Hardware and Amazon.com. The H3 peptide (Ac-TARK^{Ac}STGGKAPC), acetylated H3 peptide (Ac-TARK^{Ac}STGGK^{Ac}APC), and citrullinated H3 peptide (Ac-TACitK^{Ac}STGGK^{Ac}APC) were prepared using standard Fmoc solid phase peptide synthesis methods on Rink Amide MBHA resin.[199]

Assembly of Halo-PAD construct. Halo-PAD was assembled using standard Gibson assembly protocols (New England Biolabs) using polymerase chain reaction (PCR) from a vector containing HaloTag and a vector containing $(EAAAK)_4$-PAD. The primers used to PCR the vector containing HaloTag are: 5'-CCATATCGAAGGTCGTCATATGGAAATCGGTACTGGCTTTCC-3' (forward) and 5'-GCTGCTGCTTCCAATTGAATCTCCAGAGTAGACAGCC-3' (reverse). The primers to PCR the vector containing $(EAAAK)_4$-PAD are: 5'-GGCTGTCTACTCTGGAGATTCAATTGGAAGCAGCAGC-3'(forward) and 5'-GGAAAGCCAGTACCGATTTCCATATGACGACCTTCGATATGG-3' (reverse).

Protein expression and purification. To express Snap-PCAF, the vector was transformed into BL21DE3 *E. coli* using chemical transformation methods. A stab of Snap-PCAF BL21DE3 was added to 2xYT media (5 mL) with carbenicillin and allowed to grow overnight at 30 °C while shaking at 240 rpm. The next morning, the culture was added to 2xYT media (500 mL) supplemented with carbenicillin (100 μg mL^{-1}) and grown at 30 °C while shaking until the OD_{600} reached ~0.45. The culture was cooled at 4 °C and Snap-PCAF expression was induced with 0.5 mM IPTG overnight under shaking at 16 °C. The bacteria were pelleted by centrifugation and lysed in buffer (50 mM Tris pH 8.5, 200 mM NaCl, 5 mM β-mercaptoethanol, 50 mL) containing Bug Buster (10x, 2 mL) and one cOmplete-Mini protease inhibitor tablet. The overexpressed Snap-PCAF contains a N'-terminal His tag and was purified on a nickel immobilized metal affinity chromatography (IMAC) column. Fractions eluted off of the nickel column were combined and concentrated to 1 mL in a 25 mL Amicon 10 kDa cutoff Centrifugal Filter Unit (Millipore). The Snap-PCAF was further purified using size exclusion chromatography on an Akta FPLC (GE Healthcare) using running buffer (50 mM Tris pH 8.5, 200 mM NaCl). Fractions containing Snap-PCAF were confirmed by SDS-PAGE, pooled and concentrated, and stored at -80 °C in 50% glycerol. To express Halo-PAD, the vector was transformed into BL21DE3pLysS *E. coli* using chemical transformation methods. A stab of Halo-PAD BL21DE3 was added to 2xYT media (5 mL) with carbenicillin and allowed to grow overnight at 30 °C while shaking. The culture was then added to 2xYT media (500 mL) supplemented with carbenicillin and grown at 30 °C with shaking until the OD_{600} reached ~0.50. The culture was cooled at 4 °C and Halo-PAD expression was induced with IPTG (0.5 mM) overnight under shaking at 25 °C. The bacteria were pelleted by centrifugation and lysed in buffer (50 mL) Tris pH 8.0 (50 mM), NaCl

(300 mM), containing 10 x Bug Buster (2 mL) and one Complete-Mini protease inhibitor tablet. The overexpressed Halo-PAD also contained a N'-terminal His tag and was purified on a nickel resin column. Fractions eluted off of the nickel column were combined and concentrated to 1 mL in a 25 mL Amicon 50 kDa cutoff Centrifugal Filter Unit (Millipore). The Halo-PAD was further purified using size exclusion chromatography on an Akta FPLC (GE Healthcare) using running buffer Tris pH 8.0 (50 mM), NaCl (300 mM). Fractions containing Halo-PAD were confirmed by SDS-PAGE, pooled and concentrated, and stored at -80 °C in 50% glycerol.

3D printing molds. The two mold designs in Figure 6.6 were rendered on SolidWorks software. The first consists of a single winding channel to test individual PCAF and PAD activity, while the second contains a single channel spelling out 'NU' to test both PCAF and PAD activities. The channel width and height was 250 µm x 250 µm, and the inlet and outlet diameters were 800 µm for both designs. The files were converted to .stl format and printed in digital printing mode using a Stratasys Connex 350 3D printer in VeroWhite material (Stratasys Direct) with a glossy finish. The designs were organized on the build surface so that the printing striations lie parallel to the longest side of each part. The support material was placed on the bottom of the mold not contacting the channel features. I included 3 mm walls in our mold design because I found that PDMS will not polymerize on the side of the mold previously exposed to support material even after several 43 °C heat treatment cycles. After printing, the support material was removed with a WaterJet. The 3D printed parts were washed with ultrapure water, dried over a nitrogen stream, and placed in a 43 °C oven for 48 h before using as PDMS molds. I noticed that the PDMS did not polymerize on the mold without this heat treatment.

Self-assembled monolayer preparation on gold surfaces. Standard glass microscope slides were cleaned using ethanol and water in a sonication bath. An electron beam evaporator was used to deposit 5 nm Ti (0.02 nm s^{-1}) followed by 30 nm Au (0.05 nm s^{-1}). Two types of slides were prepared for each experiment: the microfluidic reactor slides and the effluent capture slides. The microfluidic reactor slides were soaked overnight at 25 °C in an ethanolic solution (0.5 mM total disulfide concentration); the solution had a 1:9 of an asymmetric disulfide terminated with a maleimide group and a tri(ethylene glycol) group, and a symmetric disulfide terminated with tri(ethylene glycol) groups. Likewise, the effluent capture slides were soaked overnight under the same conditions except for the ratio of asymmetric: symmetric disulfide, which was changed to 1:4. The slides were then rinsed with ethanol and water. A glass etcher was used to create a marking 16.8 mm from the short edge of the Au slide, indicating the location of the outlet. For studies where only PCAF or PAD were bound to the slide, another marking was made 24.6 mm away from the same edge of the Au slide. This second marking indicated the boundary between the enzyme binding region and the product capture region. A rectangular piece of PDMS 3 mm in width and height was aligned to the right of the 24.6 mm marking, in between the 24.6 mm marking and 16.8 mm marking. Neodymium magnets were placed on the top of the PDMS piece and on the bottom of the slide, securing the PDMS onto the slide and establishing a physical boundary for the effluent capture region and enzyme immobilization region. A solution (200 µL) containing either the HaloTag immobilization ligand (100 µM) or SnapTag immobilization ligand (100 µM) in Tris pH 8.0 (100 mM), Triton X-100 (0.01%) was pipetted onto the enzyme binding region and incubated at 25 °C for 1 h in a

humidity chamber. β-D-thioglucose was used to block the maleimide groups for the control experiments. The chips were rinsed with ethanol and water, and dried under a stream of N_2. For experiments involving PAD and PCAF to be present on the same chip, two additional markings were made in addition to the 16.8 mm marking; the first was made 23.01 mm away from the same edge of the Au slide, and the second was made 40.37 mm away from the same edge of the Au slide. A rectangular piece of PDMS was aligned to the right of the 40.37 mm marking and secured with neodymium magnets. A solution (200 µL) containing either the HaloTag immobilization ligand (100 µM), SnapTag immobilization ligand (100 µM), or β-D-thioglucose (100 µM) in Tris pH 8.0 (100 mM), Triton X-100 (0.01%) was pipetted onto the enzyme binding region and incubated at 25 °C for 1 h in a humidity chamber. Afterwards, the chips were rinsed with ethanol and water, and dried under a stream of N_2. Next, the same process was repeated with the second immobilization ligand or β-D-thioglucose using a piece of PDMS to block the 23.01 mm marking next to the effluent capture region. The chips were rinsed again with ethanol and water, and dried under a stream of nitrogen.

Microfluidic chip fabrication. PDMS prepolymer mixture was mixed in a 1:10 ratio (w/w curing agent to prepolymer), degassed in a vacuum desiccator for 15 min, and poured into a 3D printed mold. The mold containing PDMS was degassed in a vacuum desiccator for 15 min and then placed in a 43 °C oven overnight. The PDMS blocks were then peeled off of the mold and treated in a 130 °C oven for 10 min. The 3D printed molds were reused for additional PDMS curing cycles. A 0.8 mm biopsy punch was used to generate inlet and outlet ports in the PDMS block. Once the self-assembled monolayer was prepared with the appropriate enzyme

immobilization ligands, the PDMS block was treated with 50 W air plasma for 35 s at 200 mTorr using a Solarus Plasma Cleaner. The PDMS block was immediately aligned with the glass slide so that the outlet port was located over the effluent capture region 16.5 mm from the edge of the slide. The simple meandering channel design was used for chips only presenting one immobilization ligand while the 'NU' design was used for chips presenting both capture ligands. The PDMS and Au chip assembly was then placed in a clamp made from extruded polycarbonate and secured by screws (Figure 6.14). PTFE tubing was inserted into the outlet. Silicon tubing was placed in the inlet and connected to a syringe with $CaCl_2$ (10mM) and a 1:1 mixture of Tris pH 8.5 (100 mM), NaCl (50 mM), Triton X-100 (0.01%): PBS pH 7.4 (1 x), Triton X-100 (0.01%). The chip was primed with this buffer using a syringe pump (Harvard Apparatus) at 2.0 µL min^{-1} for 20 min. The buffer was freshly prepared before the start of each experiment and kept chilled at 4 °C when not in use.

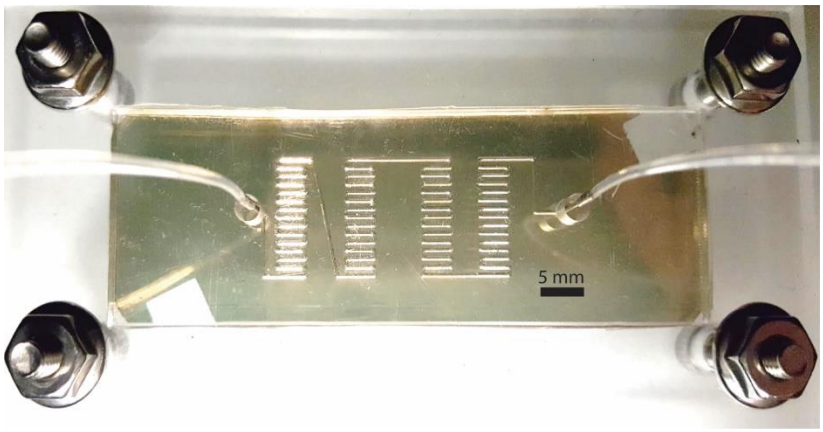

Figure 6.14 Photograph of the NU fluidic chip and clamp assembly.

Chip operation for individual Snap-PCAF and Halo-PAD activities. For chips only presenting the SnapTag immobilization ligand, a solution of Snap-PCAF (500 nM) was prepared in buffer with $CaCl_2$ (10 mM) and a 1:1 mixture of Tris pH 8.5 (100 mM), NaCl (50 mM), Triton X-100 (0.01%): PBS pH 7.4 (1 x), Triton X-100 (0.01%). The Snap-PCAF solution was injected into the microfluidic chip at 1.0 µL min^{-1} for 35 min. Then, the inlet silicon tubing was replaced with PTFE tubing and buffer containing a $CaCl_2$ (10 mM) and a 1:1 mixture of Tris pH 8.0 (100 mM), NaCl (50 mM): PBS pH 7.4 (1 x), Triton X-100 (0.01%) was flowed for 5 min at 5.0 µL min^{-1}. The outlet tubing was disconnected from the channel and dried with a stream of N_2. A buffer containing the H3 peptide (100 µM), $CaCl_2$ (10 mM), and acetyl coenzyme A (100 µM) in 1:1 of Tris pH 8.0 (100 mM), NaCl (50 mM): PBS pH 7.4 (1 x), Triton X-100 (0.01%) was flowed at 0.1, 0.2, 0.3, or 0.4 µL min^{-1} for 1.5 reactor volumes. The clamp and PDMS assembly was disassembled from the Au reactor chip, washed with ethanol and water, and dried under N_2. The effluent in the outlet line was collected in a microcentrifuge tube. The collected effluent was reduced with TCEP (100 µM) for 10 min, and 2.5 µL was spotted onto an effluent capture slide. The effluent was incubated on the slide for 1 h at 25 °C, rinsed with ethanol and water, and dried under N_2. The method for determining PAD activity was carried out using the same conditions stated above, except that a solution of Halo-PAD (200 nM) was flowed into the device and phenylglyoxal was used to modify the citrullinated product. To carry out the phenylglyoxal modification, a solution of phenylglyoxal hydrate (7.6 mg, 56.7 mmol) in trifluoroacetic acid and H_2O (30% trifluoroacetic acid, 70% H_2O, 0.5 mL) was freshly prepared. The solution (200 µL) was applied to the microfluidic reactor slide and the slide previously incubated with the collected effluent. The phenylglyoxal solution was incubated for 45 min at 45 °C, rinsed with ethanol and

water, and dried under N_2. A solution of THAP (25 mg mL^{-1}) in acetone (50 µL) was applied to each chip and the chips were analyzed using an AB Sciex 5800 MALDI TOF/TOF mass spectrometer. On the microfluidic reactor chip, spectra were obtained from the effluent collection region. Data Explorer software was used to measure the area under the monoisotopic peaks of the disulfides and thiolates (AB Sciex). This procedure was repeated for control studies with immobilized Snap-PCAF and Halo-PAD using the citrullinated H3 peptide (Ac-TACitK^{Ac}STGGKAPC) and acetylated H3 peptide (Ac-TARK^{Ac}STGGK^{Ac}APC), respectively at 0.1 uL min^{-1}. All experimental conditions were repeated three times with three spectra obtained per experimental replicate.

Chip operation for combined Snap-PCAF and Halo-PAD activity. After priming the chips presenting both immobilization ligands, a solution of Halo-PAD (200 nM) was prepared in a buffer with $CaCl_2$ (10 mM) and a 1:1 mixture of Tris pH 8.5 (100 mM), NaCl (50 mM), Triton X-100 (0.01%): PBS pH 7.4 (1 x), Triton X-100 (0.01%). The Halo-PAD solution was injected into the microfluidic chip at 1.0 µL min^{-1} for 35 min. Then, the same buffer without containing Halo-PAD was injected at 5.0 µL min^{-1} for 5 min. Next, a solution of Snap-PCAF (500 nM) was prepared in a buffer with $CaCl_2$ (10 mM) and a 1:1 mixture of Tris pH 8.5 (100 mM), NaCl (50 mM), Triton X-100 (0.01%): PBS pH 7.4 (1 x), Triton X-100 (0.01%). The outlet tubing was disconnected from the channel and dried with a stream of N_2. the H3 peptide (100 µM) in a buffer with $CaCl_2$ (10 mM) and 1:1 Tris pH 8.0 (100 mM), NaCl (50 mM) and PBS pH 7.4 (1x) was flowed at 0.1 µL min^{-1} for 1.5 reactor volumes. The remainder of the steps, including the phenylglyoxal modification step, were kept the same as previously described.

Reactions to generate a phengylyoxal response curve. Standard glass microscope slides were cleaned using ethanol and water in a sonication bath. An electron beam evaporator was used to deposit 5 nm Ti (0.02 nm s^{-1}) followed by 30 nm Au (0.05 nm s^{-1}). The slides were soaked overnight at 25 °C in an ethanolic solution (0.5 mM total disulfide concentration); the solution had a 1:4 of an asymmetric disulfide terminated with a maleimide group and a tri(ethylene glycol) group, and a symmetric disulfide terminated with tri(ethylene glycol) groups. The slides were then rinsed with ethanol and water. Different solutions containing Ac-TARK^{Ac}STGGK^{Ac}APC and Ac-TACitK^{Ac}STGGK^{Ac}APC (100 μM) were prepared in Tris HCl 8.0 (100 mM), consisting of Ac-TARK^{Ac}STGGK^{Ac}APC, Ac-TACitK^{Ac}STGGK^{Ac}APC, and different ratios of each peptide to generate a linear calibration curve. 2.5 μL of each peptide solution was individually spotted in separate areas of the slide to ensure that no mixing occurred and the slide was incubated in a humidity chamber for 1 h at 25 °C. The slide was rinsed with ethanol and water, dried under a stream of N_2, and reacted with phenylglyoxal as previously described. The slide was treated with THAP matrix (25 mg mL^{-1} in acetone) and three SAMDI-MS spectra were obtained from each spot. Adduct formation was quantified by calculating the integrated area under each monoisotopic peak as previously described.

Synthesis of SnapTag capture ligand. The synthetic route references Figure 6.15.

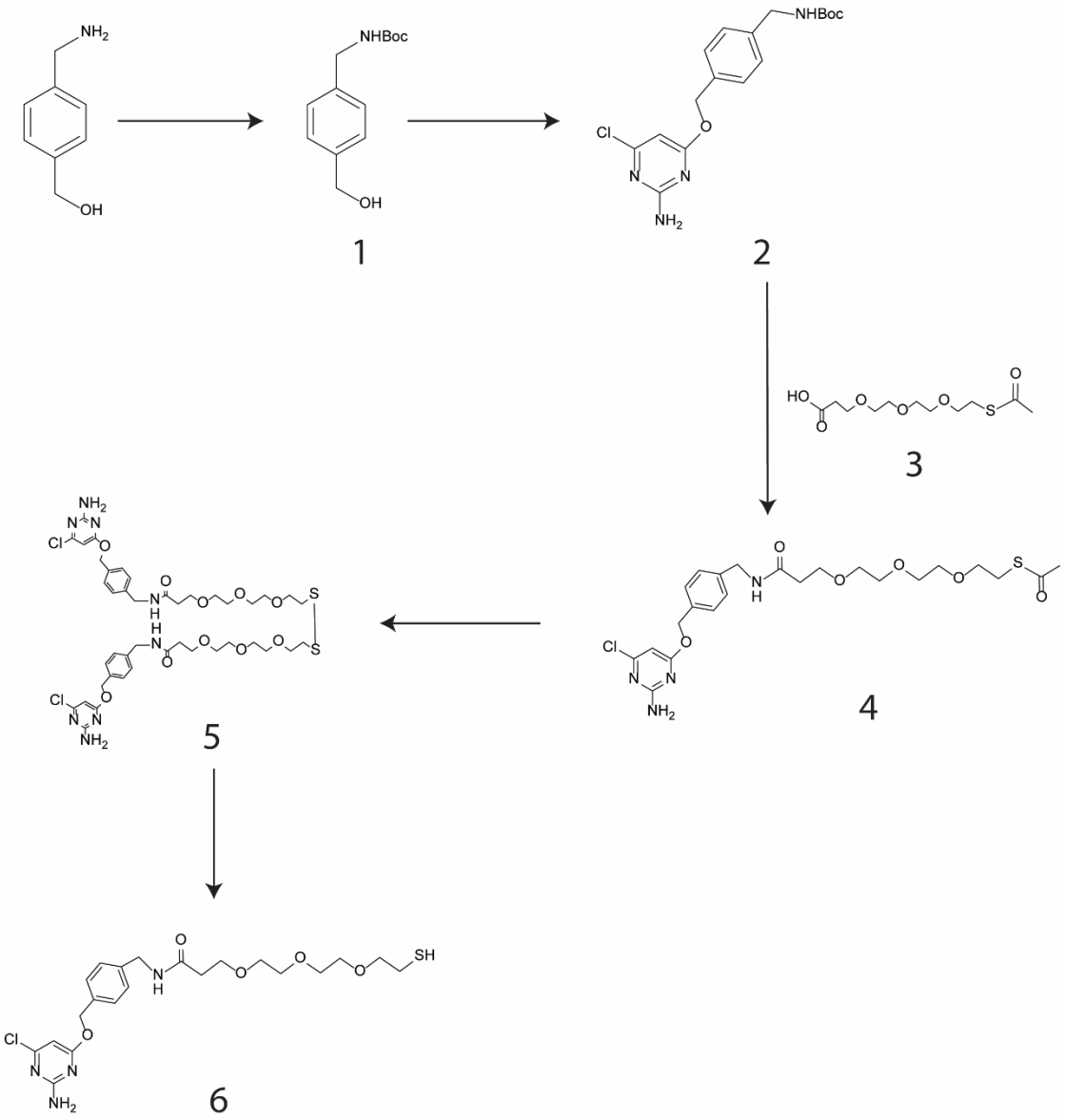

Figure 6.15 Synthesis of the SnapTag capture ligand.

Synthesis of tert-butyl (4-(hydroxymethyl)benzyl)carbamate (**1**). Di-tert-butyl dicarbonate (5.73 g, 25.4 mmol) was added to a stirred solution of (4-

(aminomethyl)phenyl)methanol (3.0 g, 21.9 mmol) in MeOH (90 mL) stirred 12 h at room temperature. The mixture was concentrated on a rotary evaporator to yield a yellow powder. The reaction product was purified via flash chromatography using 1:1 hexanes:EtOAc, to obtain the product (**1**) as a white powder (2.745 g, 91%): ^{1}H NMR (500 MHz, CD_3OD, δ): 7.34 (d, 2H), 7.28 (d, 2H), 4.82 (s, 1H), 4.68 (s, 2H), 4.31 (d, 2H), 1.61 (s, 1H), 1.46 (s, 9H); MS (ESI) *m*/*z*: $[M + Na]^+$ calcd for $C_{13}H_{19}NO_3$, 260.14; found, 260.08.

Synthesis of tert-butyl (4-(((2-amino-6-chloropyrimidin-4-yl)oxy)methyl)benzyl)carbamate (**2**). 2-amino-4,6-dichloropyridine (1.66 g, 10.1 mmol) was dissolved in 120 mL THF under stirring. To this mixture, compound **1** was added (2.00 g, 8.43 mmol). Potassium bis(trimethylsilyl) amide was slowly added to the mixture under stirring and allowed to react at room temperature for 12 h. The mixture was concentrated on a rotary evaporator and the resulting orange powder was resuspended in DCM, quenched with 1N HCl (150 mL), and transferred to a separatory funnel where the mixture was extracted with DCM (4 x 150 mL). The combined organic extracts were dried over $MgSO_4$, filtered, and concentrated on a rotary evaporator. The mixture was purified via flash chromatography using 5:1 hexanes:EtOAc, then 4:1 hexanes:EtOAc, to elute (**2**) as a white powder (1.29 g, 65%): ^{1}H NMR (500 MHz, $CDCl_3$, δ): 7.36 (d, 2H), 7.29 (d, 2H), 6.16 (s, 1H), 5.30 (s, 2H), 5.03 (s, 2H), 4.84 (s, 1H), 4.32 (d, 2H), 1.46 (s, 9H); MS (ESI) *m*/*z*: $[M + Na]^+$ calcd for $C_{17}H_{21}ClN_4O_3$, 387.13; found, 387.10.

Synthesis of S-(1-(4-(((2-amino-6-chloropyrimidin-4-yl)oxy)methyl)phenyl)-3-oxo-6,9,12-trioxa-2-azatetradecan-14-yl) ethanethioate (**4**). 500 mg of **2** was dissolved in DCM (3.0 mL, 1.37 mmol) , then trifluoroacetic acid (2.0 mL) was added to the mixture and stirred 12 h at room temperature. Cold ethyl ether (45.0 mL) was added and the mixture was stirred at -20 °C

for 24 h. A white precipitate was isolated by centrifugation (4,000 rpm, 4 min) and washed with ethyl ether (4 x, 45.0 mL). The compound was dried under high vacuum and yielded a white powder (485 mg, 97%). S-acetyl-PEG3-acid (compound **3**, 100 mg, 359 mmol), was dissolved in THF (1.8 mL). N-hydroxysuccinimide (45.2 mg, 395 mmol) and N,N'-diisopropylcarbodiimide (77.4 µL, 502.6 mmol) was added to the mixture and stirred for 12 h at room temperature. Then, the Boc-deprotected **2** (104.2 mg, 395 mmol) and triethylamine (54.8 µL, 395 mmol) were sequentially added to the mixture and stirred for 1.5 h at room temperature. The mixture was concentrated on a rotary evaporator and crude product (50 mg) was purified via preparative TLC with 9:1 DCM: MeOH to yield a viscous clear product (**4**) (35 mg, 70%): ^{1}H NMR (500 MHz, CD_3OD, δ): 7.40 (d, 2H), 7.32 (d, 2H), 6.11 (s, 1H), 5.35 (s, 2H), 4.41 (s, 2H), 3.77 (t, 2H), 3.61 (s, 4H), 3.55 (m, 6H), 3.05 (t, 1H), 2.52 (t, 2H), 2.32 (d, 2H), 1.12 (d, 3H); MS (ESI) *m*/*z*: $[M + H]^+$ calcd for $C_{23}H_{31}ClN_4O_6S$, 527.17; found, 527.15.

Synthesis of N1,N26-bis(4-(((2-amino-6-chloropyrimidin-4-yl)oxy)methyl)benzyl)-4,7,10,17,20,23-hexaoxa-13,14-dithiahexacosanediamide (5) and N-(4-(((2-amino-6-chloropyrimidin-4-yl)oxy)methyl)benzyl)-3-(2-(2-(2-mercaptoethoxy)ethoxy)ethoxy)propanamide (**6**). **4** (35 mg, .066 mmol) was dissolved in EtOH (465 µL), then ammonium hydroxide (35 µL, 0.5 M) was added and the solution reacted overnight at room temperature. The reaction mixture was concentrated on a rotary evaporator and redissolved in 3:1 ACN:H_2O (1.5 mL). Tris(2-carboxyethyl)phosphine was added (72.2 mg, 289 mmol) and stirred at room temperature for 1 h. 3:1 ACN:H_2O (1.5 mL) was added to the crude reaction mixture and the residue was purified via a Waters Delta 4000 HPLC using a C18 semi-prep scale column to yield a viscous clear compound **6** (12 mg, 34%): ^{1}H NMR (500 MHz,

CD_3OD, δ): 7.41 (d, 2H), 7.32 (d, 2H), 6.12 (s, 1H), 5.36 (s, 2H), 4.41 (s, 2H), 3.77 (t, 2H), 3.62 (s, 4H), 3.57 (m, 6H), 2.63 (t, 2H), 2.51 (t, 2H), 1.30 (s, 1H); MS (ESI) *m*/*z*: $[M + H]^+$ calcd for $C_{21}H_{29}ClN_4O_5S$, 485.15; found, 485.17.

Synthesis of HaloTag capture ligand. The synthetic route references Figure 6.16.

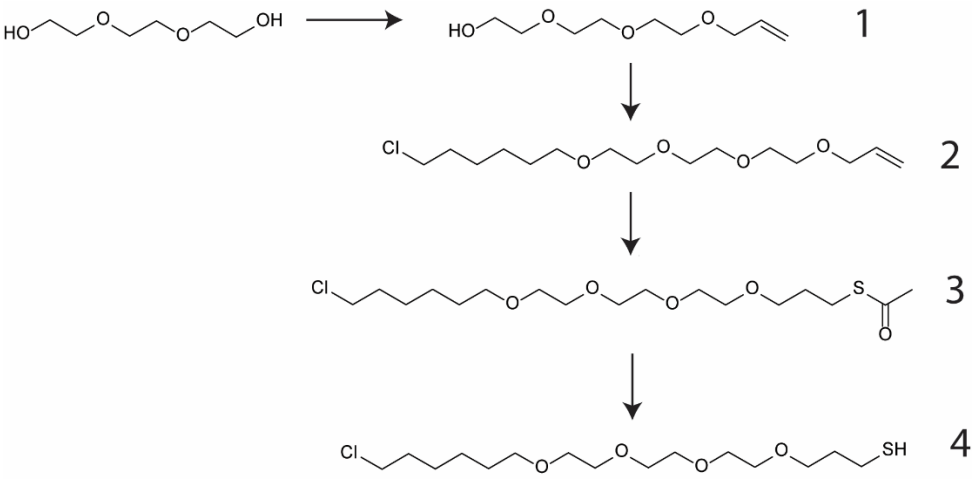

Figure 6.16 Synthesis of the HaloTag capture ligand.

Synthesis of 2-(2-(2-(allyloxy)ethoxy)ethoxy)ethan-1-ol (**1**). To rapidly stirring triethylene glycol (20 g, 133.2 mmol) was added 50% NaOH (aq) (1.07 g, 13.3 mmol). The mixture was allowed to stir 30 min after which, allyl bromide (1.61 g, 13.3 mmol) was added and the reaction heated to 90 °C for 16 h. After this period, the reaction was allowed to cool to r.t. and then poured into HCl (100 mL 1N). The aqueous phase was extracted with EtOAc (3 x 25 mL), the organic fractions then pooled and washed with saturated NH_4Cl (50 mL). The organic phase was dried over $MgSO_4$, filtered and concentrated to yield a clear oil. This oil was purified via flash chromatography on silica using 2:1 EtOAc / hexane as eluent. Product as a clear oil (0.55 g, 22%): ^1H NMR (500 MHz, $CDCl_3$, δ): 5.92 (m, 1H), 5.23 (dd, 2H), 4.03 (d, 2H), 3.73

(m, 2H), 3.68 (m, 6H), 3.62 (m, 4H), 2.43 (t, 1H); MS (ESI) *m*/*z*: $[M + Na]^+$ calcd for $C_9H_{18}O_4$, 213.12; found, 213.10.

Synthesis of 19-chloro-4,7,10,13-tetraoxanonadec-1-ene (**2**). Compound **1** (0.54 g, 2.84 mmol) was dissolved in dry THF (15 mL). To the solution was added dry sodium hydride (95%, 0.14 g, 5.68 mmol). After gas evolution ceased (~2 min), 1,6-dichlorohexane (4.40 g, 28.4 mmol) was added and the cloudy mixture heated to 60 °C for 14 hr with stirring. After this period, the reaction was concentrated, resuspended in water and EtOAc and poured into HCl (1N, 50 mL). The aqueous phase was extracted with EtOAc (3 x 10 mL), the organic fractions then pooled and washed with brine (50 mL). The organic phase was dried over $MgSO_4$, filtered and concentrated to yield a yellow oil. This oil was purified via flash chromatography on silica using 3:1 hexane / EtOAc as eluent. Product as a light yellow oil (0.71 g, 80%): ^{1}H NMR (500 MHz, $CDCl_3$, δ): 5.91 (m, 1H), 5.23 (dd, 2H), 4.02 (d, 2H), 3.65 (m, 8H), 3.59 (m, 4H), 3.53 (t, 2H), 3.46 (t, 2H), 1.77 (qui, 2H), 1.59 (m, 2H), 1.45 (m, 2H), 1.38 (m, 2H); MS (ESI) *m*/*z*: $[M + Na]^+$ calcd for $C_{15}H_{29}ClO_4$, 331.18; found, 331.28.

Synthesis of S-(19-chloro-4,7,10,13-tetraoxanonadecyl) ethanethioate (**3**). Compound **2** (0.69 g, 2.25 mmol) was dissolved in nitrogen-sparged MeOH (11 mL). To the solution was added thioacetic acid (0.48 mL, 6.75 mmol), followed by AIBN (0.02 g, 0.11 mmol). The mixture was then vented and placed in a UV photoreactor with stirring for 14 hr. After this period, the reaction was concentrated, resuspended in EtOAc and poured into $NaHCO_3$ (5% aq) (50 mL). The aqueous phase was extracted with EtOAc (3 x 10 mL), the organic fractions then pooled and washed with saturated NH_4Cl (50 mL). The organic phase was dried over $MgSO_4$, filtered and concentrated to yield a deep orange oil. This oil was purified via flash

chromatography on silica using 2:1 hexane / EtOAc as eluent. The product was a light orange oil (0.73 g, 84%): ^{1}H NMR (500 MHz, $CDCl_3$, δ): 3.65 (m, 10H), 3.58 (m, 4H), 3.52 (m, 4H), 3.46 (t, 2H), 2.95 (t, 2H), 2.32 (s, 3H), 1.85 (qui, 2H), 1.78 (qui, 2H), 1.60 (qui, 2H), 1.45 (m, 2H), 1.38 (m, 2H); MS (ESI) *m*/*z*: $[M + Na]^+$ calcd for $C_{17}H_{33}ClO_5S$, 407.17; found, 407.21.

Synthesis of 19-chloro-4,7,10,13-tetraoxanonadecane-1-thiol (**4**). Compound **3** (0.72 g, 1.87 mmol) was dissolved in EtOH (10 mL). To the solution was added HCl (12 M, 0.5 mL) and the reaction heated to reflux for 14 hr. After this period, the reaction was concentrated to ~2 mL and then poured into water. The aqueous phase was extracted with EtOAc (3 x 10 mL), the organic fractions then pooled and washed with saturated NH_4Cl (40 mL). The organic phase was dried over $MgSO_4$, filtered and concentrated to yield a yellow oil. This oil was purified via flash chromatography on silica using 1:1 hexane / EtOAc as eluent. Product as a light yellow oil (0.53 g, 82%): ^{1}H NMR (500 MHz, $CDCl_3$, δ): 3.65 (m, 8H), 3.58 (m, 6H), 3.53 (m, 2H), 3.46 (t, 2H), 2.62 (q, 2H), 1.88 (qui, 2H), 1.78 (qui, 2H), 1.59 (qui, 2H), 1.45 (m, 2H), 1.38 (m, 2H); MS (ESI) *m*/*z*: $[M + Na]^+$ calcd for $C_{15}H_{31}ClO_4S$, 365.16; found, 365.26.

Halo-PAD Sequence.

M G H H H H H H H H H H G S E I G T G F P F D P H Y V E V L G E R M H Y V D V G P R D G T P V L F L H G N P T S S Y V W R N I I P H V A P T H R C I A P D L I G M G K S D K P D L G Y F F D D H V R F M D A F I E A L G L E E V V L V I H D W G S A L G F H W A K R N P E R V K G I A F M E F I R P I P T W D E W P E F A R E T F Q A F R T T D V G R K L I I D Q N V F I E G T L P M G V V R P L T E V E M D H Y R E P F

LNPVDREPLWRFPNELPIAGEPANIVALVEEYMDWLHQSPV

PKLLFWGTPGVLIPPAEAARLAKSLPNCKAVDIGPGLNLLQ

EDNPDLIGSEIARWLSTLEISGEAAAKEAAAKEAAAKEAAAK

AAALEMAPKRVVQLSLKMPTHAVCVVGVEAHVDIHSDVPK

GANSFRVSGSSGVEVFMVYNRTRVKEPIGKARWPLDTDADM

VVSVGTASKELKDFKVRVSYFGEQEDQALGRSVLYLTGVDI

SLEVDTGRTGKVKRSQGDKKTWRWGPEGYGAILLVNCDRD

NHRSAEPDLTHSWLMSLADLQDMSPMLLSCNGPDKLFDSH

KLVLNVPFSDSKRVRVFCARGGNSLSDYKQVLGPQCLSYEV

ERQPGEQEIKFYVEGLTFPDADFLGLVSLSVSLVDPGTLPEV

TLFTDTVGFRMAPWIMTPNTQPPEELYVCRVMDTHGSNEKF

LEDMSYLTLKANCKLTICPQVENRNDRWIQDEMEFGYIEAP

HKSFPVVFDSPRNRGLKDFPYKRILGPDFGYVTREIPLPGPS

SLDSFGNLDVSPPVTVGGTEYPLGRILIGSSFPKSGGRQMAR

AVRNFLKAQQVQAPVELYSDWLSVGHVDEFLTFVPTSDQKG

FRLLLASPSACLKLFQEKKEEGYGEAAQFDGLKHQAKRSIN

EMLADRHLQRDNLHAQKCIDWNRNVLKRELGLAESDIVDIP

QLFFLKNFYAEAFFPDMVNMVVLGKYLGIPKPYGPIINGRC

CLEEKVQSLLEPLGLHCIFIDDYLSYHELQGEIHCGTNVRRK

PFPFKWWNMVP

Orange – pET16b vector encoded amino acids, Black – His-tag, Blue – HaloTag, Green – helical linker, Purple – restriction site encoded amino acids, red – PAD1

Snap-PCAF Sequence.

M G H H H H H H H H H H S S G H I E G R H M D K D C E M K R T T L D S P L G K

L E L S G C E Q G L H E I I F L G K G T S A A D A V E V P A P A A V L G G P E P L

M Q A T A W L N A Y F H Q P E A I E E F P V P A L H H P V F Q Q E S F T R Q V L W

K L L K V V K F G E V I S Y S H L A A L A G N P A A T A A V K T A L S G N P V P I L

I P C H R V V Q G D L D V G G Y E G G L A V K E W L L A H E G H R L G K P G L G

Q L E A A A K E A A A K E A A A K E A A A K A A A L E V I E F H V V G N S L N Q

K P N K K I L M W L V G L Q N V F S H Q L P R M P K E Y I T R L V F D P K H K T

L A L I K D G R V I G G I C F R M F P S Q G F T E I V F C A V T S N E Q V K G Y G T

H L M N H L K E Y H I K H D I L N F L T Y A D E Y A I G Y F K K Q G F S K E I K I P

K T K Y V G Y I K D Y E G A T L M G C E L N P R I P Y T E

Orange – pET16b vector encoded amino acids, Black – His-tag, Purple – restriction site encoded amino acids, pink – SnapTag, green – helical linker, grey – PCAF

Chapter 7

Summary, Final Thoughts, and Future Directions

Until now, SAMDI-MS assays have been exclusively carried out in microtiter plates and on spotted arrays. Manual or robotic pipetting was required for all sample handling steps and reactions were analyzed spot-by-spot with a MALDI mass spectrometer. When SAMDI-MS was first introduced, reactions were performed on 50-spotted glass slides. Improvements in liquid handling, substrate preparation, and data acquisition increased the number of spots by 30-fold to 1,536. In this work, I present iSAMDI-MS for the first time, which moves beyond the paradigm of array plates and pipetted droplets. In iSAMDI-MS, the array density is dependent on the pixel resolution of the MALDI mass spectrometer. All imaging experiments in this work were performed on a Bruker Autoflex III MALDI TOF mass spectrometer at 200 μm pixel resolution. At this resolution, one standard 25 mm x 75 mm microscope slide can be used to assay 35,000 reactions− a 20-fold improvement over the 1,536 spot array density. Importantly, a microfluidic device performs all reagent handling steps, reducing the amount of time and material compared to conventional benchtop assays.

This work also presents new techniques for controlling reactions on surfaces. 3D microfluidic devices can precisely manipulate fluid flows before contact with the SAM. The reactions proceed in the fluid flow above the SAM, such that the reaction progress is a measurement of the distance from the location of reagent mixing in the device. The chemically-defined self-assembled monolayers have three major advantages for iSAMDI-MS: 1) they allow excellent pixel-to-pixel reproducibility of the SAMDI-MS spectra, 2) selectively immobilize analytes from the flow above, and 3) the thiol-maleimide immobilization reaction occurs rapidly

(on the order of hundreds M^{-1} s^{-1}) to allow complete immobilization under flow. The SAMs were also important for patterning enzyme binding sites for enabling control over stepwise biochemical reactions in a microfluidic reactor. Microfluidics and SAMs provide the freedom to design, modify, and control reactions in ways unattainable with traditional batch-based processes.

This work represents just the beginning of iSAMDI-MS. The rapifleX MALDI mass spectrometer (Bruker Daltonics) can acquire spectra at 10 μm pixel resolution, such that *18.7 million experiments* can be performed on a standard microscope slide and *85.2 million experiments* can be performed on a standard SAMDI-MS metal plate. MALDI-MS instruments will eventually reach nanometer-scale pixel resolution that will increase throughput and allow for studying intracellular processes and single-molecule DNA, RNA, and protein interactions.

This work also presents the first strategy for overcoming the effect of dispersion in continuous flow devices. Analytes from the fluid front immobilizes onto the floor of the device as the front flows over the SAM; knowledge of the immobilization kinetics and fluid front characteristics allowed us to obtain accurate position-to-time information and calculate kinetic rate constants. Future work using continuous flow devices may apply self-assembled monolayers that ‘turn on’ their ability to immobilize analytes upon application of an external stimulus. For example, the SAM can be functionalized with a photoprotected maleimide that liberates the photoprotecting group upon ultraviolet (UV) illumination. Another option is using a substrate-protected maleimide that becomes enzymatically cleaved to reveal the maleimide functional group. In both strategies, the analyte in the flowing fluid does not bind to the monolayer until the microfluidic device is fully equilibrated and the dispersive regime within the fluid front is no

longer present. Once equilibrated, the applying UV light or injecting enzyme reveals the maleimide functional group and permits analyte binding.

iSAMDI-MS is not limited to continuous flow microfluidic systems. It can be applied to any microfluidic device design as long as the device can be integrated with a chip presenting the SAM. For example, a droplet-based fluidic device can mix reagents into droplets and application of a physical disturbance (i.e. sonication, electric current) opens the droplets, releasing their contents and allowing the previously-contained analytes to immobilize to the SAM. This can be applied to single-cell screening applications to test genetic mutants from large libraries without relying on fluorescent reporters or labels. In this system, single *E.Coli* cells can be sorted in droplets and mixed with isopropyl β-D-1-thiogalactopyranoside (IPTG) to initiate recombinant protein expression. Lysis releases the cell and droplet contents and iSAMDI-MS analyzes the overexpressed enzymatic activity through a reporter peptide present on the SAM. In this way, thousands of enzyme mutants can be screened in high-throughput with minimal reagent consumption, pipetting, and manual labor. This same concept can be applied towards mammalian single-cell profiling to assess heterogeneity in cancer cell populations. In addition, mVLSI devices can be straightforwardly integrated with SAMs for confining reactions into arrayed wells with dimensions equivalent to the 10 μm pixel resolution of the rapifleX.[14]

Much of the work presented here was enabled by a method that I developed for 3D printing PDMS device masters. 3D printing allowed for rapid prototyping of device designs without having to use a cleanroom. Recent developments in 3D printing resins now allow us to print entire devices− obviating the need for PDMS masters and enable constructing 3D fluidic devices without layer-by-layer assembly.[200] Folch and coworkers recently developed a method to

3D print PDMS, which will find great use in biology and chemistry due to its well-known biocompatability.[201] Improvements in printing resolution will soon enable 3D printed microfluidic devices with micro-valves, mixers, and arrays. Continued research in resin development and 3D printer engineering will increase the number of biocompatible and mechanically stable materials available for microfluidic device fabrication.

References

(1) Hong, J.; Edel, J. B.; deMello, A. J. Micro- and Nanofluidic Systems for High-Throughput Biological Screening. *Drug Discovery Today* **2009**, *14* (3), 134–146. https://doi.org/10.1016/j.drudis.2008.10.001.

(2) Englert, D. L.; Manson, M. D.; Jayaraman, A. Flow-Based Microfluidic Device for Quantifying Bacterial Chemotaxis in Stable, Competing Gradients. *Appl Environ Microbiol* **2009**, *75* (13), 4557–4564. https://doi.org/10.1128/AEM.02952-08.

(3) Hong, J.; deMello, A. J.; Jayasinghe, S. N. Bio-Electrospraying and Droplet-Based Microfluidics: Control of Cell Numbers within Living Residues. *Biomed Mater* **2010**, *5* (2), 21001. https://doi.org/10.1088/1748-6041/5/2/021001.

(4) Araci, I. E.; Quake, S. R. Microfluidic Very Large Scale Integration (MVLSI) with Integrated Micromechanical Valves. *Lab Chip* **2012**, *12* (16), 2803–2806. https://doi.org/10.1039/C2LC40258K.

(5) Dertinger, S. K. W.; Chiu, D. T.; Jeon, N. L.; Whitesides, G. M. Generation of Gradients Having Complex Shapes Using Microfluidic Networks. *Anal. Chem.* **2001**, *73* (6), 1240–1246. https://doi.org/10.1021/ac001132d.

(6) Yun, J. Y.; Jambovane, S.; Kim, S.-K.; Cho, S.-H.; Duin, E. C.; Hong, J. W. Log-Scale Dose Response of Inhibitors on a Chip. *Anal. Chem.* **2011**, *83* (16), 6148–6153. https://doi.org/10.1021/ac201177g.

(7) Chang, C.-W.; Cheng, Y.-J.; Tu, M.; Chen, Y.-H.; Peng, C.-C.; Liao, W.-H.; Tung, Y.-C. A Polydimethylsiloxane-Polycarbonate Hybrid Microfluidic Device Capable of Generating Perpendicular Chemical and Oxygen Gradients for Cell Culture Studies. *Lab Chip* **2014**, *14* (19), 3762–3772. https://doi.org/10.1039/c4lc00732h.

(8) Bhattacharjee, N.; Folch, A. Large-Scale Microfluidic Gradient Arrays Reveal Axon Guidance Behaviors in Hippocampal Neurons. *Microsystems & Nanoengineering* **2017**, *3*, 17003. https://doi.org/10.1038/micronano.2017.3.

(9) Kang, D.-K.; Gong, X.; Cho, S.; Kim, J.; Edel, J. B.; Chang, S.-I.; Choo, J.; deMello, A. J. 3D Droplet Microfluidic Systems for High-Throughput Biological Experimentation. *Anal. Chem.* **2015**, *87* (21), 10770–10778. https://doi.org/10.1021/acs.analchem.5b02402.

(10) Li, L.; Ismagilov, R. F. Protein Crystallization Using Microfluidic Technologies Based on Valves, Droplets, and SlipChip. *Annu Rev Biophys* **2010**, *39*, 139–158. https://doi.org/10.1146/annurev.biophys.050708.133630.

(11) Rho, H. S.; Hanke, A. T.; Ottens, M.; Gardeniers, H. Mapping of Enzyme Kinetics on a Microfluidic Device. *PLOS ONE* **2016**, *11* (4), e0153437. https://doi.org/10.1371/journal.pone.0153437.

(12) D. Ahrberg, C.; Manz, A.; Geun Chung, B. Polymerase Chain Reaction in Microfluidic Devices. *Lab on a Chip* **2016**, *16* (20), 3866–3884. https://doi.org/10.1039/C6LC00984K.

(13) Siltanen, C. A.; Cole, R. H.; Poust, S.; Chao, L.; Tyerman, J.; Kaufmann-Malaga, B.; Ubersax, J.; Gartner, Z. J.; Abate, A. R. An Oil-Free Picodrop Bioassay Platform for Synthetic Biology. *Scientific Reports* **2018**, *8* (1), 7913. https://doi.org/10.1038/s41598-018-25577-4.

(14) Araci, I. E.; Quake, S. R. Microfluidic Very Large Scale Integration (MVLSI) with Integrated Micromechanical Valves. *Lab Chip* **2012**, *12* (16), 2803–2806. https://doi.org/10.1039/C2LC40258K.
(15) Au, A. K.; Lai, H.; Utela, B. R.; Folch, A.; Au, A. K.; Lai, H.; Utela, B. R.; Folch, A. Microvalves and Micropumps for BioMEMS. *Micromachines* **2011**, *2* (2), 179–220. https://doi.org/10.3390/mi2020179.
(16) Spurgeon, S. L.; Jones, R. C.; Ramakrishnan, R. High Throughput Gene Expression Measurement with Real Time PCR in a Microfluidic Dynamic Array. *PLOS ONE* **2008**, *3* (2), e1662. https://doi.org/10.1371/journal.pone.0001662.
(17) Chen, S.-Y. C.; Hung, P. J.; Lee, P. J. Microfluidic Array for Three-Dimensional Perfusion Culture of Human Mammary Epithelial Cells. *Biomed Microdevices* **2011**, *13* (4), 753–758. https://doi.org/10.1007/s10544-011-9545-3.
(18) Maerkl, S. J.; Quake, S. R. A Systems Approach to Measuring the Binding Energy Landscapes of Transcription Factors. *Science* **2007**, *315* (5809), 233–237. https://doi.org/10.1126/science.1131007.
(19) Fordyce, P. M.; Gerber, D.; Tran, D.; Zheng, J.; Li, H.; DeRisi, J. L.; Quake, S. R. De Novo Identification and Biophysical Characterization of Transcription Factor Binding Sites with Microfluidic Affinity Analysis. *Nat Biotechnol* **2010**, *28* (9), 970–975. https://doi.org/10.1038/nbt.1675.
(20) Hyman, A. A.; Weber, C. A.; Jülicher, F. Liquid-Liquid Phase Separation in Biology. *Annu. Rev. Cell Dev. Biol.* **2014**, *30* (1), 39–58. https://doi.org/10.1146/annurev-cellbio-100913-013325.
(21) Hyman, A. A.; Brangwynne, C. P. Beyond Stereospecificity: Liquids and Mesoscale Organization of Cytoplasm. *Developmental Cell* **2011**, *21* (1), 14–16. https://doi.org/10.1016/j.devcel.2011.06.013.
(22) Goldstein, R. E.; Meent, J.-W. van de. A Physical Perspective on Cytoplasmic Streaming. *Interface Focus* **2015**, *5* (4), 20150030. https://doi.org/10.1098/rsfs.2015.0030.
(23) Hochachka, P. W. The Metabolic Implications of Intracellular Circulation. *PNAS* **1999**, *96* (22), 12233–12239. https://doi.org/10.1073/pnas.96.22.12233.
(24) Y. Ono, M. Kitajima, S. Daikoku, T. Shiroya, S. Nishihara, Y. Kanie, K. Suzuki, S. Goto, O. Kanie. *Lab Chip* **2008**, *8*, (12), 2168-73. https://doi.org/10.1073/10.1039/b809316d.
(25) Maier, M.; Radtke, C. P.; Hubbuch, J.; Niemeyer, C. M.; Rabe, K. S. On-Demand Production of Flow-Reactor Cartridges by 3D Printing of Thermostable Enzymes. *Angewandte Chemie International Edition* **2018**, *57* (19), 5539–5543. https://doi.org/10.1002/anie.201711072.
(26) Garrett, T. J.; Prieto-Conaway, M. C.; Kovtoun, V.; Bui, H.; Izgarian, N.; Stafford, G.; Yost, R. A. Imaging of Small Molecules in Tissue Sections with a New Intermediate-Pressure MALDI Linear Ion Trap Mass Spectrometer. *International Journal of Mass Spectrometry* **2007**, *260* (2), 166–176. https://doi.org/10.1016/j.ijms.2006.09.019.
(27) Kompauer, M.; Heiles, S.; Spengler, B. Atmospheric Pressure MALDI Mass Spectrometry Imaging of Tissues and Cells at 1.4-Mm Lateral Resolution. *Nature Methods* **2017**, *14* (1), 90–96. https://doi.org/10.1038/nmeth.4071.

(28) Andersson, M.; Groseclose, M. R.; Deutch, A. Y.; Caprioli, R. M. Imaging Mass Spectrometry of Proteins and Peptides: 3D Volume Reconstruction. *Nature Methods* **2008**, *5* (1), 101–108. https://doi.org/10.1038/nmeth1145.
(29) Altelaar, A. F. M.; Taban, I. M.; McDonnell, L. A.; Verhaert, P. D. E. M.; de Lange, R. P. J.; Adan, R. A. H.; Mooi, W. J.; Heeren, R. M. A.; Piersma, S. R. High-Resolution MALDI Imaging Mass Spectrometry Allows Localization of Peptide Distributions at Cellular Length Scales in Pituitary Tissue Sections. *International Journal of Mass Spectrometry* **2007**, *260* (2), 203–211. https://doi.org/10.1016/j.ijms.2006.09.028.
(30) Sinha, T. K.; Khatib-Shahidi, S.; Yankeelov, T. E.; Mapara, K.; Ehtesham, M.; Cornett, D. S.; Dawant, B. M.; Caprioli, R. M.; Gore, J. C. Integrating Spatially Resolved Three-Dimensional MALDI IMS with *in Vivo* Magnetic Resonance Imaging. *Nature Methods* **2008**, *5* (1), 57–59. https://doi.org/10.1038/nmeth1147.
(31) Casadonte, R.; Caprioli, R. M. Proteomic Analysis of Formalin-Fixed Paraffin-Embedded Tissue by MALDI Imaging Mass Spectrometry. *Nat Protoc* **2011**, *6* (11), 1695–1709. https://doi.org/10.1038/nprot.2011.388.
(32) McDonnell Liam A.; Piersma Sander R.; Altelaar A. F. Maarten; Mize Todd H.; Luxembourg Stefan L.; Verhaert Peter D. E. M.; van Minnen Jan; Heeren Ron M. A. Subcellular Imaging Mass Spectrometry of Brain Tissue. *Journal of Mass Spectrometry* **2005**, *40* (2), 160–168. https://doi.org/10.1002/jms.735.
(33) Dueñas, M. E.; Essner, J. J.; Lee, Y. J. 3D MALDI Mass Spectrometry Imaging of a Single Cell: Spatial Mapping of Lipids in the Embryonic Development of Zebrafish. *Scientific Reports* **2017**, *7* (1), 14946. https://doi.org/10.1038/s41598-017-14949-x.
(34) Powers, T. W.; Jones, E. E.; Betesh, L. R.; Romano, P.; Gao, P.; Copland, J. A.; Mehta, A. S.; Drake, R. R. A MALDI Imaging Mass Spectrometry Workflow for Spatial Profiling Analysis of N-Linked Glycan Expression in Tissues. *Anal Chem* **2013**, *85* (20), 9799–9806. https://doi.org/10.1021/ac402108x.
(35) Gemperline, E.; Rawson, S.; Li, L. Optimization and Comparison of Multiple MALDI Matrix Application Methods for Small Molecule Mass Spectrometric Imaging. *Anal. Chem.* **2014**, *86* (20), 10030–10035. https://doi.org/10.1021/ac5028534.
(36) Robichaud, G.; Garrard, K. P.; Barry, J. A.; Muddiman, D. C. MSiReader: An Open-Source Interface to View and Analyze High Resolving Power MS Imaging Files on Matlab Platform. *J. Am. Soc. Mass Spectrom.* **2013**, *24* (5), 718–721. https://doi.org/10.1007/s13361-013-0607-z.
(37) Bokhart, M. T.; Nazari, M.; Garrard, K. P.; Muddiman, D. C. MSiReader v1.0: Evolving Open-Source Mass Spectrometry Imaging Software for Targeted and Untargeted Analyses. *J. Am. Soc. Mass Spectrom.* **2018**, *29* (1), 8–16. https://doi.org/10.1007/s13361-017-1809-6.
(38) Fujimura, Y.; Miura, D.; Fujimura, Y.; Miura, D. MALDI Mass Spectrometry Imaging for Visualizing In Situ Metabolism of Endogenous Metabolites and Dietary Phytochemicals. *Metabolites* **2014**, *4* (2), 319–346. https://doi.org/10.3390/metabo4020319.
(39) Zavalin, A.; Yang, J.; Hayden, K.; Vestal, M.; Caprioli, R. M. Tissue Protein Imaging at 1 Mm Laser Spot Diameter for High Spatial Resolution and High Imaging Speed Using Transmission Geometry MALDI TOF MS. *Anal Bioanal Chem* **2015**, *407* (8), 2337–2342. https://doi.org/10.1007/s00216-015-8532-6.

(40) Houseman, B. T.; Gawalt, E. S.; Mrksich, M. Maleimide-Functionalized Self-Assembled Monolayers for the Preparation of Peptide and Carbohydrate Biochips. *Langmuir* **2003**, *19* (5), 1522–1531. https://doi.org/10.1021/la0262304.
(41) Houseman, B. T.; Mrksich, M. Carbohydrate Arrays for the Evaluation of Protein Binding and Enzymatic Modification. *Chemistry & Biology* **2002**, *9* (4), 443–454. https://doi.org/10.1016/S1074-5521(02)00124-2.
(42) Helal, K. Y.; Alamgir, A.; Berns, E. J.; Mrksich, M. Traceless Immobilization of Analytes for High-Throughput Experiments with SAMDI Mass Spectrometry. *J. Am. Chem. Soc.* **2018**, *140* (26), 8060–8063. https://doi.org/10.1021/jacs.8b02918.
(43) Hodneland, C. D.; Lee, Y.-S.; Min, D.-H.; Mrksich, M. Selective Immobilization of Proteins to Self-Assembled Monolayers Presenting Active Site-Directed Capture Ligands. *Proc. Natl. Acad. Sci. U.S.A.* **2002**, *99* (8), 5048–5052. https://doi.org/10.1073/pnas.072685299.
(44) Grant, J.; Modica, J. A.; Roll, J.; Perkovich, P.; Mrksich, M. An Immobilized Enzyme Reactor for Spatiotemporal Control over Reaction Products. *Small* **2018**, *14* (31), 1800923. https://doi.org/10.1002/smll.201800923.
(45) Szymczak, L. C.; Kuo, H.-Y.; Mrksich, M. Peptide Arrays: Development and Application. *Anal. Chem.* **2018**, *90* (1), 266–282. https://doi.org/10.1021/acs.analchem.7b04380.
(46) Gurard-Levin, Z. A.; Mrksich, M. The Activity of HDAC8 Depends on Local and Distal Sequences of Its Peptide Substrates. *Biochemistry* **2008**, *47* (23), 6242–6250. https://doi.org/10.1021/bi800053v.
(47) Diagne, A. B.; Li, S.; Perkowski, G. A.; Mrksich, M.; Thomson, R. J. SAMDI Mass Spectrometry-Enabled High-Throughput Optimization of a Traceless Petasis Reaction. *ACS Comb. Sci.* **2015**, *17* (11), 658–662. https://doi.org/10.1021/acscombsci.5b00131.
(48) Kuo, H.-Y.; DeLuca, T. A.; Miller, W. M.; Mrksich, M. Profiling Deacetylase Activities in Cell Lysates with Peptide Arrays and SAMDI Mass Spectrometry. *Anal Chem* **2013**, *85* (22), 10635–10642. https://doi.org/10.1021/ac402614x.
(49) O'Kane, P. T.; Mrksich, M. An Assay Based on SAMDI Mass Spectrometry for Profiling Protein Interaction Domains. *J. Am. Chem. Soc.* **2017**, *139* (30), 10320–10327. https://doi.org/10.1021/jacs.7b03805.
(50) Gurard-Levin, Z. A.; Scholle, M. D.; Eisenberg, A. H.; Mrksich, M. High-Throughput Screening of Small Molecule Libraries Using SAMDI Mass Spectrometry. *ACS Comb Sci* **2011**, *13* (4), 347–350. https://doi.org/10.1021/co2000373.
(51) Cabezas, M. D.; Mirkin, C. A.; Mrksich, M. Nanopatterned Extracellular Matrices Enable Cell-Based Assays with a Mass Spectrometric Readout. *Nano Lett.* **2017**, *17* (3), 1373–1377. https://doi.org/10.1021/acs.nanolett.6b04176.
(52) Berns, E. J.; Cabezas, M. D.; Mrksich, M. Cellular Assays with a Molecular Endpoint Measured by SAMDI Mass Spectrometry. *Small* **2016**, *12* (28), 3811–3818. https://doi.org/10.1002/smll.201502940.
(53) Kornacki, J. R.; Stuparu, A. D.; Mrksich, M. Acetyltransferase P300/CBP Associated Factor (PCAF) Regulates Crosstalk-Dependent Acetylation of Histone H3 by Distal Site Recognition. *ACS Chem. Biol.* **2015**, *10* (1), 157–164. https://doi.org/10.1021/cb5004527.

(54) Cao, Z.; Chen, C.; He, B.; Tan, K.; Lu, C. A Microfluidic Device for Epigenomic Profiling Using 100 Cells. *Nature Methods* **2015**, *12* (10), 959–962. https://doi.org/10.1038/nmeth.3488.
(55) Deshpande, S.; Dekker, C. On-Chip Microfluidic Production of Cell-Sized Liposomes. *Nature Protocols* **2018**, *13* (5), 856–874. https://doi.org/10.1038/nprot.2017.160.
(56) Neils, C.; Tyree, Z.; Finlayson, B.; Folch, A. Combinatorial Mixing of Microfluidic Streams. *Lab Chip* **2004**, *4* (4), 342–350. https://doi.org/10.1039/b314962e.
(57) Kang, D.-K.; Gong, X.; Cho, S.; Kim, J.; Edel, J. B.; Chang, S.-I.; Choo, J.; deMello, A. J. 3D Droplet Microfluidic Systems for High-Throughput Biological Experimentation. *Anal. Chem.* **2015**, *87* (21), 10770–10778. https://doi.org/10.1021/acs.analchem.5b02402.
(58) Thorsen, T.; Maerkl, S. J.; Quake, S. R. Microfluidic Large-Scale Integration. *Science* **2002**, *298* (5593), 580–584. https://doi.org/10.1126/science.1076996.
(59) Zheng, B.; Roach, L. S.; Ismagilov, R. F. Screening of Protein Crystallization Conditions on a Microfluidic Chip Using Nanoliter-Size Droplets. *J. Am. Chem. Soc.* **2003**, *125* (37), 11170–11171. https://doi.org/10.1021/ja037166v.
(60) Q. Boedicker, J.; Li, L.; R. Kline, T.; F. Ismagilov, R. Detecting Bacteria and Determining Their Susceptibility to Antibiotics by Stochastic Confinement in Nanoliter Droplets Using Plug-Based Microfluidics. *Lab on a Chip* **2008**, *8* (8), 1265–1272. https://doi.org/10.1039/B804911D.
(61) Hatakeyama, T.; Chen, D. L.; Ismagilov, R. F. Microgram-Scale Testing of Reaction Conditions in Solution Using Nanoliter Plugs in Microfluidics with Detection by MALDI-MS. *J. Am. Chem. Soc.* **2006**, *128* (8), 2518–2519. https://doi.org/10.1021/ja057720w.
(62) Jeon, N. L.; Dertinger, S. K. W.; Chiu, D. T.; Choi, I. S.; Stroock, A. D.; Whitesides, G. M. Generation of Solution and Surface Gradients Using Microfluidic Systems. *Langmuir* **2000**, *16* (22), 8311–8316. https://doi.org/10.1021/la000600b.
(63) Oh, K. W.; Lee, K.; Ahn, B.; Furlani, E. P. Design of Pressure-Driven Microfluidic Networks Using Electric Circuit Analogy. *Lab Chip* **2012**, *12* (3), 515–545. https://doi.org/10.1039/C2LC20799K.
(64) Cornett, D. S.; Reyzer, M. L.; Chaurand, P.; Caprioli, R. M. MALDI Imaging Mass Spectrometry: Molecular Snapshots of Biochemical Systems. *Nature Methods* **2007**, *4* (10), 828–833. https://doi.org/10.1038/nmeth1094.
(65) Bokhart, M. T.; Nazari, M.; Garrard, K. P.; Muddiman, D. C. MSiReader v1.0: Evolving Open-Source Mass Spectrometry Imaging Software for Targeted and Untargeted Analyses. *J. Am. Soc. Mass Spectrom.* **2018**, *29* (1), 8–16. https://doi.org/10.1007/s13361-017-1809-6.
(66) Robichaud, G.; Garrard, K. P.; Barry, J. A.; Muddiman, D. C. MSiReader: An Open-Source Interface to View and Analyze High Resolving Power MS Imaging Files on Matlab Platform. *J. Am. Soc. Mass Spectrom.* **2013**, *24* (5), 718–721. https://doi.org/10.1007/s13361-013-0607-z.
(67) Henderson, G. B.; Murgolo, N. J.; Kuriyan, J.; Osapay, K.; Kominos, D.; Berry, A.; Scrutton, N. S.; Hinchliffe, N. W.; Perham, R. N.; Cerami, A. Engineering the Substrate Specificity of Glutathione Reductase toward That of Trypanothione Reduction. *Proc Natl Acad Sci U S A* **1991**, *88* (19), 8769–8773.

(68) Becker Katja; Gui Ming; Schirmer R. Heiner. Inhibition of Human Glutathione Reductase by S-nitrosoglutathione. *European Journal of Biochemistry* **2004**, *234* (2), 472–478. https://doi.org/10.1111/j.1432-1033.1995.472_b.x.
(69) Savvides, S. N.; Karplus, P. A. Kinetics and Crystallographic Analysis of Human Glutathione Reductase in Complex with a Xanthene Inhibitor. *J. Biol. Chem.* **1996**, *271* (14), 8101–8107.
(70) Nichols, K. P.; Azoz, S.; Gardeniers, H. J. G. E. Enzyme Kinetics by Directly Imaging a Porous Silicon Microfluidic Reactor Using Desorption/Ionization on Silicon Mass Spectrometry. *Anal. Chem.* **2008**, *80* (21), 8314–8319. https://doi.org/10.1021/ac8017586.
(71) Zavalin, A.; Yang, J.; Hayden, K.; Vestal, M.; Caprioli, R. M. Tissue Protein Imaging at 1 Mm Laser Spot Diameter for High Spatial Resolution and High Imaging Speed Using Transmission Geometry MALDI TOF MS. *Anal Bioanal Chem* **2015**, *407* (8), 2337–2342. https://doi.org/10.1007/s00216-015-8532-6.
(72) Sengupta, S.; Dey, K. K.; Muddana, H. S.; Tabouillot, T.; Ibele, M. E.; Butler, P. J.; Sen, A. Enzyme Molecules as Nanomotors. *J. Am. Chem. Soc.* **2013**, *135* (4), 1406–1414. https://doi.org/10.1021/ja3091615.
(73) Araci, I. E.; Quake, S. R. Microfluidic Very Large Scale Integration (MVLSI) with Integrated Micromechanical Valves. *Lab Chip* **2012**, *12* (16), 2803–2806. https://doi.org/10.1039/C2LC40258K.
(74) Dillmore, W. S.; Yousaf, M. N.; Mrksich, M. A Photochemical Method for Patterning the Immobilization of Ligands and Cells to Self-Assembled Monolayers. *Langmuir* **2004**, *20* (17), 7223–7231. https://doi.org/10.1021/la049826v.
(75) Yeo, W. S.; Mrksich, M. Electroactive Substrates That Reveal Aldehyde Groups for Bio-Immobilization. *Advanced Materials 16* (15), 1352–1356. https://doi.org/10.1002/adma.200400591.
(76) Helal, K. Y.; Alamgir, A.; Berns, E. J.; Mrksich, M. Traceless Immobilization of Analytes for High-Throughput Experiments with SAMDI Mass Spectrometry. *J. Am. Chem. Soc.* **2018**, *140* (26), 8060–8063. https://doi.org/10.1021/jacs.8b02918.
(77) Wood, S. E.; Sinsinbar, G.; Gudlur, S.; Nallani, M.; Huang, C.-F.; Liedberg, B.; Mrksich, M. A Bottom-Up Proteomic Approach to Identify Substrate Specificity of Outer-Membrane Protease OmpT. *Angew. Chem. Int. Ed. Engl.* **2017**, *56* (52), 16531–16535. https://doi.org/10.1002/anie.201707535.
(78) Stenzel, M. H. Bioconjugation Using Thiols: Old Chemistry Rediscovered to Connect Polymers with Nature's Building Blocks. *ACS Macro Lett.* **2013**, *2* (1), 14–18. https://doi.org/10.1021/mz3005814.
(79) Datta, S.; Ghosal, S. Characterizing Dispersion in Microfluidic Channels. *Lab Chip* **2009**, *9* (17), 2537–2550. https://doi.org/10.1039/b822948c.
(80) Song, H.; Chen, D. L.; Ismagilov, R. F. Reactions in Droplets in Microfluidic Channels. *Angewandte Chemie International Edition* **2006**, *45* (44), 7336–7356. https://doi.org/10.1002/anie.200601554.
(81) Chen, D.; Du, W.; Liu, Y.; Liu, W.; Kuznetsov, A.; Mendez, F. E.; Philipson, L. H.; Ismagilov, R. F. The Chemistrode: A Droplet-Based Microfluidic Device for Stimulation and Recording with High Temporal, Spatial, and Chemical Resolution. *Proc Natl Acad Sci U S A* **2008**, *105* (44), 16843–16848. https://doi.org/10.1073/pnas.0807916105.

(82) Song, H.; Tice, J. D.; Ismagilov, R. F. A Microfluidic System for Controlling Reaction Networks in Time. *Angewandte Chemie International Edition* **2003**, *42* (7), 768–772. https://doi.org/10.1002/anie.200390203.
(83) Huebner, A. M.; Abell, C.; Huck, W. T. S.; Baroud, C. N.; Hollfelder, F. Monitoring a Reaction at Submillisecond Resolution in Picoliter Volumes. *Anal. Chem.* **2011**, *83* (4), 1462–1468. https://doi.org/10.1021/ac103234a.
(84) Mao, H.; Yang, T.; Cremer, P. S. A Microfluidic Device with a Linear Temperature Gradient for Parallel and Combinatorial Measurements. *J. Am. Chem. Soc.* **2002**, *124* (16), 4432–4435. https://doi.org/10.1021/ja017625x.
(85) Fidalgo, L. M.; Whyte, G.; Ruotolo, B. T.; Benesch, J. L. P.; Stengel, F.; Abell, C.; Robinson, C. V.; Huck, W. T. S. Coupling Microdroplet Microreactors with Mass Spectrometry: Reading the Contents of Single Droplets Online. *Angew. Chem. Int. Ed. Engl.* **2009**, *48* (20), 3665–3668. https://doi.org/10.1002/anie.200806103.
(86) Wang, J.; Sui, G.; Mocharla, V. P.; Lin, R. J.; Phelps, M. E.; Kolb, H. C.; Tseng, H.-R. Integrated Microfluidics for Parallel Screening of an In Situ Click Chemistry Library. *Angewandte Chemie International Edition 45* (32), 5276–5281. https://doi.org/10.1002/anie.200601677.
(87) Browne, D. L.; Wright, S.; Deadman, B. J.; Dunnage, S.; Baxendale, I. R.; Turner, R. M.; Ley, S. V. Continuous Flow Reaction Monitoring Using an On-Line Miniature Mass Spectrometer. *Rapid Communications in Mass Spectrometry 26* (17), 1999–2010. https://doi.org/10.1002/rcm.6312.
(88) Liu, Y.; Ismagilov, R. F. Dynamics of Coalescence of Plugs with a Hydrophilic Wetting Layer Induced by Flow in a Microfluidic Chemistrode. *Langmuir* **2009**, *25* (5), 2854–2859. https://doi.org/10.1021/la803518b.
(89) Hatakeyama, T.; Chen, D. L.; Ismagilov, R. F. Microgram-Scale Testing of Reaction Conditions in Solution Using Nanoliter Plugs in Microfluidics with Detection by MALDI-MS. *J. Am. Chem. Soc.* **2006**, *128* (8), 2518–2519. https://doi.org/10.1021/ja057720w.
(90) Bula, W. P.; Verboom, W.; Reinhoudt, D. N.; Gardeniers, H. J. G. E. Multichannel Quench-Flow Microreactor Chip for Parallel Reaction Monitoring. *Lab Chip* **2007**, *7* (12), 1717–1722. https://doi.org/10.1039/B710680G.
(91) Houseman, B. T.; Gawalt, E. S.; Mrksich, M. Maleimide-Functionalized Self-Assembled Monolayers for the Preparation of Peptide and Carbohydrate Biochips. *Langmuir* **2003**, *19* (5), 1522–1531. https://doi.org/10.1021/la0262304.
(92) Weber, A. L. Formation of the Thioester, N-Acetyl, S-Lactoylcysteine, by Reaction of N-Acetylcysteine with Pyruvaldehyde in Aqueous Solution. *J Mol Evol* **1982**, *18* (5), 354–359. https://doi.org/10.1007/BF01733903.
(93) Okuyama, T.; Komoguchi, S.; Fueno, T. Reaction of Thiols with Phenylglyoxal to Give Thiol Esters of Mandelic Acid. II. Intramolecular General-Base Catalysis and Change in Rate-Determining Step. *J. Am. Chem. Soc.* **1982**, *104* (9), 2582–2587. https://doi.org/10.1021/ja00373a041.
(94) Dawson, P. E.; Muir, T. W.; Clark-Lewis, I.; Kent, S. B. Synthesis of Proteins by Native Chemical Ligation. *Science* **1994**, *266* (5186), 776–779. https://doi.org/10.1126/science.7973629.

(95) Grant, J.; Goudarzi, S. H.; Mrksich, M. High-Throughput Enzyme Kinetics with 3D Microfluidics and Imaging SAMDI Mass Spectrometry. *Anal. Chem.* **2018**. https://doi.org/10.1021/acs.analchem.8b04391.
(96) Liao, X.; Su, J.; Mrksich, M. An Adaptor Domain-Mediated Autocatalytic Interfacial Kinase Reaction. *Chemistry – A European Journal* **2009**, *15* (45), 12303–12309. https://doi.org/10.1002/chem.200901345.
(97) Pollock, S. B.; Kent, S. B. H. An Investigation into the Origin of the Dramatically Reduced Reactivity of Peptide-Prolyl-Thioesters in Native Chemical Ligation. *Chem. Commun.* **2011**, *47* (8), 2342–2344. https://doi.org/10.1039/C0CC04120C.
(98) Chen, D.; Disotuar, M. M.; Xiong, X.; Wang, Y.; Chou, D. H.-C. Selective N-Terminal Functionalization of Native Peptides and Proteins. *Chem. Sci.* **2017**, *8* (4), 2717–2722. https://doi.org/10.1039/C6SC04744K.
(99) Britto, P. J.; Knipling, L.; Wolff, J. The Local Electrostatic Environment Determines Cysteine Reactivity of Tubulin. *J. Biol. Chem.* **2002**, *277* (32), 29018–29027. https://doi.org/10.1074/jbc.M204263200.
(100) Song, H.; Chen, D. L.; Ismagilov, R. F. Reactions in Droplets in Microfluidic Channels. *Angew Chem Int Ed Engl* **2006**, *45* (44), 7336–7356. https://doi.org/10.1002/anie.200601554.
(101) Mark, D.; Haeberle, S.; Roth, G.; Stetten, F. von; Zengerle, R. Microfluidic Lab-on-a-Chip Platforms: Requirements, Characteristics and Applications. *Chemical Society Reviews* **2010**, *39* (3), 1153–1182. https://doi.org/10.1039/B820557B.
(102) Yousaf, M. N.; Mrksich, M. Diels−Alder Reaction for the Selective Immobilization of Protein to Electroactive Self-Assembled Monolayers. *J. Am. Chem. Soc.* **1999**, *121* (17), 4286–4287. https://doi.org/10.1021/ja983529t.
(103) Ban, L.; Pettit, N.; Li, L.; Stuparu, A. D.; Cai, L.; Chen, W.; Guan, W.; Han, W.; Wang, P. G.; Mrksich, M. Discovery of Glycosyltransferases Using Carbohydrate Arrays and Mass Spectrometry. *Nat Chem Biol* **2012**, *8* (9), 769–773. https://doi.org/10.1038/nchembio.1022.
(104) Ban, L.; Mrksich, M. On-Chip Synthesis and Label-Free Assays of Oligosaccharide Arrays. *Angewandte Chemie* **2008**, *120* (18), 3444–3447. https://doi.org/10.1002/ange.200704998.
(105) Wollman, E. W.; Kang, D.; Frisbie, C. D.; Lorkovic, I. M.; Wrighton, M. S. Photosensitive Self-Assembled Monolayers on Gold: Photochemistry of Surface-Confined Aryl Azide and Cyclopentadienylmanganese Tricarbonyl. *J. Am. Chem. Soc.* **1994**, *116* (10), 4395–4404. https://doi.org/10.1021/ja00089a030.
(106) Chechik, V.; Crooks, R. M.; Stirling, C. J. M. Reactions and Reactivity in Self-Assembled Monolayers. *Advanced Materials* **2000**, *12* (16), 1161–1171. https://doi.org/10.1002/1521-4095(200008)12:16<1161::AID-ADMA1161>3.0.CO;2-C.
(107) Diagne, A. B.; Li, S.; Perkowski, G. A.; Mrksich, M.; Thomson, R. J. SAMDI Mass Spectrometry-Enabled High-Throughput Optimization of a Traceless Petasis Reaction. *ACS Comb. Sci.* **2015**, *17* (11), 658–662. https://doi.org/10.1021/acscombsci.5b00131.
(108) Helal, K. Y.; Alamgir, A.; Berns, E. J.; Mrksich, M. Traceless Immobilization of Analytes for High-Throughput Experiments with SAMDI Mass Spectrometry. *J. Am. Chem. Soc.* **2018**, *140* (26), 8060–8063. https://doi.org/10.1021/jacs.8b02918.

(109) Tyagi, S.; VanDelinder, V.; Banterle, N.; Fuertes, G.; Milles, S.; Agez, M.; Lemke, E. A. Continuous Throughput and Long-Term Observation of Single-Molecule FRET without Immobilization. *Nature Methods* **2014**, *11* (3), 297–300. https://doi.org/10.1038/nmeth.2809.

(110) Bouilly, D.; Hon, J.; Daly, N. S.; Trocchia, S.; Vernick, S.; Yu, J.; Warren, S.; Wu, Y.; Gonzalez, R. L.; Shepard, K. L.; et al. Single-Molecule Reaction Chemistry in Patterned Nanowells. *Nano Lett.* **2016**, *16* (7), 4679–4685. https://doi.org/10.1021/acs.nanolett.6b02149.

(111) Casadonte, R.; Caprioli, R. M. Proteomic Analysis of Formalin-Fixed Paraffin-Embedded Tissue by MALDI Imaging Mass Spectrometry. *Nature Protocols* **2011**, *6* (11), 1695–1709. https://doi.org/10.1038/nprot.2011.388.

(112) Fogler, H. S. *Essentials of Chemical Reaction Engineering: Essenti Chemica Reactio Engi*; Pearson Education, 2010.

(113) Kwon, Y.; Mrksich, M. Dependence of the Rate of an Interfacial Diels−Alder Reaction on the Steric Environment of the Immobilized Dienophile: An Example of Enthalpy−Entropy Compensation. *J. Am. Chem. Soc.* **2002**, *124* (5), 806–812. https://doi.org/10.1021/ja010740n.

(114)Abu-Reesh, I. M.; Abu-Sharkh, B. F. Comparison of Axial Dispersion and Tanks-in-Series Models for Simulating the Performance of Enzyme Reactors. *Ind. Eng. Chem. Res.* **2003**, *42* (22), 5495–5505. https://doi.org/10.1021/ie030131j.

(115) Bošković, D.; Loebbecke, S.; Gross, G. A.; Koehler, J. M. Residence Time Distribution Studies in Microfluidic Mixing Structures. *Chemical Engineering & Technology* **2011**, *34* (3), 361–370. https://doi.org/10.1002/ceat.201000352.

(116) Gervais, T.; Jensen, K. F. Mass Transport and Surface Reactions in Microfluidic Systems. *Chemical Engineering Science* **2006**, *61* (4), 1102–1121. https://doi.org/10.1016/j.ces.2005.06.024.

(117) Fernandes del Pozo, D. Effect of Mass Transfer Limitations on Enzymatic Reactions in Microreactors: A Model-Based Analysis. Masters, University of Ghent, 2015.

(118) Slade, D. J.; Fang, P.; Dreyton, C. J.; Zhang, Y.; Fuhrmann, J.; Rempel, D.; Bax, B. D.; Coonrod, S. A.; Lewis, H. D.; Guo, M.; et al. Protein Arginine Deiminase 2 Binds Calcium in an Ordered Fashion: Implications for Inhibitor Design. *ACS Chem. Biol.* **2015**, *10* (4), 1043–1053. https://doi.org/10.1021/cb500933j.

(119) Brown, A. Analysis of Cooperativity by Isothermal Titration Calorimetry. *Int J Mol Sci* **2009**, *10* (8), 3457–3477. https://doi.org/10.3390/ijms10083457.

(120) Rossi, A. M.; Taylor, C. W. Analysis of Protein-Ligand Interactions by Fluorescence Polarization. *Nat Protoc* **2011**, *6* (3), 365–387. https://doi.org/10.1038/nprot.2011.305.

(121) Braun, D. C.; Garfield, S. H.; Blumberg, P. M. Analysis by Fluorescence Resonance Energy Transfer of the Interaction between Ligands and Protein Kinase Cδ in the Intact Cell. *J. Biol. Chem.* **2005**, *280* (9), 8164–8171. https://doi.org/10.1074/jbc.M413896200.

(122) Jecklin, M. C.; Schauer, S.; Dumelin, C. E.; Zenobi, R. Label-Free Determination of Protein–Ligand Binding Constants Using Mass Spectrometry and Validation Using Surface Plasmon Resonance and Isothermal Titration Calorimetry. *Journal of Molecular Recognition 22* (4), 319–329. https://doi.org/10.1002/jmr.951.

(123) Herling, T. W.; O'Connell, D. J.; Bauer, M. C.; Persson, J.; Weininger, U.; Knowles, T. P. J.; Linse, S. A Microfluidic Platform for Real-Time Detection and Quantification of Protein-Ligand Interactions. *Biophys. J.* **2016**, *110* (9), 1957–1966. https://doi.org/10.1016/j.bpj.2016.03.038.

(124) Damgaard, D.; Senolt, L.; Nielsen, C. H. Increased Levels of Peptidylarginine Deiminase 2 in Synovial Fluid from Anti-CCP-Positive Rheumatoid Arthritis Patients: Association with Disease Activity and Inflammatory Markers. *Rheumatology (Oxford)* **2016**, *55* (5), 918–927. https://doi.org/10.1093/rheumatology/kev440.

(125) Bonilha, V. L.; Shadrach, K. G.; Rayborn, M. E.; Li, Y.; Pauer, G. J. T.; Hagstrom, S. A.; Bhattacharya, S. K.; Hollyfield, J. G. Retinal Deimination and PAD2 Levels in Retinas from Donors with Age-Related Macular Degeneration (AMD). *Exp. Eye Res.* **2013**, *111*, 71–78. https://doi.org/10.1016/j.exer.2013.03.017.

(126) Darrah, E.; Rosen, A.; Giles, J. T.; Andrade, F. Peptidylarginine Deiminase 2, 3 and 4 Have Distinct Specificities against Cellular Substrates: Novel Insights into Autoantigen Selection in Rheumatoid Arthritis. *Ann Rheum Dis* **2012**, *71* (1), 92–98. https://doi.org/10.1136/ard.2011.151712.

(127) Slade, D. J.; Fang, P.; Dreyton, C. J.; Zhang, Y.; Fuhrmann, J.; Rempel, D.; Bax, B. D.; Coonrod, S. A.; Lewis, H. D.; Guo, M.; et al. Protein Arginine Deiminase 2 Binds Calcium in an Ordered Fashion: Implications for Inhibitor Design. *ACS Chem. Biol.* **2015**, *10* (4), 1043–1053. https://doi.org/10.1021/cb500933j.

(128) Knipp, M.; Vasák, M. A Colorimetric 96-Well Microtiter Plate Assay for the Determination of Enzymatically Formed Citrulline. *Anal. Biochem.* **2000**, *286* (2), 257–264. https://doi.org/10.1006/abio.2000.4805.

(129) Fert-Bober, J.; Giles, J. T.; Holewinski, R. J.; Kirk, J. A.; Uhrigshardt, H.; Crowgey, E. L.; Andrade, F.; Bingham, C. O.; Park, J. K.; Halushka, M. K.; et al. Citrullination of Myofilament Proteins in Heart Failure. *Cardiovasc. Res.* **2015**, *108* (2), 232–242. https://doi.org/10.1093/cvr/cvv185.

(130) Clancy, K. W.; Weerapana, E.; Thompson, P. R. Detection and Identification of Protein Citrullination in Complex Biological Systems. *Curr Opin Chem Biol* **2016**, *30*, 1–6. https://doi.org/10.1016/j.cbpa.2015.10.014.

(131) Moelants, E. A. V.; Van Damme, J.; Proost, P. Detection and Quantification of Citrullinated Chemokines. *PLoS ONE* **2011**, *6* (12), e28976. https://doi.org/10.1371/journal.pone.0028976.

(132) Choi, M.; Song, J.-S.; Kim, H.-J.; Cha, S.; Lee, E. Y. Matrix-Assisted Laser Desorption Ionization-Time of Flight Mass Spectrometry Identification of Peptide Citrullination Site Using Br Signature. *Anal. Biochem.* **2013**, *437* (1), 62–67. https://doi.org/10.1016/j.ab.2013.03.003.

(133) Bicker, K. L.; Subramanian, V.; Chumanevich, A. A.; Hofseth, L. J.; Thompson, P. R. Seeing Citrulline: Development of a Phenylglyoxal-Based Probe to Visualize Protein Citrullination. *J Am Chem Soc* **2012**, *134* (41), 17015–17018. https://doi.org/10.1021/ja308871v.

(134) Holm, A.; Rise, F.; Sessler, N.; Sollid, L. M.; Undheim, K.; Fleckenstein, B. Specific Modification of Peptide-Bound Citrulline Residues. *Anal. Biochem.* **2006**, *352* (1), 68–76. https://doi.org/10.1016/j.ab.2006.02.007.

(135) Wildeman, E.; Pires, M. M. Facile Fluorescence-Based Detection of PAD4-Mediated Citrullination. *ChemBioChem 14* (8), 963–967. https://doi.org/10.1002/cbic.201300173.
(136) Robinson, R. A.; Chia, C. L. The Diffusion Coefficient of Calcium Chloride in Aqueous Solution at 25°. *J. Am. Chem. Soc.* **1952**, *74* (11), 2776–2777. https://doi.org/10.1021/ja01131a021.
(137) Young, M. E.; Carroad, P. A.; Bell, R. L. Estimation of Diffusion Coefficients of Proteins. *Biotechnology and Bioengineering 22* (5), 947–955. https://doi.org/10.1002/bit.260220504.
(138) Liu, Y.-L.; Chiang, Y.-H.; Liu, G.-Y.; Hung, H.-C. Functional Role of Dimerization of Human Peptidylarginine Deiminase 4 (PAD4). *PLOS ONE* **2011**, *6* (6), e21314. https://doi.org/10.1371/journal.pone.0021314.
(139) Dreyton, C. J.; Knuckley, B.; Jones, J. E.; Lewallen, D. M.; Thompson, P. R. Mechanistic Studies of Protein Arginine Deiminase 2: Evidence for a Substrate-Assisted Mechanism. *Biochemistry* **2014**, *53* (27), 4426–4433. https://doi.org/10.1021/bi500554b.
(140) Chakraborty, P.; Acquasaliente, L.; Pelc, L. A.; Cera, E. D. Interplay between Conformational Selection and Zymogen Activation. *Scientific Reports* **2018**, *8* (1), 4080. https://doi.org/10.1038/s41598-018-21728-9.
(141) Hall, B. E.; Bar-Sagi, D.; Nassar, N. The Structural Basis for the Transition from Ras-GTP to Ras-GDP. *Proc Natl Acad Sci U S A* **2002**, *99* (19), 12138–12142. https://doi.org/10.1073/pnas.192453199.
(142) Peri-Naor, R.; Ilani, T.; Motiei, L.; Margulies, D. Protein–Protein Communication and Enzyme Activation Mediated by a Synthetic Chemical Transducer. *J. Am. Chem. Soc.* **2015**, *137* (30), 9507–9510. https://doi.org/10.1021/jacs.5b01123.
(143) Graham, T. R.; Emr, S. D. Compartmental Organization of Golgi-Specific Protein Modification and Vacuolar Protein Sorting Events Defined in a Yeast Sec18 (NSF) Mutant. *J. Cell Biol.* **1991**, *114* (2), 207–218.
(144) Dunphy, W. G.; Rothman, J. E. Compartmental Organization of the Golgi Stack. *Cell* **1985**, *42* (1), 13–21. https://doi.org/10.1016/S0092-8674(85)80097-0.
(145) Jia, F.; Narasimhan, B.; Mallapragada, S. Materials-Based Strategies for Multi-Enzyme Immobilization and Co-Localization: A Review. *Biotechnology and Bioengineering* **2014** *111* (2), 209–222. https://doi.org/10.1002/bit.25136.
(146) Betancor, L.; Luckarift, H. Co-Immobilized Coupled Enzyme Systems in Biotechnology. *Biotechnol. Genet. Eng. Rev.* **2010**, *27*, 95–114.
(147) Rabe, K. S.; Müller, J.; Skoupi, M.; Niemeyer, C. M. Cascades in Compartments: En Route to Machine-Assisted Biotechnology. *Angewandte Chemie International Edition* **2017**, *56* (44), 13574–13589. https://doi.org/10.1002/anie.201703806.
(148) Heintz, S.; Mitic, A.; Ringborg, R. H.; Krühne, U.; Woodley, J. M.; Gernaey, K. V. A Microfluidic Toolbox for the Development of In-Situ Product Removal Strategies in Biocatalysis. *J Flow Chem* **2016**, *6* (1), 18–26. https://doi.org/10.1556/1846.2015.00040.
(149)Halim, A. A.; Szita, N.; Baganz, F. Characterization and Multi-Step Transketolase-ω-Transaminase Bioconversions in an Immobilized Enzyme Microreactor (IEMR) with Packed Tube. *J. Biotechnol.* **2013**, *168* (4), 567–575. https://doi.org/10.1016/j.jbiotec.2013.09.001.

(150) Boehm, C. R.; Freemont, P. S.; Ces, O. Design of a Prototype Flow Microreactor for Synthetic Biology in Vitro. *Lab Chip* **2013**, *13* (17), 3426–3432. https://doi.org/10.1039/C3LC50231G.
(151) Mukai, C.; Gao, L.; Nelson, J. L.; Lata, J. P.; Cohen, R.; Wu, L.; Hinchman, M. M.; Bergkvist, M.; Sherwood, R. W.; Zhang, S.; et al. Biomimicry Promotes the Efficiency of a 10-Step Sequential Enzymatic Reaction on Nanoparticles, Converting Glucose to Lactate. *Angew Chem Int Ed Engl* **2017**, *56* (1), 235–238. https://doi.org/10.1002/anie.201609495.
(152) Ono, Y.; Kitajima, M.; Daikoku, S.; Shiroya, T.; Nishihara, S.; Kanie, Y.; Suzuki, K.; Goto, S.; Kanie, O. Sequential Enzymatic Glycosyltransfer Reactions on a Microfluidic Device: Synthesis of a Glycosaminoglycan Linkage Region Tetrasaccharide. *Lab Chip* **2008**, *8* (12), 2168–2173. https://doi.org/10.1039/b809316d.
(153) Fornera, S.; Kuhn, P.; Lombardi, D.; Schlüter, A. D.; Dittrich, P. S.; Walde, P. Sequential Immobilization of Enzymes in Microfluidic Channels for Cascade Reactions. *ChemPlusChem* **2012**, *77* (2), 98–101. https://doi.org/10.1002/cplu.201100068.
(154) Peschke, T.; Skoupi, M.; Burgahn, T.; Gallus, S.; Ahmed, I.; Rabe, K. S.; Niemeyer, C. M. Self-Immobilizing Fusion Enzymes for Compartmentalized Biocatalysis. *ACS Catal.* **2017**, *7* (11), 7866–7872. https://doi.org/10.1021/acscatal.7b02230.
(155) Schröder, H.; Hoffmann, L.; Müller, J.; Alhorn, P.; Fleger, M.; Neyer, A.; Niemeyer, C. M. Addressable Microfluidic Polymer Chip for DNA-Directed Immobilization of Oligonucleotide-Tagged Compounds. *Small* **2009**, *5* (13), 1547–1552. https://doi.org/10.1002/smll.200801016.
(156) Kampe, T.; König, A.; Schroeder, H.; Hengstler, J. G.; Niemeyer, C. M. Modular Microfluidic System for Emulation of Human Phase I/Phase II Metabolism. *Anal. Chem.* **2014**, *86* (6), 3068–3074. https://doi.org/10.1021/ac404128k.
(157) Logan, T. C.; Clark, D. S.; Stachowiak, T. B.; Svec, F.; Fréchet, J. M. J. Photopatterning Enzymes on Polymer Monoliths in Microfluidic Devices for Steady-State Kinetic Analysis and Spatially Separated Multi-Enzyme Reactions. *Anal. Chem.* **2007**, *79* (17), 6592–6598. https://doi.org/10.1021/ac070705k.
(158) Kornacki, J. R.; Stuparu, A. D.; Mrksich, M. Acetyltransferase P300/CBP Associated Factor (PCAF) Regulates Crosstalk-Dependent Acetylation of Histone H3 by Distal Site Recognition. *ACS Chem. Biol.* **2015**, *10* (1), 157–164. https://doi.org/10.1021/cb5004527.
(159) Mrksich, M.; Sigal, G. B.; Whitesides, G. M. Surface Plasmon Resonance Permits in Situ Measurement of Protein Adsorption on Self-Assembled Monolayers of Alkanethiolates on Gold. *Langmuir* **1995**, *11* (11), 4383–4385. https://doi.org/10.1021/la00011a034.
(160) Lee, J.; Ryoo, S.-R.; Kim, S. K.; Ahn, J.-H.; Min, D.-H.; Yeo, W.-S. Quantitation of Surface-Bound Proteins on Biochips Using MALDI-TOF MS. *Analytical Sciences* **2011**, *27* (11), 1127–1127. https://doi.org/10.2116/analsci.27.1127.
(161) Hodneland, C. D.; Lee, Y.-S.; Min, D.-H.; Mrksich, M. Selective Immobilization of Proteins to Self-Assembled Monolayers Presenting Active Site-Directed Capture Ligands. *PNAS* **2002**, *99* (8), 5048–5052. https://doi.org/10.1073/pnas.072685299.
(162) Eisenberg, J. L.; Piper, J. L.; Mrksich, M. Using Self-Assembled Monolayers to Model Cell Adhesion to the 9th and 10th Type III Domains of Fibronectin. *Langmuir* **2009**, *25* (24), 13942–13951. https://doi.org/10.1021/la901528c.

(163) Juillerat, A.; Gronemeyer, T.; Keppler, A.; Gendreizig, S.; Pick, H.; Vogel, H.; Johnsson, K. Directed Evolution of O6-Alkylguanine-DNA Alkyltransferase for Efficient Labeling of Fusion Proteins with Small Molecules in Vivo. *Chem. Biol.* **2003**, *10* (4), 313–317.
(164) Srikun, D.; Albers, A. E.; Nam, C. I.; Iavarone, A. T.; Chang, C. J. Organelle-Targetable Fluorescent Probes for Imaging Hydrogen Peroxide in Living Cells via SNAP-Tag Protein Labeling. *J. Am. Chem. Soc.* **2010**, *132* (12), 4455–4465. https://doi.org/10.1021/ja100117u.
(165) Lukinavičius, G.; Reymond, L.; Johnsson, K. Fluorescent Labeling of SNAP-Tagged Proteins in Cells. In *Site-Specific Protein Labeling*; Methods in Molecular Biology; Humana Press, New York, NY, 2015; pp 107–118. https://doi.org/10.1007/978-1-4939-2272-7_7.
(166) Los, G. V.; Encell, L. P.; McDougall, M. G.; Hartzell, D. D.; Karassina, N.; Zimprich, C.; Wood, M. G.; Learish, R.; Ohana, R. F.; Urh, M.; et al. HaloTag: A Novel Protein Labeling Technology for Cell Imaging and Protein Analysis. *ACS Chem. Biol.* **2008**, *3* (6), 373–382. https://doi.org/10.1021/cb800025k.
(167) Chan, H. N.; Chen, Y.; Shu, Y.; Chen, Y.; Tian, Q.; Wu, H. Direct, One-Step Molding of 3D-Printed Structures for Convenient Fabrication of Truly 3D PDMS Microfluidic Chips. *Microfluid Nanofluid* **2015**, *19* (1), 9–18. https://doi.org/10.1007/s10404-014-1542-4.
(168) Comina, G.; Suska, A.; Filippini, D. PDMS Lab-on-a-Chip Fabrication Using 3D Printed Templates. *Lab Chip* **2013**, *14* (2), 424–430. https://doi.org/10.1039/C3LC50956G.
(169) Seong, G. H.; Heo, J.; Crooks, R. M. Measurement of Enzyme Kinetics Using a Continuous-Flow Microfluidic System. *Anal. Chem.* **2003**, *75* (13), 3161–3167. https://doi.org/10.1021/ac034155b.
(170) Gong, A.; Zhu, C.-T.; Xu, Y.; Wang, F.-Q.; Tsabing, D. K.; Wu, F.-A.; Wang, J. Moving and Unsinkable Graphene Sheets Immobilized Enzyme for Microfluidic Biocatalysis. *Scientific Reports* **2017**, *7* (1), 4309. https://doi.org/10.1038/s41598-017-04216-4.
(171) Bicker, K. L.; Subramanian, V.; Chumanevich, A. A.; Hofseth, L. J.; Thompson, P. R. Seeing Citrulline: Development of a Phenylglyoxal-Based Probe To Visualize Protein Citrullination. *J. Am. Chem. Soc.* **2012**, *134* (41), 17015–17018. https://doi.org/10.1021/ja308871v.
(172) Elani, Y.; Law, R. V.; Ces, O. Vesicle-Based Artificial Cells as Chemical Microreactors with Spatially Segregated Reaction Pathways. *Nature Communications* **2014**, *5*, 5305. https://doi.org/10.1038/ncomms6305.
(173) Hosoya, O.; Chono, S.; Saso, Y.; Juni, K.; Morimoto, K.; Seki, T. Determination of Diffusion Coefficients of Peptides and Prediction of Permeability through a Porous Membrane. *Journal of Pharmacy and Pharmacology* **2004**, *56* (12), 1501–1507. https://doi.org/10.1211/0022357044878.
(174) Kirby, B. J. Passive Scalar Transport: Dispersion, Patterning, and Mixing. In *Micro and Nanoscale Fluid Mechanics: Transport in Microfluidic Devices*; Cambridge University Press: Cambridge, 2010; pp 79-96,
(175) Squires, T. M.; Messinger, R. J.; Manalis, S. R. Making It Stick: Convection, Reaction and Diffusion in Surface-Based Biosensors. *Nature Biotechnology* **2008**, *26* (4), 417–426. https://doi.org/10.1038/nbt1388.

(176) Fu, J.; Liu, M.; Liu, Y.; Woodbury, N. W.; Yan, H. Interenzyme Substrate Diffusion for an Enzyme Cascade Organized on Spatially Addressable DNA Nanostructures. *J. Am. Chem. Soc.* **2012**, *134* (12), 5516–5519. https://doi.org/10.1021/ja300897h.
(177) Fu, Y.; Zeng, D.; Chao, J.; Jin, Y.; Zhang, Z.; Liu, H.; Li, D.; Ma, H.; Huang, Q.; Gothelf, K. V.; et al. Single-Step Rapid Assembly of DNA Origami Nanostructures for Addressable Nanoscale Bioreactors. *J. Am. Chem. Soc.* **2013**, *135* (2), 696–702. https://doi.org/10.1021/ja3076692.
(178) Mathesh, M.; Liu, J.; Barrow, C. J.; Yang, W. Graphene-Oxide-Based Enzyme Nanoarchitectonics for Substrate Channeling. *Chemistry – A European Journal* **2017**, *23* (2), 304–311. https://doi.org/10.1002/chem.201604348.
(179) Min, D.-H.; Yeo, W.-S.; Mrksich, M. A Method for Connecting Solution-Phase Enzyme Activity Assays with Immobilized Format Analysis by Mass Spectrometry. *Anal. Chem.* **2004**, *76* (14), 3923–3929. https://doi.org/10.1021/ac049816z.
(180) Wilner, O. I.; Weizmann, Y.; Gill, R.; Lioubashevski, O.; Freeman, R.; Willner, I. Enzyme Cascades Activated on Topologically Programmed DNA Scaffolds. *Nat Nanotechnol* **2009**, *4* (4), 249–254. https://doi.org/10.1038/nnano.2009.50.
(181) Vong, T.; Schoffelen, S.; Dongen, S. F. M. van; Beek, T. A. van; Zuilhof, H.; Hest, J. C. M. van. A DNA-Based Strategy for Dynamic Positional Enzyme Immobilization inside Fused Silica Microchannels. *Chem. Sci.* **2011**, *2* (7), 1278–1285. https://doi.org/10.1039/C1SC00146A.
(182) Nguyen, K. V.; Giroud, F.; Minteer, S. D. Improved Bioelectrocatalytic Oxidation of Sucrose in a Biofuel Cell with an Enzyme Cascade Assembled on a DNA Scaffold. *J. Electrochem. Soc.* **2014**, *161* (14), H930–H933. https://doi.org/10.1149/2.0761414jes.
(183) Schröder, H.; Hoffmann, L.; Müller, J.; Alhorn, P.; Fleger, M.; Neyer, A.; Niemeyer, C. M. Addressable Microfluidic Polymer Chip for DNA-Directed Immobilization of Oligonucleotide-Tagged Compounds. *Small 5* (13), 1547–1552. https://doi.org/10.1002/smll.200801016.
(184) Niemeyer, C. M.; Koehler, J.; Wuerdemann, C. DNA-Directed Assembly of Bienzymic Complexes from In Vivo Biotinylated NAD(P)H:FMN Oxidoreductase and Luciferase. *ChemBioChem* **2002**, *3* (2–3), 242–245. https://doi.org/10.1002/1439-7633(20020301)3:2/3<242::AID-CBIC242>3.0.CO;2-F.
(185) Niemeyer, C. M.; Sano, T.; Smith, C. L.; Cantor, C. R. Oligonucleotide-Directed Self-Assembly of Proteins: Semisynthetic DNA—Streptavidin Hybrid Molecules as Connectors for the Generation of Macroscopic Arrays and the Construction of Supramolecular Bioconjugates. *Nucleic Acids Res* **1994**, *22* (25), 5530–5539. https://doi.org/10.1093/nar/22.25.5530.
(186) Witalison, E. E.; Thompson, P. R.; Hofseth, L. J. Protein Arginine Deiminases and Associated Citrullination: Physiological Functions and Diseases Associated with Dysregulation. *Curr Drug Targets* **2015**, *16* (7), 700–710.
(187) Zhao, T.; Pan, B.; Alam, H. B.; Liu, B.; Bronson, R. T.; Deng, Q.; Wu, E.; Li, Y. Protective Effect of Cl-Amidine against CLP-Induced Lethal Septic Shock in Mice. *Scientific Reports* **2016**, *6*, 36696. https://doi.org/10.1038/srep36696.
(188) Chumanevich, A. A.; Causey, C. P.; Knuckley, B. A.; Jones, J. E.; Poudyal, D.; Chumanevich, A. P.; Davis, T.; Matesic, L. E.; Thompson, P. R.; Hofseth, L. J. Suppression

of Colitis in Mice by Cl-Amidine: A Novel Peptidylarginine Deiminase Inhibitor. *Am. J. Physiol. Gastrointest. Liver Physiol.* **2011**, *300* (6), G929-938. https://doi.org/10.1152/ajpgi.00435.2010.

(189) Knuckley, B.; Causey, C. P.; Jones, J. E.; Bhatia, M.; Dreyton, C. J.; Osborne, T. C.; Takahara, H.; Thompson, P. R. Substrate Specificity and Kinetic Studies of PADs 1, 3, and 4 Identify Potent and Selective Inhibitors of Protein Arginine Deiminase 3. *Biochemistry* **2010**, *49* (23), 4852–4863. https://doi.org/10.1021/bi100363t.

(190)Bennike, T.; Lauridsen, K. B.; Olesen, M. K.; Andersen, V.; Birkelund, S.; Stensballe, A. Optimizing the Identification of Citrullinated Peptides by Mass Spectrometry: Utilizing the Inability of Trypsin to Cleave after Citrullinated Amino Acids. *Journal of Proteomics & Bioinformatics* **2013**, *6* (12). https://doi.org/10.4172/jpb.1000293.

(191) Tutturen, A. E. V.; Holm, A.; Jørgensen, M.; Stadtmüller, P.; Rise, F.; Fleckenstein, B. A Technique for the Specific Enrichment of Citrulline-Containing Peptides. *Anal. Biochem.* **2010**, *403* (1–2), 43–51. https://doi.org/10.1016/j.ab.2010.04.012.

(192) Chokkalingam, V.; Tel, J.; Wimmers, F.; Liu, X.; Semenov, S.; Thiele, J.; Figdor, C. G.; Huck, W. T. S. Probing Cellular Heterogeneity in Cytokine-Secreting Immune Cells Using Droplet-Based Microfluidics. *Lab Chip* **2013**, *13* (24), 4740–4744. https://doi.org/10.1039/c3lc50945a.

(193) Zhou, J.; Zeng, J.; Grant, J.; Wu, H.; Xia, Y. On-Chip Screening of Experimental Conditions for the Synthesis of Noble-Metal Nanostructures with Different Morphologies. *Small* **2011**, *7* (23), 3308–3316. https://doi.org/10.1002/smll.201101299.

(194) Gossweiler, G. R.; Brown, C. L.; Hewage, G. B.; Sapiro-Gheiler, E.; Trautman, W. J.; Welshofer, G. W.; Craig, S. L. Mechanochemically Active Soft Robots. *ACS Appl. Mater. Interfaces* **2015**, *7* (40), 22431–22435. https://doi.org/10.1021/acsami.5b06440.

(195) Rountree, A.; Karkamkar, A.; Khalil, G.; Folch, A.; Cook, D. L.; Sweet, I. R. BaroFuse, a Novel Pressure-Driven, Adjustable-Throughput Perfusion System for Tissue Maintenance and Assessment. *Heliyon* **2016**, *2* (12), e00210. https://doi.org/10.1016/j.heliyon.2016.e00210.

(196) Urrios, A.; Parra-Cabrera, C.; Bhattacharjee, N.; Gonzalez-Suarez, A. M.; Rigat-Brugarolas, L. G.; Nallapatti, U.; Samitier, J.; Deforest, C. A.; Posas, F.; Garcia-Cordero, J. L.; et al. 3D-Printing of Transparent Bio-Microfluidic Devices in PEG-DA. *Lab Chip* **2016**, *16* (12), 2287–2294. https://doi.org/10.1039/c6lc00153j.

(197) Gautier, A.; Juillerat, A.; Heinis, C.; Corrêa, I. R.; Kindermann, M.; Beaufils, F.; Johnsson, K. An Engineered Protein Tag for Multiprotein Labeling in Living Cells. *Chemistry & Biology* **2008**, *15* (2), 128–136. https://doi.org/10.1016/j.chembiol.2008.01.007.

(198) Griffin, B. A.; Adams, S. R.; Tsien, R. Y. Specific Covalent Labeling of Recombinant Protein Molecules inside Live Cells. *Science* **1998**, *281* (5374), 269–272.

(199) Kilian, K. A.; Mrksich, M. Directing Stem Cell Fate by Controlling the Affinity and Density of Ligand-Receptor Interactions at the Biomaterials Interface. *Angew Chem Int Ed Engl* **2012**, *51* (20), 4891–4895. https://doi.org/10.1002/anie.201108746.

(200) Glick, C. C.; Srimongkol, M. T.; Schwartz, A. J.; Zhuang, W. S.; Lin, J. C.; Warren, R. H.; Tekell, D. R.; Satamalee, P. A.; Lin, L. Rapid Assembly of Multilayer Microfluidic Structures via 3D-Printed Transfer Molding and Bonding. *Microsystems & Nanoengineering* **2016**, *2*, 16063. https://doi.org/10.1038/micronano.2016.63.

(201) Bhattacharjee, N.; Parra-Cabrera, C.; Kim, Y. T.; Kuo, A. P.; Folch, A. Desktop-Stereolithography 3D-Printing of a Poly(Dimethylsiloxane)-Based Material with Sylgard-184 Properties. *Advanced Materials* **2018**, *30* (22), 1800001. https://doi.org/10.1002/adma.201800001.
(202) Mrksich, M.; Chen, C. S.; Xia, Y.; Dike, L. E.; Ingber, D. E.; Whitesides, G. M. Controlling Cell Attachment on Contoured Surfaces with Self-Assembled Monolayers of Alkanethiolates on Gold. *PNAS* **1996**, *93* (20), 10775–10778. https://doi.org/10.1073/pnas.93.20.10775.
(203) Sánchez-Cortés, J.; Mrksich, M. Using Self-Assembled Monolayers to Understand A8β1-Mediated Cell Adhesion to RGD and FEI Motifs in Nephronectin. *ACS Chem. Biol.* **2011**, *6* (10), 1078–1086. https://doi.org/10.1021/cb200186j.

Appendices

Appendix A. iSAMDI-MS demonstration on the rapifleX MALDI Tissuetyper

This work was performed in collaboration with Sohrab Habibi Goudarzi and Sergei Dikler.

The next generation of iSAMDI-MS experimentation will be performed on the rapifleX MALDI Tissuetyper (Bruker Daltonics) due to its fast acquisition rate (10 kHz) and low pixel resolution (10 µM). This work surveyed iSAMDI-MS performance on the rapifleX in reflector positive mode with a peptide m/z= 2110. The main criteria assessed were: signal sensitivity, peak resolution, pixel resolution, and laser firing rate. I prepared a gold-coated microscope slide functionalized with a self-assembled monolayer presenting maleimide groups at a density of 10% against a background of tri(ethylene glycol) groups. A PDMS block containing serpentine channel features was placed onto the slide and a solution of peptide (100 µM in 10 mM Tris 8.0) with the sequence Ac-TARK^{Ac}STGGKAPC was flowed through the PDMS block at 0.5 µL min^{-1} for 3 h. Tris 8.0 buffer (10 mM) was flowed through the device to rinse out excess peptide solution, the PDMS block was removed from the chip, and the chip was washed sequentially with ethanol and water. The chip was placed in a vacuum sealed bag and shipped overnight to Bruker Daltonics in Massachusetts, USA. Figure A.1 shows a SAMDI mass spectra and

iSAMDI-MS dataset acquired on the rapifleX.

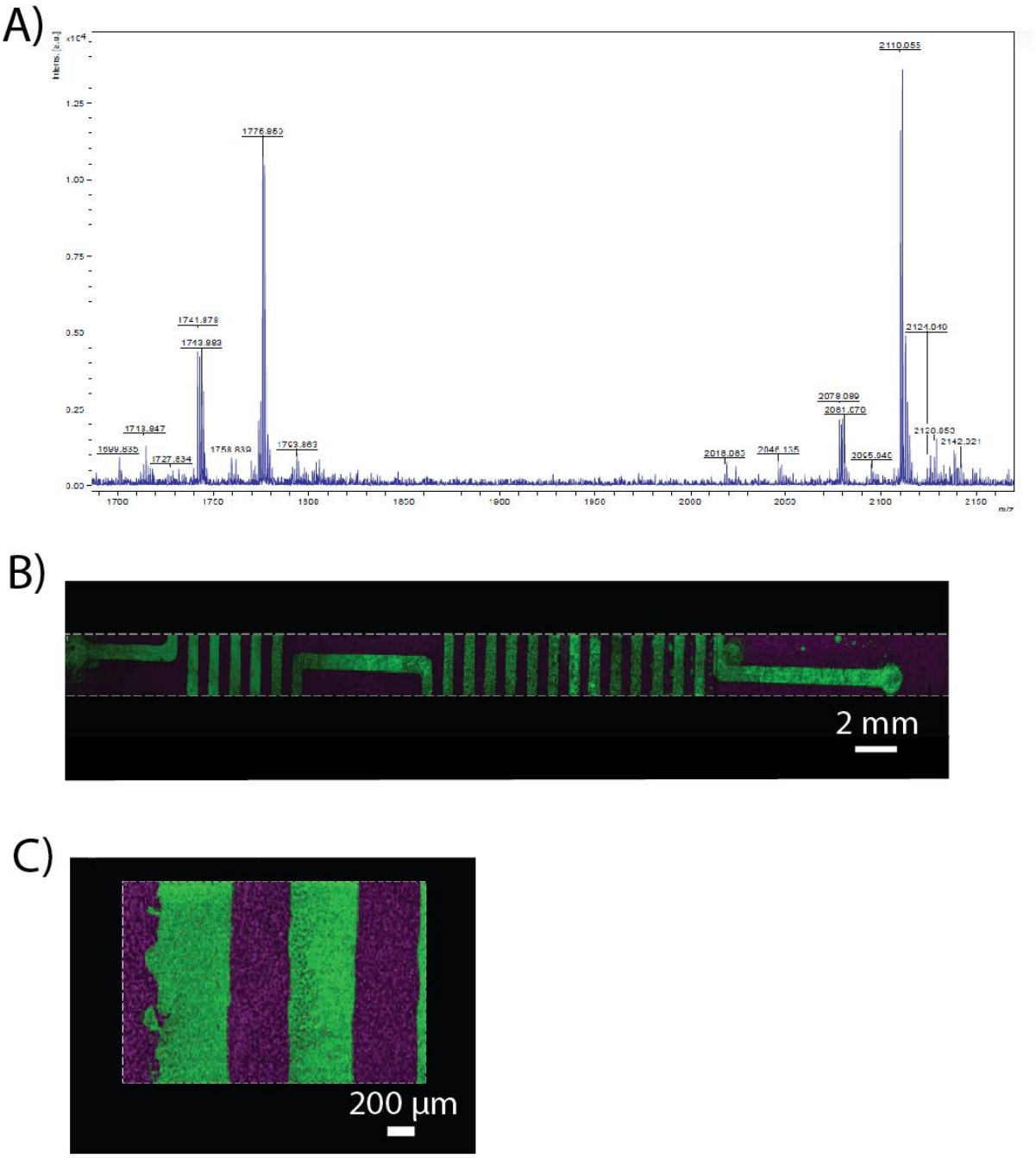

Figure A.1 RapifleX MALDI-TOF/TOF imaging demonstration. A) iSAMDI-MS spectrum acquired from the channel; B) channel section acquired at 10 µm resolution with 28,137 spectra, *m/z* 851.5 (purple), *m/z* 2110.1 (green); C) horizontal channel cross section acquired at 30 µm resolution with 95,200 spectra, *m/z* 851.5 (purple), *m/z* 2110.1 (green).

Appendix B. A 3D printed cell culture chamber for improved confocal microscope imaging

This work was performed in collaboration with Pradeep Bugga.

Gold-functionalized SAMs have been used to study cell-surface interactions including cell attachment, migration, and differentiation.[202,203] In a typical experiment, a gold-coated coverslip functionalized with adhesion ligand presenting SAMs is placed into a petri dish, the dish is filled with cell media, and cells are seeded onto the SAM. Microscopes with inverted stages (i.e. the objectives are below the stage) obtain images through the back side of the sample, which is problematic for obtaining high-quality microscopy images because the petri dish obscures the image quality. The goal of this work was to design an apparatus for seeding cells on SAMs at 37 °C for ≤12 h without requiring a petri dish.

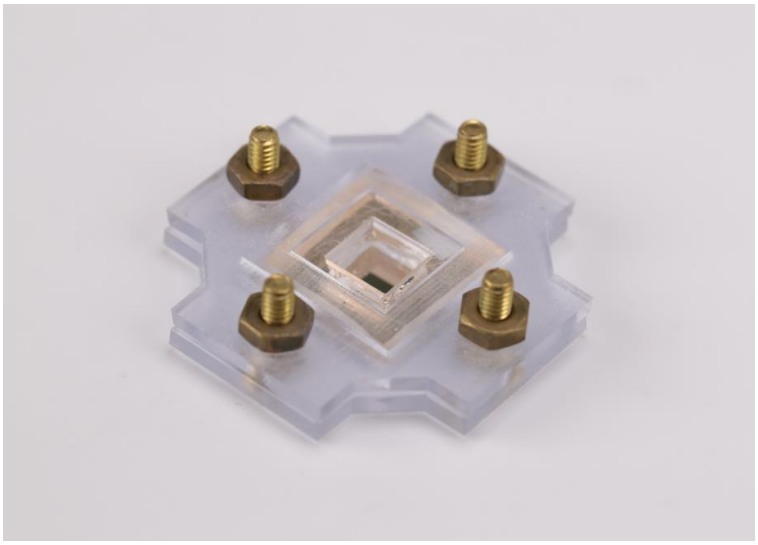

Figure B.1 Device for culturing cells on SAMs and acquiring high quality microscopy photos with an inverted stage microscope.

The design consisted of a rectangular PDMS block contacting the SAM-coated coverslip that was held together between a 3D printed clamp with 4 screws (Figure B.1). The PDMS block was cast from a 3D printed master. The PDMS block was treated with O_2 plasma and bonded to the coverslip to prevent the media from leaking. SolidWorks renderings of the 3D printed parts, the device assembly, and a photo of a HUVEC cell on the SAM from the device are shown in Figure B.2.

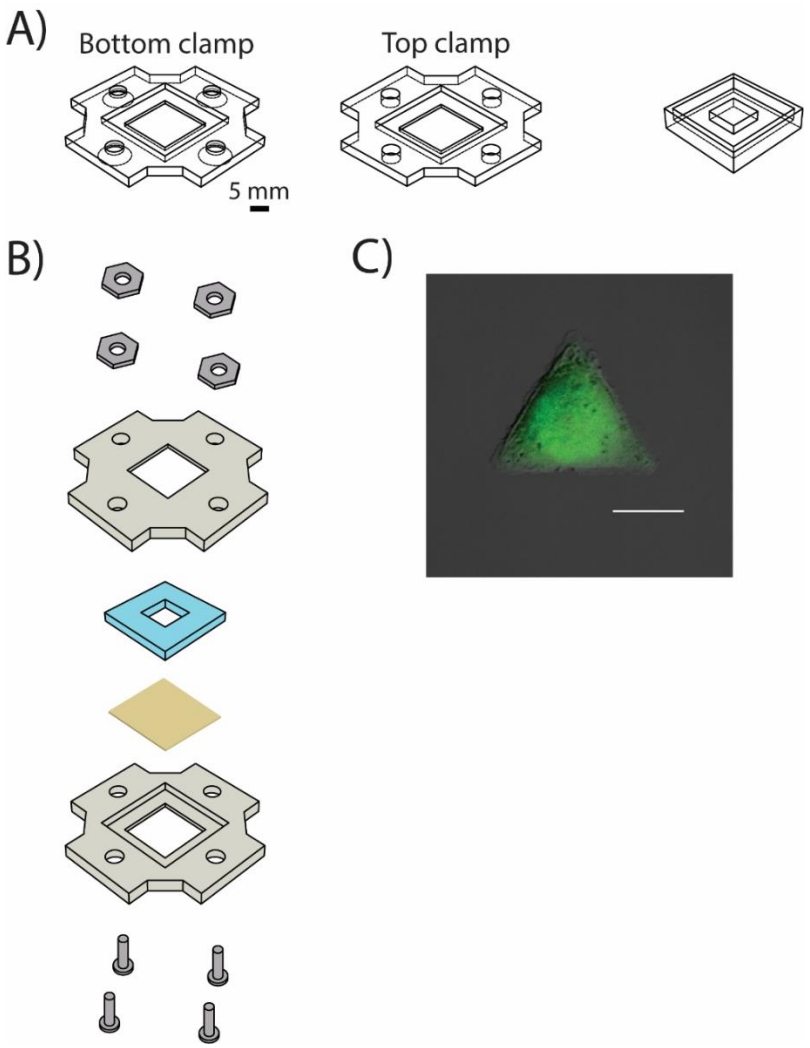

Figure B.2 Clamp design and assembly. A) SolidWorks renderings of 3D printed clamp (left, middle) and PDMS master (right), B) Clamp assembly C) HUVEC cell patterned on the SAM in a triangle shape in the cell culture device (scale bar= 20 µm).

Methods:

3D printing of Clamp and PDMS master. The top clamp piece, bottom clamp piece, and PDMS master were designed in SolidWorks. The top and bottom clamp pieces have a 10 mm x 10 mm x 1 mm opening in the center and a 25 mm x 25 mm x 2 mm inset to contain the Au slide and PDMS. The PDMS master has a 25 mm x 25 mm x 3 mm outer inset and a 10 mm x 10 mm x 3 mm inner inset. The renderings were converted to .stl format and printed on a Stratasys Connex 350 3D printer in digital printing mode. The top and bottom clamp pieces were printed in VeroClear or VeroWhite material (Stratasys) with a glossy finish, and the PDMS master was printed in White material with a glossy finish. The support material was printed on the flat side of the PDMS master away from the area designated for PDMS polymerization. For all parts, the support material was removed with a WaterJet, rinsed with ultrapure water, and dried under a nitrogen stream.

Preparing the PDMS piece. After 3D printing and washing, the PDMS master was placed in a 42 °C oven for 24 h. PDMS prepolymer mixture was mixed in a 1:9 ratio (w/w curing agent to prepolymer), degassed in a vacuum desiccator for 15 min, then poured into the PDMS master. The PDMS master was degassed for 15 min in a vacuum desiccator for 15 min and placed in a 42 °C oven for 14 h.

Plasma Cleaning. The PDMS block was treated with 50 W air plasma for 35 s at 200 mTorr using a Solarus Plasma Cleaner.

Core Facilities. This work used the Northwestern University 3D Printing & Rapid Prototyping Lab and the Northwestern University Structural Biology Core.